UNIVERSITY OF OKLAHOMA

GRADUATE COLLEGE

SUPERSYMMETRY

AND THE PRISONER OF NATURALNESS

A DISSERTATION

SUBMITTED TO THE GRADUATE FACULTY

in partial fulfillment of the requirements for the

Degree of

DOCTOR OF PHILOSOPHY

By

MICHAEL ROBERT SAVOY
Norman, Oklahoma
2017

SUPERSYMMETRY
AND THE PRISONER OF NATURALNESS

A DISSERTATION APPROVED FOR THE
HOMER L. DODGE DEPARTMENT OF PHYSICS AND ASTRONOMY

BY

_____
Dr. Howard Baer, Chair

_____
Dr. Chung Kao

_____
Dr. Michael Strauss

_____
Dr. Bruno Uchoa

_____
Dr. Robert White

To Howie Baer for his limitless patience.

To my loving parents, Carol and Ron,

who always encouraged me to pursue my passion.

To Kaity for her unending love and support along the way.

Table of Contents

List of Tables

List of Figures

Abstract

In this work, I will address three concerns of supersymmetry. The first is the notion of naturalness and how much fine-tuning exists in a model. Historical measures, Δ_{HS} and Δ_{BG}, have led to an over estimate of the amount of fine-tuning and consequently to false claims about limits on supersymmetric particle masses. These supersymmetric particles masses have since been excluded, provoking claims that supersymmetry is fine-tuned and in a crisis. These claims are supported by incorrect measures of fine-tuning. In chapter 2, fine-tuning measures will be re-examined, leading to Δ_{EW}, a conservative estimate that is straight forward to calculate and free of inherent cancellations and ambiguity. A limit on the amount of fine-tuning allowed for natural models is set, which will be used to constrain the parameter space.

The second concern in supersymmetry is determining how large the parameter space is. In choosing different archetypes of models, the parameter space is determined by a small set of input variables. In chapter 3, the archetypes scanned will include grand unification theories with gauge symmetries of either $SO(10)$ or $SU(5)$ as well as a general supergravity model. Furthermore, a non-unified model that has both anomaly and gravity mediation will be searched. Taking the upper limit allowed for natural supersymmetry models will constrain not only the inputs of the model, but also the outputs, such as particle masses, to lie within a finite amount of parameter space in which supersymmetry can live.

The third concern of supersymmetry is whether or not experiments will be able to find any new particles and verify supersymmetry. The large hadron collider is currently running, colliding protons with a center of mass energy of 14 TeV to

generate new particles. Whether or not it will be able to find supersymmetric particles depends on how massive the new particles are, the frequency of their interactions, and how well the events generating new particles can be distinguished from the events containing known particles. A number of production channels will be searched: gluino pairs, same-sign di-bosons, higgsino pairs, and top squark pairs. These processes will determine the limit of how far in the parameter space the large hadron collider can search. It will be shown that for the unified models, the large hadron collider may exclude the entire parameter space if no super-symmetry signals are found. For the mixed anomaly and gravity mediation, an upgrade from 14 TeV to 33 TeV would be required to exclude the entire parameter space. Alternatively, instead of colliding protons, if the international linear collider is constructed, colliding electrons and positrons with enough energy to create Higgs bosons and higgsinos, the linear collider with center of mass energy of 600 GeV would be able to search the entire parameter space of any natural model.

Chapter 1

Introduction

In this work, many acronyms and abbreviations are used. A complete list is displayed in the appendix.

BG	:	BackGround
CP	:	Charge and Parity conjugation
EW	:	Electro-Weak
EWSB	:	Electro-Weak Symmetry Breaking
GMM	:	Generalized Gauge Mediation
GUT	:	Grand Unified Theory
HE-LHC	:	High Energy LHC
HL-LHC	:	High Luminosity LHC
ILC	:	International Linear Collider
LEP	:	Large Electron-Position collider
LHC	:	Large Hadron Collider
LO	:	Leading-Order
LSP	:	Lightest Supersymmetric Particle
MM	:	Mirage Mediation
MSSM	:	Minimal Supersymmetric Standard Model
nGMM	:	natural Generalized Mirage Mediation
NLO	:	Next-to-Leading Order
NUHM2	:	Non-Universal Higgs Model with 2 extra parameters
NUHM2+D	:	NUHM2 with D-term symmetry breaking
OS	:	Opposite-Sign
QCD	:	Quantum ChromoDynamics
REWSB	:	Radiative Electro Weak Symmetry Breaking
RGE	:	Renormalization Group Equation
RNS	:	Radiatively-driven Natural Supersymmetry
SF	:	Same-Flavor
SM	:	Standard Model
SS	:	Same-Sign
SSB	:	Soft Supersymmetry Breaking
SSdB	:	Same-Sign di-Boson
SUGRA	:	SUper GRAvity
SUSY	:	SUperSYmmetry
VEV	:	Vacuum Expectation Value

Table 1.1: List of acronyms and abbreviations used, sorted alphabetically.

1.1 Standard Model

The Standard Model (SM) of particle physics is a relativistic, quantum mechanical, renormalizable theory of particles and their interactions. The information about the particles, which are excitations of quantum fields, and details of their interactions are contained in the Lagrangian[1]. The Lagrangian is used to determine the Feynman diagrams from which theoretical calculations can be done perturbatively, order by order, up to the desired precision. The group structure of the SM is $SU(3)_C \otimes SU(2)_L \otimes U(1)_Y$, where C denotes color, L denotes left-handed, and Y denotes hypercharge. $SU(2)_L \otimes U(1)_Y$ is spontaneously broken to $U(1)_{em}$. The fields are organized in multiplets; left-handed leptons and quarks, L and Q, as well as their individual right-handed counterparts, and Higgs, Φ, listed in table 1.2.

1.1.1 Standard Model Lagrangian

The Lagrangian for the SM can be broken down into two parts: the electroweak (EW), $\mathcal{L}_{EW}$, and the quantum chromodynamics (QCD), $\mathcal{L}_{QCD}$. The EW Lagrangian can be broken into four parts: gauge, matter, Higgs, and Yukawa as

$$\mathcal{L}_{EW} = \mathcal{L}_{gauge} + \mathcal{L}_{matter} + \mathcal{L}_{Higgs} + \mathcal{L}_{Yukawa} \ . \tag{1.1}$$

The gauge Lagrangian can be written in terms of $SU(2)_L$ and $U(1)_Y$ gauge fields, $W_{A\mu}$ and B_μ, as

$$\mathcal{L}_{gauge} = -\frac{1}{4}W_{A\mu\nu}W_A^{\mu\nu} - \frac{1}{4}B_{\mu\nu}B^{\mu\nu} \ , \tag{1.2}$$

Field	$SU(3)_C$	$SU(2)_L$	$U(1)_Y$
$L_3,\ L_2,\ L_1 = \begin{bmatrix} \nu_L \\ e_L \end{bmatrix}$	**1**	**2**	-1
$\tau_R,\ \mu_R,\ e_R$	**1**	**1**	2
$Q_3,\ Q_2,\ Q_1 = \begin{bmatrix} u_L \\ d_L \end{bmatrix}$	**3**	**2**	1/3
$t_R,\ c_R,\ u_R$	**3***	**1**	-4/3
$b_R,\ s_R,\ d_R$	**3***	**1**	2/3
$\Phi = \begin{bmatrix} \phi^+ \\ \phi^0 \end{bmatrix}$	**1**	**2**	1
$g_{1,\dots,8}$	**8**	**1**	0
$W_{1,2,3}$	**1**	**3**	0
B	**1**	**1**	0

Table 1.2: The matter, Higgs, and gauge field content of the SM, with associated gauge quantum numbers.

where $B_{\mu\nu} = \partial_\mu B_\nu - \partial_\nu B_\mu$ and $W_{A\mu\nu} = \partial_\mu W_{A\nu} - \partial_\nu W_{A\mu}$. After breaking $SU(2)_L$ symmetry through the Higgs mechanism, W_1 and W_2 mix to give the $W^\pm$ bosons while W_3 and B mix to give the Z boson responsible for mediating the weak nuclear force. Furthermore, the W_3 and B mix providing the photon, γ, responsible for mediating the electromagnetic force. The matter Lagrangian depends upon the flavors of matter fields, $\psi_j \in \{L_i, Q_i, u_{Ri}, d_{Ri}, e_{Ri}\}$, where L and Q are the left handed leptons and quarks; u_{Ri}, d_{Ri}, and e_{Ri} are the right handed up, down, and lepton fields; and $i \in \{1, 2, 3\}$ for the three generations. The matter Lagrangian is expressed as

$$\mathcal{L}_{matter} = \sum_{\text{flav, i}} i\bar{\psi}_i \slashed{D} \psi_i \ , \tag{1.3}$$

where D is the covariant derivative

$$D_\mu = \partial_\mu + igW_\mu \cdot T + \frac{1}{2}ig'B_\mu Y \ , \tag{1.4}$$

where g and g' are the $SU(2)_L$ and $U(1)_Y$ coupling constants, $W_{\mu A}$ is an $SU(2)_L$ gauge isotriplet with weak isospin operator T, and B_μ is a $U(1)_Y$ gauge singlet with weak hypercharge operator Y. The Higgs doublet, Φ, is introduced in the Lagrangian in terms of the kinetic and potential components in terms of the Higgs mass parameter, μ_{SM}, and quadratic constant, λ, as

$$\mathcal{L}_{Higgs} = (D\Phi)^\dagger (D\Phi) - V(\Phi) \ , \text{where} \tag{1.5a}$$

$$V(\Phi) = -\mu_{SM}^2 \Phi^\dagger \Phi + \lambda \left(\Phi^\dagger \Phi\right)^2 \ , \tag{1.5b}$$

with $\mu_{SM}^2 > 0$. Lastly, the Yukawa interaction Lagrangian is the trilinear combination of the Higgs field with the matter fields, using the completely anti-symmetric $SU(2)$ tensor, ϵ^{ab}, with $\epsilon^{12} = 1$, as

$$\mathcal{L}_{Yukawa} = -\sum_{\text{gens}} \left(\lambda_e \, \bar{L} \cdot \Phi \, e_R + \lambda_d \overline{Q} \cdot \Phi \, d_R + \lambda_u \, \epsilon^{ab} \overline{Q}_a \Phi_b^\dagger u_R + \text{h.c.} \right) \ . \tag{1.6}$$

The QCD Lagrangian has the interactions of the strong nuclear force, mediated by the eight gluon $SU(3)_C$ gauge fields, $G_{A\mu\nu}$. The particles that interact with gluons are the six quarks, q (up, u, down, d, charm, c, strange, s, top, t, and bottom, b) carrying color (red, green, or blue), antiquarks, $\bar{q}$, and gluons, carrying color-anti-color pairs. The QCD Lagrangian is written as

$$\mathcal{L}_{QCD} = -\frac{1}{4} G_{A\mu\nu} G_A^{\mu\nu} + \bar{q}_i \left(i\slashed{D} - m_i \right) q_i \ , \tag{1.7}$$

with the sum over quark flavors, q_i, the color index $i \in \{1, 2, 3\}$ for colors {red, green, blue}, and a covariant derivative of

$$D_\mu = \partial_\mu + i g_S \frac{\lambda_A}{2} G_{A\mu} \ . \tag{1.8}$$

The $SU(3)$ gauge fields satisfy

$$G_{\mathrm{A}\mu\nu} = \partial_\mu G_{\mathrm{A}\nu} - \partial_\nu G_{\mathrm{A}\mu} - g_S f_{\mathrm{ABC}} G_{\mathrm{B}\mu} G_{\mathrm{C}\nu} \;, \qquad (1.9)$$

where g_S is the strong coupling constant and λ_A are the eight Gell-Mann matrices. The color-anti-color adjoint index pairs $\mathrm{A}, \mathrm{B}, \mathrm{C} \in \{1, ..., 8\}$.

1.1.2 Higgs mechanism

The breaking of $SU(2)_L \otimes U(1)_Y$ to $U(1)_{em}$ is done through the Higgs mechanism. The Lagrangian is given by eq. (1.5)

$$\mathcal{L}_{Higgs} = (D\Phi)^\dagger (D\Phi) - V(\Phi) \;, \qquad (1.10a)$$

$$V(\Phi) = \mu_{\mathrm{SM}}^2 \Phi^\dagger \Phi + \lambda \left(\Phi^\dagger \Phi\right)^2 \;, \qquad (1.10b)$$

where Φ is a complex, scalar doublet

$$\Phi = \begin{bmatrix} \phi^+ \\ \phi^0 \end{bmatrix} = \begin{bmatrix} \phi_R^+ + i\phi_I^+ \\ \phi_R^0 + i\phi_I^0 \end{bmatrix} \;. \qquad (1.11)$$

For $\mu_{\mathrm{SM}}^2 < 0$, the real part of the Higgs field obtains a non-zero vacuum expectation value (VEV), denoted by v, expressed as

$$\langle \Phi \rangle = \frac{1}{\sqrt{2}} \begin{bmatrix} 0 \\ v \end{bmatrix} \qquad (1.12a)$$

$$v \equiv \langle \phi_R^0 \rangle = \sqrt{\frac{-\mu_{\mathrm{SM}}^2}{2\lambda}} \;. \qquad (1.12b)$$

Between the two complex components of the Higgs doublet, there are four degrees of freedom. Along with the VEV, three massless Goldstone bosons are introduced. The Goldstone bosons are absorbed by the $W_{1,2,3}$ fields, which mix to give rise

to massive $W^{\pm}$ (80.385 GeV) and Z (91.1876 GeV) bosons. The last degree of freedom is the Higgs boson with mass $m_h = \sqrt{-2\mu_{SM}}$, recently measured to be 125.09 ± 0.21 (stat.) ± 0.11 (syst.) GeV[2].

Furthermore, the Higgs boson interacts with the fermions' left and right handed fields, f_L and f_R, through the interaction Lagrangian, expressed as

$$\mathcal{L}_{int} = g_f \left(\bar{f}_L \Phi f_R + \text{h.c.} \right) \tag{1.13a}$$

$$= \frac{g_f v}{\sqrt{2}} \left(\bar{f}_L f_R + \bar{f}_R f_L \right) + \frac{g_f}{\sqrt{2}} \left(\bar{f}_L f_R + \bar{f}_R f_L \right) h \tag{1.13b}$$

Through this interaction, the masses of each fermion, $m_f = g_f v$, are introduced explicitly into the Lagrangian from the VEV of the Higgs potential.

1.1.3   Standard Model successes and limitations

The SM has been extremely successful as both a descriptive and predictive theory. High-precision tests have validated the accuracy of the SM. One such test is the measurement of the magnetic moment g-factor of the electron. Theoretical calculations have been computed up to tenth order[3], predicting $g/2 = 1.00115965218178(77)$. Experiments measured[4] $g/2 = 1.00115965218073(28)$, agreeing up to 10^{-12}. Evidence for the SM being a successful, predictive theory can be seen in the searches for the third generation quarks, b (predicted[5]: 1973, discovered[6]: 1977 through the Υ meson, $b\bar{b}$) and t (predicted[5]: 1973, discovered[7, 8]: 1995); W and Z bosons (predicted[9]: 1967, discovered[10, 11]: 1983); and the Higgs boson (predicted[12]: 1967, discovered[13, 14]: 2012).

Although the SM is very successful, there are limitations, including:

- gravity,

- dark matter,

- hierarchy problem,

- strong CP problem,

- neutrino masses, and

- baryogenesis.

The SM does not contain gravity, one of the fundamental forces of nature, a particle that is a valid cold dark matter candidate, right handed neutrinos to allow for neutrino masses, or a sufficient mechanism for baryogenesis to account for the matter-antimatter asymmetry. Furthermore, there is a large gap between the weak scale where the W, Z, and Higgs masses are and the grand unified theory (GUT) scale, where the Higgs mass would be expected due to quadratic contributions.

1.2 Supersymmetry

Supersymmetry (SUSY) is a quantum space-time symmetry relating particle statistics between fermions and bosons. Fermions (odd half-integer spin) obey Fermi-Dirac statistics while bosons (integer spin) obey Bose-Einstein statistics. For each fermion field, supersymmetry generates a boson field and vice versa. The supersymmetric bosons have the same name with an s in front, e.g. squark, stop, stau, etc. The supersymmetric fermions have the same name with ino at the end, e.g. gluino, wino, higgsino, etc. This statistical symmetry yields many convenient consequences, one of which is an inherent removal of quadratic divergences. Quadratic divergences arise in loop calculations to the Higgs mass in the

SM. Each fermion loop necessarily has the opposite sign contribution as the associate boson loop calculation. Because of this, quadratic divergences are exactly cancelled by their supersymmetric field counterpart to all orders in perturbation theory[15]. Furthermore, SUSY may provide a cold dark matter candidate particle if R-parity is conserved. R-parity is defined as

$$R = (-1)^{3(B-L)+2s} ,\qquad (1.14)$$

where B and L are baryon and lepton numbers respectively and s is the spin. If R-parity is conserved, then a sparticle may not decay to only SM particles, they may only be created or annihilated in pairs. Because of this, through a chain of decays, the lightest supersymmetric particle (LSP) is stable. If the LSP is electrically and chromatically neutral, then it makes a good cold dark matter candidate. These properties are just two of many that supersymmetry has to offer, including:

- freedom from quadratic divergences,

- ultra-violet completeness to the GUT scale,

- connection to gravity (described later in this section),

- connection to string theory through superstrings,

as well as experimental niceties, including:

- unification of gauge couplings at the GUT scale,

- cold dark matter due to R-parity conservation,

- electroweak symmetry radiatively broken (detailed in section 3.1),

8

- Higgs boson mass measurement falls squarely in the range 115 GeV $< m_h <$ 135 GeV as required by the Large Electron-Positron (LEP) collider and minimal supersymmetric standard model (MSSM) upper bound[16].

Relativistic quantum field theory is based upon the space-time symmetry of the Poincaré group, which includes the transformations of Lorentz boosts, rotations, and translations in space and time. To construct a chiral supersymmetric theory, supersymmetry generalizes the Poincaré group to include the super-Poincaré group. In constructing representations of the super-Poincaré group, spacetime is expanded to include *anti-commuting*, Grassmann valued coordinates, θ. A left chiral superfield is given by

$$\hat{\mathcal{S}}(x, \theta) = \mathcal{S}(\hat{x}) + i\sqrt{2}\,\bar{\theta}\,\psi(\hat{x}) + i\bar{\theta}\theta\mathcal{F}(\hat{x}) \ , \tag{1.15}$$

where $\hat{x}_\mu = x_\mu + \frac{i}{2}\bar{\theta}\gamma_5\gamma_\mu\theta$, $\mathcal{S}$ is a scalar, ψ is a spinor, and $\mathcal{F}$ is an auxiliary field. The supersymmetric interactions are included in a super-potential term, $\hat{f}$, which, along with the Kähler potential, K, and matter content, distinguishes one SUSY model from another. A supersymmetric Lagrangian can be written as the sum of the gauge, gauge kinetic (GK), F, and Fayet-Iliopoulos (FI), terms

$$\mathcal{L} = \mathcal{L}_{GK} + \mathcal{L}_{gauge} + \mathcal{L}_F + \mathcal{L}_{FI} \ . \tag{1.16}$$

The gauge kinetic term is given by

$$\mathcal{L}_{GK} = \frac{i}{2}\bar{\lambda}_{\rm A}\slashed{D}_{\rm AC}\lambda_{\rm C} - \frac{1}{4}F_{\mu\nu\rm A}F_{\rm A}^{\mu\nu} + \frac{1}{2}\mathcal{D}_{\rm A}\mathcal{D}_{\rm A} \ , \text{where} \tag{1.17a}$$

$$F_{\mu\nu\rm A} = \partial_\mu V_{\nu\rm A} - \partial_\nu V_{\mu\rm A} - gf_{\rm ABC}V_{\mu\rm B}V_{\nu\rm C} \ \text{ and} \tag{1.17b}$$

$$\left(\slashed{D}\lambda\right)_{\rm A} = \slashed{\partial}\lambda_{\rm A} + ig\left(t_{\rm B}\slashed{V}_{\rm B}\right)_{\rm AC}\lambda_{\rm C} \ . \tag{1.17c}$$

The gauge term is given by

$$\mathcal{L}_{gauge} = \frac{i}{2}\, \bar{\psi}\, \slashed{D}\, \psi + (D_\mu \mathcal{S})^\dagger\, (D^\mu \mathcal{S}) + \mathcal{F}^\dagger \mathcal{F}$$

$$- g\, \mathcal{S}^\dagger t \cdot \mathcal{D}\mathcal{S} + \left(-\sqrt{2}\, g\, \mathcal{S}^\dagger t_{\mathrm{A}} \bar{\lambda}_{\mathrm{A}} \frac{1 - \gamma_5}{2} \psi + \text{h.c.}\right) , \qquad (1.18)$$

where the covariant derivatives on $\mathcal{S}$ and ψ are

$$D_\mu \mathcal{S} = \partial_\mu \mathcal{S} + i\, g\, t \cdot V_\mu \mathcal{S} \qquad (1.19\text{a})$$

$$D_\mu \psi = \partial_\mu \psi + i\, g\, (t \cdot V_\mu)\, \psi_L - i\, g\, (t^* \cdot V_\mu)\, \psi_R . \qquad (1.19\text{b})$$

The F term is given by

$$\mathcal{L}_F = -i \sum_i \left.\frac{\partial \hat{f}}{\partial \hat{\mathcal{S}}_i}\right|_{\hat{\mathcal{S}}=\mathcal{S}} \mathcal{F}_i - \frac{1}{2} \sum_{i,j} \left.\frac{\partial^2 \hat{f}}{\partial \hat{\mathcal{S}}_i\, \partial \hat{\mathcal{S}}_j}\right|_{\hat{\mathcal{S}}=\mathcal{S}} \bar{\psi}_i\, P_L\, \psi_j + \text{h.c.} . \qquad (1.20)$$

The Fayet-Iliopoulos D-term is given by

$$\mathcal{L}_{\mathrm{FI}} = \xi_{\mathrm{p}} \mathcal{D}_{\mathrm{p}} , \qquad (1.21)$$

where ξ_{p} are coupling constants with $[\xi_{\mathrm{p}}] = 2$ and p runs over each $U(1)$ factor of the gauge group. Putting all this together in one expression, a complete

10

renormalizable, supersymmetric, Lagrangian for gauge theories is

$$
\begin{aligned}
\mathcal{L} = &\sum_{\mathrm{i}} \left(D_\mu \mathcal{S}_{\mathrm{i}}\right)^\dagger \left(D^\mu \mathcal{S}_{\mathrm{i}}\right) + \frac{i}{2} \sum_{\mathrm{i}} \bar{\psi}_{\mathrm{i}} \, \slashed{D} \, \psi_{\mathrm{i}} + \sum_{\mathrm{i}} \mathcal{F}_{\mathrm{i}}^\dagger \mathcal{F}_{\mathrm{i}} \\
&+ \frac{i}{2} \bar{\lambda}_{\mathrm{A}} \slashed{D}_{\mathrm{AC}} \lambda_{\mathrm{C}} - \frac{1}{4} F_{\mu\nu\mathrm{A}} F_{\mathrm{A}}^{\mu\nu} + \frac{1}{2} \mathcal{D}_{\mathrm{A}} \mathcal{D}_{\mathrm{A}} \\
&+ \left(-\sqrt{2} \, g \, \mathcal{S}^\dagger t_{\mathrm{A}} \bar{\lambda}_{\mathrm{A}} \frac{1 - \gamma_5}{2} \psi + \mathrm{h.c.} \right) - g \sum_{\mathrm{i,\,A}} \mathcal{S}_{\mathrm{i}}^\dagger \left(t_{\mathrm{A}} \mathcal{D}_{\mathrm{A}} \right) \mathcal{S}_{\mathrm{i}} \\
&- \sum_{\mathrm{p}} \xi_{\mathrm{p}} \mathcal{D}_{\mathrm{p}} + \sum_{\mathrm{i}} \left(-i \left. \frac{\partial \hat{f}}{\partial \hat{\mathcal{S}}_{\mathrm{i}}} \right|_{\hat{\mathcal{S}} = \mathcal{S}} \mathcal{F}_{\mathrm{i}} + i \left(\frac{\partial \hat{f}}{\partial \hat{\mathcal{S}}_{\mathrm{i}}} \right)^\dagger \bigg|_{\hat{\mathcal{S}} = \mathcal{S}} \mathcal{F}_{\mathrm{i}}^\dagger \right) \\
&- \frac{1}{2} \sum_{\mathrm{i,\,j}} \bar{\psi}_{\mathrm{i}} \left(\left. \frac{\partial^2 \hat{f}}{\partial \hat{\mathcal{S}}_{\mathrm{i}} \, \partial \hat{\mathcal{S}}_{\mathrm{j}}} \right|_{\hat{\mathcal{S}} = \mathcal{S}} \frac{1 - \gamma_5}{2} + \left(\frac{\partial^2 \hat{f}}{\partial \hat{\mathcal{S}}_{\mathrm{i}} \, \partial \hat{\mathcal{S}}_{\mathrm{j}}} \right)^\dagger \bigg|_{\hat{\mathcal{S}} = \mathcal{S}} \frac{1 + \gamma_5}{2} \right) \psi_{\mathrm{i}} \, . \quad (1.22)
\end{aligned}
$$

The auxiliary fields, $\mathcal{D}$ and $\mathcal{F}$, can further be removed using the Euler-Lagrange equations of motion.

1.2.1 Global supersymmetry breaking

An essential part of SUSY is how to break it. Spontaneous global SUSY breaking occurs through either F-type or D-type breaking,

$$
\langle 0 \left| \mathcal{F}_{\mathrm{i}} \right| 0 \rangle \neq 0 \quad \mathrm{or} \tag{1.23a}
$$

$$
\langle 0 \left| \mathcal{D}_{\mathrm{i}} \right| 0 \rangle \neq 0 \, . \tag{1.23b}
$$

When either of these conditions is met, the associated auxiliary field develops a VEV. Spontaneous global SUSY breaking leads to non-phenomenological results, e.g. some supersymmetric particles (sparticles) will have lighter SUSY partners.

Alternatively, to avoid such non-phenomenological results, the effects of SUSY

breaking can be introduced explicitly. In doing so, certain terms, which will break SUSY softly, can be added into the Lagrangian by hand to parametrize our ignorance of the exact details of SUSY breaking. The terms that will break SUSY softly are:

- linear $(\mathcal{S}_i)$,

- bilinear $(\mathcal{S}_i \mathcal{S}_j)$,

- trilinear $(\mathcal{S}_i \mathcal{S}_j \mathcal{S}_k)$,

- scalar masses, m, and

- gaugino masses, M,

The explicit soft SUSY breaking (SSB) Lagrangian is

$$\mathcal{L}_{SSB} = \sum_i C_i \, \mathcal{S}_i + \sum_{i,\,j} B_{ij} \, \mu_{ij} \, \mathcal{S}_i \, \mathcal{S}_j + \sum_{i,j,k} A_{ijk} \, f_{ijk} \, \mathcal{S}_i \, \mathcal{S}_j \, \mathcal{S}_k + \mathrm{h.c.}$$

$$- \sum_{i,\,j} \mathcal{S}_i^\dagger \, m_{ij}^2 \, \mathcal{S}_j - \frac{1}{2} \sum_{A,\,\alpha} M_{A\alpha} \, \bar{\lambda}_{A\alpha} \, \lambda_{A\alpha} - \frac{i}{2} \sum_{A,\,\alpha} M'_{A\alpha} \, \bar{\lambda}_{A\alpha} \, \gamma_5 \, \lambda_{A\alpha} \,, \quad (1.24)$$

where α runs over the different factors of the gauge group.

1.2.2 Local supersymmetry breaking

SUSY cannot be broken in the same way as SM symmetries, such as $SU(2)$ through the Higgs mechanism. If SUSY were broken in the same way, then the SUSY masses would be identical to their SM partners. The breaking of SUSY is done in a hidden sector, kept separate from the observable sector in which the SM and MSSM reside. Because SUSY breaking is in the hidden sector, the exact details are unknown. Global SUSY breaking can be either spontaneous or explicit;

the latter is ad hoc by introducing certain terms by hand into the Lagrangian. The alternative is to break SUSY locally. In local SUSY, a spin 3/2 field, ψ_μ, must be introduced[17]. To maintain SUSY, this field comes with a partner, which is a spin 2 field, $g_{\mu\nu}$. These can be recognized as the gravitino and graviton fields. Fortunately, the graviton interacts with all particles. Consequently, the gravitino interacts with all fields, making supergravity (SUGRA) a perfect choice to convey information from the hidden sector to the observable sector. If local SUSY is broken spontaneously in a hidden sector, then the gravitino obtains a mass, $m_{3/2}$, via the super-Higgs mechanism. This then induces explicit soft SUSY breaking terms for the visible sector fields. In doing so, *all* supersymmetric particle (sparticle) masses and soft terms are all proportional to the gravitino mass[18–20]. The specific ratio of the sparticle masses is determined by the form of hidden sector SUSY breaking.

These terms come with a non-renormalizable $1/M_P$ factor. The gravitino mass is integrated out, taking the low-energy limit with the Planck mass taken to infinity, $M_P \to \infty$ while keeping $m_{3/2}$ fixed. This leads to an effective theory of gravity. The gravitino mass can be expressed as in terms of the hidden sector SUSY breaking scale, m, and reduced Planck scale, $M_P = M_{PL}/\sqrt{8\pi} \approx 2.4 \times 10^{18}$ GeV as

$$m_{3/2} = m^2/M_P \ . \tag{1.25}$$

If $\mathcal{O}(m_{3/2}) \approx 10^3$ GeV to 10^4 GeV, then $m \approx 10^{11}$ GeV to 10^{12} GeV.

1.2.3 Minimal Supersymmetric Standard Model

The Minimal Supersymmetric Standard Model (MSSM) is the smallest extension of the SM to include supersymmetry. To extend the SM to include SUSY, a number of steps must be taken:

1. Choose gauge symmetry to be the SM gauge group, $SU(3)_C \otimes SU(2)_L \otimes U(1)_Y$. The SM gauge bosons become gauge superfields, listed in table 1.3.

2. Introduce the supersymmetric matter content, realized as left-chiral scalar superfields with the same gauge quantum numbers as the SM counterparts, listed in table 1.3 the superfields are denoted by a tilde.

3. Choose the form of an superpotential, $\hat{f}$, analytic function of left-chiral superfields, $\mathcal{S}_L$.

4. Extend the Higgs sector to a two Higgs doublet, $\hat{H}_u$ with $Y = 1$ and $\hat{H}_d$ with $Y = -1$.

5. Choose form of a flat Kähler potential.

6. Determine supersymmetric Lagrangian including all possible SSB terms, explicit form of which are determined by the low energy effective SUGRA.

The superpotential describes the interactions between chiral superfields. For the MSSM, the superfield is written in terms of the fields listed in table 1.3 as

$$\hat{f} = \mu \hat{H}_u^{\mathrm{a}} \hat{H}_{d\mathrm{a}} + \sum_{\mathrm{i,j}=1,2,3} \left[(\mathbf{f}_u)_{\mathrm{ij}} \epsilon_{\mathrm{ab}} \hat{Q}_{\mathrm{i}}^{\mathrm{a}} \hat{h}_u^{\mathrm{b}} \hat{U}_{\mathrm{j}}^c + (\mathbf{f}_d)_{\mathrm{ij}} \hat{Q}_{\mathrm{i}}^{\mathrm{a}} \hat{H}_{d\mathrm{a}} \hat{D}_{\mathrm{j}}^c + (\mathbf{f}_e)_{\mathrm{ij}} \hat{L}_{\mathrm{i}}^{\mathrm{a}} \hat{H}_{d\mathrm{a}} \hat{E}_{\mathrm{j}}^c \right] \ , \tag{1.26}$$

where the indices a and b are $SU(2)$ doublet indices, ϵ_{ab} is the completely antisymmetric $SU(2)$ tensor with $\epsilon_{12} = 1$, and the $\mathbf{f}$ terms are 3×3 Yukawa coupling matrices with i and j indicating the generations of interacting fields. The μ term is

Superfield	$SU(3)_C$	$SU(2)_L$	$U(1)_Y$
$\hat{L}_3,\ \hat{L}_2,\ \hat{L}_1 = \begin{bmatrix} \tilde{\nu}_L \\ \tilde{e}_L \end{bmatrix}$	**1**	**2**	-1
$\tilde{\tau}_R,\ \tilde{\mu}_R,\ \tilde{e}_R$	**1**	**1**	2
$\widehat{Q}_3,\ \widehat{Q}_2,\ \widehat{Q}_1 = \begin{bmatrix} \tilde{u}_L \\ \tilde{d}_L \end{bmatrix}$	**3**	**2**	1/3
$\tilde{t}_R,\ \tilde{c}_R,\ \tilde{u}_R$	**3***	**1**	-4/3
$\tilde{b}_R,\ \tilde{s}_R,\ \tilde{d}_R$	**3***	**1**	2/3
$\widehat{H}_u = \begin{bmatrix} \hat{h}_u^+ \\ \hat{h}_u^0 \end{bmatrix}$	**1**	**2**	1
$\widehat{H}_d = \begin{bmatrix} \hat{h}_d^+ \\ \hat{h}_d^0 \end{bmatrix}$	**1**	**2***	1
$\hat{g}_{1,\dots,8}$	**8**	**1**	0
$\widehat{W}_{1,2,3}$	**1**	**3**	0
$\widehat{B}$	**1**	**1**	0

Table 1.3: The matter, Higgs, and gauge superfield content of the MSSM, with gauge quantum numbers.

the superpotential Higgs mass term, referred to later as the superpotential μ term. The Yukawa interactions arise through the superpotential since the SSB terms are free of chiral interactions. In the SM, from eq. (1.6), the up-type quark Yukawa interaction contains the conjugate of the Higgs field. Because the superpotential is analytic in fields, and conjugate terms are forbidden, the Higgs sector must be extended to include a second Higgs doublet, $\widehat{H}_u$, with hypercharge $Y = 1$, which couples to the up-type particles separately from the down-type Higgs, $\widehat{H}_d$ with hypercharge $Y = -1$, which couples to the down-type particles. The extension of the Higgs sector is detailed in section 1.2.4 and SUSY masses are determined in section 1.2.5.

1.2.4 Higgs mechanism

The Higgs mechanism follows similar to the SM Higgs mechanism; however, the Higgs sector must be extended to a two Higgs doublet, instead of a single doublet.

Having two Higgs doublets allows coupling to both up-type or down-type quarks and leptons. The scalar potential for the neutral components is

$$
\begin{aligned}
V_{\text{scalar}} = {} & \left(m_{H_u}^2 + \mu^2\right)\left|h_u^0\right|^2 + \left(m_{H_d}^2 + \mu^2\right)\left|h_d^0\right|^2 \\
& - B\mu\left(h_u^0 h_d^0 + \text{h.c.}\right) + \frac{1}{8}\left(g^2 + g'^2\right)\left(\left|h_u^0\right|^2 - \left|h_d^0\right|^2\right)^2 .
\end{aligned}
\tag{1.27}
$$

Electroweak symmetry is broken when $m_{H_u}^2$ becomes negative. When that happens, the Higgs fields develop VEVs $\langle h_u^0\rangle \equiv v_u$ and $\langle h_d^0\rangle \equiv v_d$. The ratio of VEVs is denoted as

$$
\tan\beta \equiv \frac{v_u}{v_d} .
\tag{1.28}
$$

Setting $\partial V/\partial h_u^{0*} = 0$, $\partial V/\partial h_d^{0*} = 0$, and enforcing the origin is a local maximum (to avoid the trivial solution of $v_u = v_d = 0$) leads to the minimization conditions

$$
B\mu = \frac{\left(m_{H_u}^2 + m_{H_d}^2 + 2\mu^2\right)\sin(2\beta)}{2} \quad \text{and}
\tag{1.29a}
$$

$$
\mu^2 = \frac{m_{H_d}^2 + m_{H_u}^2 \tan^2\beta}{\tan^2\beta - 1} - \frac{m_Z^2}{2} .
\tag{1.29b}
$$

After the electroweak breaking, three degrees of freedom go into the $W^\pm$ and Z boson masses as before, leaving five degrees of freedom left over. These lead to five physical Higgs boson states (opposed to only one in the SM), being the light Higgs, h; heavy Higgs, H; two charged Higgs, $H^\pm$; and pseudo-scalar Higgs, A.

1.2.5 Supersymmetric masses

To obtain the masses of supersymmetric particles, the soft SUSY breaking terms listed in section 1.2.1 are used. Detailing the general procedure, the top squark will be used as an example. There is a bilinear and trilinear Higgs contribution to the superpotential of the form

$$\mu \, \hat{h}_u^0 \, \hat{h}_d^0 + f_t \, \hat{t} \, \hat{h}_u^0 \, \hat{T}^c \in \hat{f} \ . \tag{1.30}$$

From the $-\sum_i \left| \partial \hat{f} / \partial \hat{\mathcal{S}}_i \right|^2_{\hat{\mathcal{S}}=\mathcal{S}}$ contribution, taking $\hat{\mathcal{S}} = \hat{T}^c$ yields

$$-m_t^2 \left(\tilde{t}_L^\dagger \tilde{t}_L + \tilde{t}_R^\dagger \tilde{t}_R \right) \in \mathcal{L} \tag{1.31}$$

and taking $\hat{\mathcal{S}}_i = \hat{h}_u^0$ yields

$$-\mu \, m_t \cot \beta \left(\tilde{t}_L^\dagger \tilde{t}_R + \tilde{t}_R^\dagger \tilde{t}_L \right) \ . \tag{1.32}$$

From the trilinear terms, there is a term of the form $\left(A_t \, f_t \, \tilde{t}_L \, h_u^0 \tilde{t}_R^\dagger + \text{h.c.} \right) \in \mathcal{L}$, which leads to stop squark mixing of

$$-\left(-A_t \, m_t \right) \left(\tilde{t}_L^\dagger \tilde{t}_R + \tilde{t}_R^\dagger \tilde{t}_L \right) \ . \tag{1.33}$$

The D-term contributions lead to a mass squared term of

$$m_{D-\text{term}}^2 = m_Z^2 \cos(2\beta) \left(T_3 - Q \sin^2 \theta_W \right) \ . \tag{1.34}$$

Combining all these contributions together, the mass term in the Lagrangian can be written as

$$- \begin{bmatrix} \tilde{t}_L^\dagger & \tilde{t}_R^\dagger \end{bmatrix} \mathcal{M}_{\tilde{t}}^2 \begin{bmatrix} \tilde{t}_L \\ \tilde{t}_R \end{bmatrix} \in \mathcal{L} \, , \tag{1.35}$$

where the $\mathcal{M}_{\tilde{t}}^2$ matrix is given by

$$\mathcal{M}_{\tilde{t}}^2 = \begin{bmatrix} m_{\tilde{t}_L}^2 + m_t^2 + D\left(\tilde{t}_L\right) & m_t\left(-A_t + \mu \cot \beta\right) \\ m_t\left(-A_t + \mu \cot \beta\right) & m_{\tilde{t}_R}^2 + m_t^2 + D\left(\tilde{t}_R\right) \end{bmatrix} \, , \tag{1.36}$$

with

$$D\left(\tilde{t}_L\right) = m_Z^2 \cos(2\beta) \left(\frac{1}{2} - \frac{2}{3} \sin^2 \theta_W \right) \tag{1.37a}$$

$$D\left(\tilde{t}_R\right) = m_Z^2 \cos(2\beta) \left(\frac{2}{3} \sin^2 \theta_W \right) \, . \tag{1.37b}$$

The eigenvalues of the $\mathcal{M}_{\tilde{t}}^2$ matrix yield the light and heavy stop masses of

$$m_{\tilde{t}_{1,2}}^2 = \frac{1}{2} \left(m_{\tilde{t}_L}^2 + m_{\tilde{t}_R}^2 \right) + \frac{1}{4} m_Z^2 \cos(2\beta) + m_t^2$$

$$\mp \sqrt{\left(\frac{1}{2} \left(m_{\tilde{t}_L}^2 - m_{\tilde{t}_R}^2 \right) + m_Z^2 \cos(2\beta) \left(\frac{1}{4} - \frac{2}{3} x_W \right) \right)^2 + m_t^2 \left(\mu \cot \beta - A_t \right)^2} \, , \tag{1.38}$$

where $x_W \equiv \sin^2\left(\theta_W\right)$. Following a similar procedure, all the MSSM mass eigenstates can be obtained, which are listed in table 1.4. These masses are important in section 1.2.6, where radiative corrections to the scalar potential will be calculated, contributing to an expression for the amount of fine-tuning.

$$m_{\tilde{t}_{1,2}}^2 = \frac{1}{2}\left(m_{\tilde{t}_L}^2 + m_{\tilde{t}_R}^2\right) + \frac{1}{4}m_Z^2\cos(2\beta) + m_t^2$$

$$\mp\sqrt{\left(\frac{1}{2}\left(m_{\tilde{t}_L}^2 - m_{\tilde{t}_R}^2\right) + m_Z^2\cos(2\beta)\left(\frac{1}{4} - \frac{2}{3}x_W\right)\right)^2 + m_t^2\left(\mu\cot\beta - A_t\right)^2}$$

$$m_{\tilde{b}_{1,2}}^2 = \frac{1}{2}\left(m_{\tilde{b}_L}^2 + m_{\tilde{b}_R}^2\right) - \frac{1}{4}m_Z^2\cos(2\beta) + m_b^2$$

$$\mp\sqrt{\left(\frac{1}{2}\left(m_{\tilde{b}_L}^2 - m_{\tilde{b}_R}^2\right) - m_Z^2\cos(2\beta)\left(\frac{1}{4} - \frac{1}{3}x_W\right)\right)^2 + m_b^2\left(\mu\tan\beta - A_b\right)^2}$$

$$m_{\tilde{\tau}_{1,2}}^2 = \frac{1}{2}\left(m_{\tilde{\tau}_L}^2 + m_{\tilde{\tau}_R}^2\right) - \frac{1}{4}m_Z^2\cos(2\beta) + m_\tau^2$$

$$\mp\sqrt{\left(\frac{1}{2}\left(m_{\tilde{\tau}_L}^2 - m_{\tilde{\tau}_R}^2\right) - m_Z^2\cos(2\beta)\left(\frac{1}{4} - x_W\right)\right)^2 + m_\tau^2\left(\mu\tan\beta - A_\tau\right)^2}$$

$$m_{h,H}^2 = \frac{1}{2}\left(\left(m_A^2 + m_Z^2\right) \mp \sqrt{\left(m_A^2 + m_Z^2\right)^2 - 4m_A^2 m_Z^2\cos(2\beta)}\right)$$

$$m_{H^\pm}^2 = m_A^2 + m_W^2$$

$$m_{\widetilde{W}_{1,2}}^2 = \frac{1}{2}\left(\left(\mu^2 + M_2^2 + 2m_W^2\right)\right.$$

$$\left.\mp\sqrt{\left(\mu^2 - M_2^2\right)^2 + 4m_W^2\left(m_X^2\cos^2(2\beta) + \mu^2 + M_2^2 - 2\mu M_2\sin(2\beta)\right)}\right)$$

$$m_{\widetilde{Z}_{1,2,3,4}} = \mathrm{diag}\begin{bmatrix} 0 & \mu & -\frac{gv_u}{\sqrt{2}} & \frac{g'v_u}{\sqrt{2}} \\ \mu & 0 & \frac{gv_d}{\sqrt{2}} & -\frac{g'v_d}{\sqrt{2}} \\ -\frac{gv_u}{\sqrt{2}} & \frac{gv_d}{\sqrt{2}} & M_2 & 0 \\ \frac{g'v_u}{\sqrt{2}} & -\frac{g'v_d}{\sqrt{2}} & 0 & M_1 \end{bmatrix}$$

Table 1.4: List of the masses of $\tilde{t}_{1,2}$, $\tilde{b}_{1,2}$, $\tilde{\tau}_{1,2}$, h, H, $H^\pm$, $\widetilde{W}_{1,2}$, and $\widetilde{Z}_{1,2,3,4}$ obtained from explicit global SUSY breaking.

1.2.6 Radiative corrections

Radiative corrections can be introduced to the Higgs potential additively,

$$V_{\text{Higgs}} = V_{\text{tree}} + \Delta V \ , \tag{1.39}$$

where V_{tree} is given in eq. (1.27). The radiative corrections, ΔV, include all fields that couple to the Higgs fields and can be expressed (in the effective potential approximation using the dimensional regularization scheme, $\overline{DR}$) as[21]

$$\Delta V = \sum_i \frac{(-1)^{2s_i}}{64\pi^2} (2s_i + 1)\, c_i\, m_i^4 \left(\ln\left(\frac{m_i^2}{Q^2}\right) - \frac{3}{2} \right) \ , \tag{1.40}$$

where s_i and m_i^2 are the spin and Higgs field dependent mass squared matrix, $c_i = c_{\text{color}} c_{\text{charge}}$ with $c_{\text{color}} = 3(1)$ for colored (uncolored) particles and $c_{\text{charge}} = 2(1)$ for charged(neutral) particles. The derivatives of the potential are defined as

$$\Sigma_{u,d} \equiv \left. \frac{\partial\,(\Delta V)}{\partial\, h_{u,d}} \right|_{\text{min}} . \tag{1.41}$$

By $SU(2)$ invariance, these can be expressed in terms of the VEVs, v_u and v_d, as

$$\Sigma_u = \Sigma_u^u v_u + \Sigma_u^d v_d \ , \text{ and} \tag{1.42a}$$

$$\Sigma_d = \Sigma_u^d v_u + \Sigma_d^d v_d \ , \tag{1.42b}$$

where

$$\Sigma_u^u \equiv \left. \frac{\partial \left(\Delta V \right)}{\partial \left(|h_u|^2 \right)} \right|_{\text{min}} , \tag{1.43a}$$

$$\Sigma_d^d \equiv \left. \frac{\partial \left(\Delta V \right)}{\partial \left(|h_d|^2 \right)} \right|_{\text{min}} , \quad \text{and} \tag{1.43b}$$

$$\Sigma_d^u = \Sigma_u^d \equiv \left. \frac{\partial \left(\Delta V \right)}{\partial \left(h_u h_d + \text{c.c.} \right)} \right|_{\text{min}} . \tag{1.43c}$$

Written more explicitly, using eq. (1.40),

$$\Sigma_u^u = \sum_i \frac{1}{32\pi^2} (-1)^{2s_i} (2s_i + 1) \, c_i \, F(m_i^2) \left. \frac{\partial \left(m_i^2 \right)}{\partial \left(|h_u|^2 \right)} \right|_{\text{min}} , \tag{1.44a}$$

$$\Sigma_d^d = \sum_i \frac{1}{32\pi^2} (-1)^{2s_i} (2s_i + 1) \, c_i \, F(m_i^2) \left. \frac{\partial \left(m_i^2 \right)}{\partial \left(|h_d|^2 \right)} \right|_{\text{min}} , \quad \text{and} \tag{1.44b}$$

$$\Sigma_d^u = \Sigma_u^d = \sum_i \frac{1}{32\pi^2} (-1)^{2s_i} (2s_i + 1) \, c_i \, F(m_i^2) \left. \frac{\partial \left(m_i^2 \right)}{\partial \left(h_u h_d + \text{c.c.} \right)} \right|_{\text{min}} , \tag{1.44c}$$

where

$$F \left(m^2 \right) \equiv m^2 \left(\ln \left(\frac{m^2}{Q^2} \right) - 1 \right) . \tag{1.45}$$

Using the Σs, the minimization conditions, eq. (1.29a), can be expressed as

$$\frac{m_Z^2}{2} = \frac{\left(m_{H_d}^2 + \Sigma_d^d \right) - \left(m_{H_u}^2 + \Sigma_u^u \right) \tan^2 \beta}{\tan^2 \beta - 1} - \mu^2 , \quad \text{and} \tag{1.46a}$$

$$B\mu = \left(\left(m_{H_u}^2 + \mu^2 + \Sigma_u^u \right) + \left(m_{H_d}^2 + \mu^2 + \Sigma_d^d \right) \right) \sin \beta \cos \beta + \Sigma_d^u . \tag{1.46b}$$

To list each field contribution to Σ_u^u and Σ_d^d explicitly, the mass matrices from section 1.2.1 are used. For the tops squarks,

$$m_{\tilde{t}_{1,2}}^2 = \frac{1}{2}\left(m_{\tilde{t}_L}^2 + m_{\tilde{t}_R}^2\right) + \frac{1}{4}m_Z^2\cos(2\beta) + m_t^2$$

$$\mp\sqrt{\left(\frac{1}{2}\left(m_{\tilde{t}_L}^2 - m_{\tilde{t}_R}^2\right) + m_Z^2\cos(2\beta)\left(\frac{1}{4} - \frac{2}{3}x_W\right)\right)^2 + m_t^2\left(\mu\cot\beta - A_t\right)^2} \,,$$

$$(1.47)$$

Substituting in the explicit dependence on the Higgs fields,

- $\tan\beta = \dfrac{h_u}{h_d} \implies \cos(2\beta) = \dfrac{h_d^2 - h_u^2}{h_u^2 + h_d^2}$,

- $m_Z^2 = \dfrac{g + g'^2}{2}\left(h_u^2 + h_d^2\right) = 4g_Z^2\left(h_u^2 + h_d^2\right)$, and

- $m_t = f_t h_u$,

the $\tilde{t}_{1,2}$ contributions to Σ can be calculated, with $s_i = 0$, $c_i = (3)(2)$, to be

$$\Sigma_u^u\left(\tilde{t}_{1,2}\right) = \frac{3}{16\pi^2}\, F\left(m_{\tilde{t}_{1,2}}^2\right)\left(f_t^2 - g_Z^2 \mp \frac{f_t^2 A_t^2 - 8g_Z^2\left(\frac{1}{4} - \frac{2}{3}x_W\right)\Delta_t}{m_{\tilde{t}_2}^2 - m_{\tilde{t}_1}^2}\right) \,, \quad (1.48\text{a})$$

$$\Sigma_d^d\left(\tilde{t}_{1,2}\right) = \frac{3}{16\pi^2}\, F\left(m_{\tilde{t}_{1,2}}^2\right)\left(g_Z^2 \mp \frac{f_t^2 \mu^2 + 8g_Z^2\left(\frac{1}{4} - \frac{2}{3}x_W\right)\Delta_t}{m_{\tilde{t}_2}^2 - m_{\tilde{t}_1}^2}\right) \,, \qquad (1.48\text{b})$$

$$\Delta_t \equiv \frac{1}{2}\left(m_{\tilde{t}_L}^2 - m_{\tilde{t}_R}^2\right)m_Z^2\cos(2\beta)\left(\frac{1}{4} - \frac{2}{3}x_W\right) \,.$$

The other contributions can be found in a similar manner. Table 1.5 lists the results for $\tilde{t}_{1,2}$, $\tilde{b}_{1,2}$, $\tilde{\tau}_{1,2}$, h, H, $\widetilde{W}_{1,2}$, and $\widetilde{Z}_{1,2,3,4}$.

$\tilde{t}_{1,2}$	$\sum_u^u$	$\dfrac{3}{16\pi^2}\,F\!\left(m_{\tilde{t}_{1,2}}^2\right)\left(f_t^2 - g_Z^2 \mp \dfrac{f_t^2 A_t^2 - 8g_Z^2\left(\frac{1}{4} - \frac{2}{3}x_w\right)\Delta_t}{m_{\tilde{t}_2}^2 - m_{\tilde{t}_1}^2}\right)$
	$\sum_d^d$	$\dfrac{3}{16\pi^2}\,F\!\left(m_{\tilde{t}_{1,2}}^2\right)\left(g_Z^2 \mp \dfrac{f_t^2 \mu^2 + 8g_Z^2\left(\frac{1}{4} - \frac{2}{3}x_w\right)\Delta_t}{m_{\tilde{t}_2}^2 - m_{\tilde{t}_1}^2}\right)$
	$\Delta_t \;=\; \frac{1}{2}\left(m_{\tilde{t}_L}^2 - m_{\tilde{t}_R}^2\right) + m_Z^2\cos(2\beta)\left(\frac{1}{4} - \frac{2}{3}x_w\right)$	
$\tilde{b}_{1,2}$	$\sum_u^u$	$\dfrac{3}{16\pi^2}\,F\!\left(m_{\tilde{b}_{1,2}}^2\right)\left(g_Z^2 \mp \dfrac{f_b^2 \mu^2 - 8g_Z^2\left(\frac{1}{4} - \frac{1}{3}x_w\right)\Delta_b}{m_{\tilde{b}_2}^2 - m_{\tilde{b}_1}^2}\right)$
	$\sum_d^d$	$\dfrac{3}{16\pi^2}\,F\!\left(m_{\tilde{b}_{1,2}}^2\right)\left(f_b^2 - g_Z^2 \mp \dfrac{f_b^2 A_b^2 - 8g_Z^2\left(\frac{1}{4} - \frac{1}{3}x_w\right)\Delta_b}{m_{\tilde{b}_2}^2 - m_{\tilde{b}_1}^2}\right)$
	$\Delta_b \;=\; \frac{1}{2}\left(m_{\tilde{b}_L}^2 - m_{\tilde{b}_R}^2\right) - m_Z^2\cos(2\beta)\left(\frac{1}{4} - \frac{1}{3}x_w\right)$	
$\tilde{\tau}_{1,2}$	$\sum_u^u$	$\dfrac{1}{16\pi^2}\,F\!\left(m_{\tilde{\tau}_{1,2}}^2\right)\left(g_Z^2 \mp \dfrac{f_\tau^2 \mu^2 + 8g_Z^2\left(\frac{1}{4} - x_w\right)\Delta_\tau}{m_{\tilde{\tau}_2}^2 - m_{\tilde{\tau}_1}^2}\right)$
	$\sum_d^d$	$\dfrac{1}{16\pi^2}\,F\!\left(m_{\tilde{\tau}_{1,2}}^2\right)\left(f_\tau^2 - g_Z^2 \mp \dfrac{f_\tau^2 A_\tau^2 - 8g_Z^2\left(\frac{1}{4} - x_w\right)\Delta_\tau}{m_{\tilde{\tau}_2}^2 - m_{\tilde{\tau}_1}^2}\right)$
	$\Delta_\tau \;=\; \frac{1}{2}\left(m_{\tilde{\tau}_L}^2 - m_{\tilde{\tau}_R}^2\right) - m_Z^2\cos(2\beta)\left(\frac{1}{4} - x_w\right)$	
h,H	$\sum_u^u$	$\dfrac{g_Z^2}{16\pi^2}\,F\!\left(m_{h,H}^2\right)\left(1 \mp \dfrac{m_Z^2 + m_A^2\left(1 + 4\cos(2\beta) + 2\cos^2(2\beta)\right)}{m_H^2 - m_h^2}\right)$
	$\sum_d^d$	$\dfrac{g_Z^2}{16\pi^2}\,F\!\left(m_{h,H}^2\right)\left(1 \mp \dfrac{m_Z^2 + m_A^2\left(1 - 4\cos(2\beta) + 2\cos^2(2\beta)\right)}{m_H^2 - m_h^2}\right)$
$H^\pm$	$\sum_u^u = \sum_d^d$	$\dfrac{g^2}{32\pi^2}\,F\left(m_{H^\pm}^2\right)$

$\widetilde{W}_{1,2}$	$\sum_u^u$	$\dfrac{-g^2}{16\pi^2}\, F\!\left(m_{\widetilde{W}_{1,2}}^2\right)\left(1 \mp \dfrac{M_2^2 + \mu^2 - 2m_W^2\cos(2\beta)}{m_{\widetilde{W}_2}^2 - m_{\widetilde{W}_1}^2}\right)$
	$\sum_d^d$	$\dfrac{-g^2}{16\pi^2}\, F\!\left(m_{\widetilde{W}_{1,2}}^2\right)\left(1 \mp \dfrac{M_2^2 + \mu^2 + 2m_W^2\cos(2\beta)}{m_{\widetilde{W}_2}^2 - m_{\widetilde{W}_1}^2}\right)$
$\widetilde{Z}_i$	$\sum_u^u$	$\dfrac{1}{16\pi^2}\dfrac{F\!\left(m_{\widetilde{Z}_i}^2\right)}{D\!\left(\widetilde{Z}_i\right)}\left(K\!\left(\widetilde{Z}_i\right) - 16\,g_Z^2\,\mu^2\,m_Z^2\,\cos^2\beta\left(m_{\widetilde{Z}_i}^2 - m_{\widetilde{\gamma}}^2\right)\right)$
	$\sum_d^d$	$\dfrac{1}{16\pi^2}\dfrac{F\!\left(m_{\widetilde{Z}_i}^2\right)}{D\!\left(\widetilde{Z}_i\right)}\left(K\!\left(\widetilde{Z}_i\right) - 16\,g_Z^2\,\mu^2\,m_Z^2\,\sin^2\beta\left(m_{\widetilde{Z}_i}^2 - m_{\widetilde{\gamma}}^2\right)\right)$
	$D \;=\; \displaystyle\prod_{i\neq j}\left(m_{\widetilde{Z}_i}^2 - m_{\widetilde{Z}_j}^2\right)$	
	$\begin{aligned} K \;=\;& m_{\widetilde{Z}_i}^6\left(g^2 + g'^2\right) + m_{\widetilde{Z}_i}^4\Big(g^2(M_1^2 + \mu^2) + g'^2(M_2^2 + \mu^2) \\ &+ (g^2 + g'^2)\,m_Z^2\Big) - m_{\widetilde{Z}_i}^2\Big(\mu^2(g^2 M_1^2 + g'^2 M_2^2) \\ &+ (g^2 + g'^2)\,m_Z^2\left(M_1\cos^2\theta_W + M_2\sin^2\theta_W\right)\Big) \end{aligned}$	

Table 1.5: List of contributions to $\sum_u^u$ and $\sum_d^d$ from $\tilde{t}_{1,2}$, $\tilde{b}_{1,2}$, $\tilde{\tau}_{1,2}$, h, H, $H^\pm$, $\widetilde{W}_{1,2}$, and $\widetilde{Z}_{1,2,3,4}$. The masses of the sparticles are listed in table 1.4.

Chapter 2

Naturalness

Naturalness is the idea of how natural a theory is, or how likely it is to be realized by nature. If the standard model was valid up to an energy scale $\Lambda \gg m_{\text{weak}}$ and there was nothing else, there would be a large amount of fine-tuning in the Higgs boson mass. Considering the Higgs mass to next-to-leading order (NLO), using Pauli-Villars regularization, the leading radiative correction to the Higgs mass is

$$\delta m_h^2(\Lambda) = \frac{3}{4\pi^2}\left(-\lambda_t^2 + \frac{g^2}{4} + \frac{g^2}{8\cos\theta_W} + \lambda\right)\Lambda^2 \, , \tag{2.1}$$

where λ_t is the top quark Yukawa coupling, g is the $SU(2)$ gauge coupling, λ is the Higgs field quartic coupling, and Λ is the UV cutoff scale. As Λ becomes large, the correction to the Higgs mass also becomes large. If the standard model is presumed to be valid up to the GUT scale, $\Lambda \approx 10^{19}$ GeV, then the Higgs mass would be fine-tuned to 1 part in 10^{28}.

Since the notion of naturalness may be a vague one, a concrete definition must be given. In this chapter, I will present three measures of naturalness used in literature[22]: Higgs mass (or large log), Δ_{HS}; Barbieri-Giudice, Δ_{BG}; and electroweak, Δ_{EW}. Through these, I will show that for an observable, $\mathcal{O}$, all independent contributions, p_i, must be $\lesssim \mathcal{O}$. If this does not hold for some parameter, p_i, then there is significant fine-tuning.

2.1 Higgs mass fine-tuning, Δ_{HS}

Just as the Higgs mass was of important significance in motivating SUSY through canceling quadratic divergences, so too was it a motivation for a measure of fine-tuning. The Higgs mass can be expressed as

$$m_h^2 \simeq \mu^2 + m_{H_u}^2\left(\Lambda\right) + \delta m_{H_u}^2\left(\Lambda\right). \tag{2.2}$$

Δ_{HS} is a measure of fine-tuning in the correction to the Higgs mass relative to the Higgs mass itself, simply expressed as

$$\Delta_{HS} = \frac{\delta m_{H_u}^2}{m_h^2}. \tag{2.3}$$

This gives a concrete measure of what is meant by fine-tuning: any contribution to an observable should be comparable or less than the measured value.

Often cited results of Δ_{HS} are limits on the third generation squarks. This can be seen from the running of the Higgs mass, which is expressed through the renormalization group equation (RGE)

$$\frac{dm_{H_u}^2}{dt} = \frac{1}{8\pi}\left(-\frac{3}{5}g_1^2 M_1^2 - 3g_2^2 M_2^2 + \frac{3}{10}g_1^2 S + 3f_t^2 X_t\right), \tag{2.4}$$

where $t = \ln\left(Q^2/Q_0^2\right)$, $S = m_{H_u}^2 - m_{H_d}^2 + \text{Tr}\left(\mathbf{m}_Q^2 - \mathbf{m}_L^2 - 2\mathbf{m}_U^2 + \mathbf{m}_D^2 + \mathbf{m}_E^2\right)$, and $X_t = m_{Q_3}^2 + m_{U_3}^2 + m_{H_u}^2 + A_t^2$. By omitting the gauge terms, S, and $m_{H_u}^2$ contribution to X_t, while keeping f_t and soft terms constant under variation in Q^2, eq. (2.4) reduces to

$$\delta m_{H_u}^2 = -\frac{3f_t^2}{8\pi}\left(m_{Q_3}^2 + m_{U_3}^2 + A_t^2\right)\ln\left(\frac{\Lambda^2}{m_{\tilde{t}_1}m_{\tilde{t}_2}}\right). \tag{2.5}$$

Maintaining a cutoff of fine-tuning up to 10%, or $\Delta_{HS} \lesssim 10$, yields third generation squark masses, $m_{\tilde{t}_{1,2}, \tilde{b}_1} \lesssim 600$ GeV. These highly search for third generation squarks have yet to be found, resulting in claims that SUSY is fine-tuned, unnatural, and in a crisis. As the data compounds and SUSY does not present herself, an increasing number of physicists are becoming skeptical of or abandoning SUSY. Although the ever increasing top squark mass limits bring skepticism, this skepticism should not be for SUSY, but rather, towards the measure of fine-tuning. There are two issues with Δ_{HS}:

- δm_{H_u} depends upon m_{H_u}, and

- SUSY is broken in a hidden sector $\xrightarrow[\text{SUGRA}]{} m_{H_u}^2 \approx m_{3/2}^2 > 0$.

The first point is problematic, because *any* quantity can seem fine-tuned if calculated prior to necessary cancelations. For a given constant, a, one would not say $\lim_{a \to \infty} (\mathcal{O} + a - a)$ is fine-tuned or divergent, it is clear that the expression is simply $\mathcal{O}$. In a similar way, one must combine dependent quantities together *prior* to calculating fine-tuning. This issue can be addressed and will be discussed in section 2.3. For the second point, because the Higgs mass is near the gravitino mass, one needs large radiative corrections to drive $m_{H_u}^2 < 0$. It is precisely this large log in eq. (2.5) that is needed to break EW symmetry.

2.2 Barbieri-Giudice fine-tuning, Δ_{BG}

Historically, fine-tuning was examined in context of the Z-boson mass. The Z-boson mass is well measured and can be calculated in terms of SUSY parameters

through the minimization of the MSSM potential as eq. (1.46a)

$$\frac{m_Z^2}{2} = \frac{(m_{H_d}^2 + \Sigma_d^d) - (m_{H_u}^2 + \Sigma_u^u) \tan^2 \beta}{\tan^2 \beta - 1} - \mu^2 \qquad (2.6a)$$

$$\simeq -m_{H_u}^2 - \Sigma_u^u - \mu^2 \,, \qquad (2.6b)$$

where Σ_d^d and Σ_u^u contain loop corrections to the effective potential (detailed in section 1.2.6) and eq. (2.6b) holds for moderate to large $\tan\beta$. Δ_{BG}[23, 24] is a measure of the dependence of m_Z on the fundamental high-scale parameters, p_i, through the sensitivity coefficients, c_i, as

$$\Delta_{BG} \equiv \max(c_i) \,, \quad \text{where} \quad c_i = \left| \frac{\partial \left(\ln m_Z^2 \right)}{\partial \left(\ln p_i \right)} \right| = \left| \frac{p_i}{m_Z^2} \frac{\partial \left(m_Z^2 \right)}{\partial p_i} \right|. \qquad (2.7)$$

Semi-analytic solutions to the RGEs can be used to express m_Z^2 in terms of SUSY parameters (with $\tan\beta = 10$) as[25–27]:

$$m_Z^2 = -\, 2.18\mu^2 + 3.84M_3^2 + 0.32M_3M_2 + 0.047M_1M_3 - 0.42M_2^2$$

$$+ 0.011M_2M_1 - 0.012M_1^2 - 0.65M_3A_t - 0.15M_2A_t$$

$$- 0.025M_1A_t + 0.22A_t^2 + 0.004M_3A_b$$

$$- 1.27m_{H_u}^2 - 0.053m_{H_d}^2$$

$$+ 0.73m_{Q_3}^2 + 0.57m_{U_3}^2 + 0.049m_{D_3}^2 - 0.052m_{L_3}^2 + 0.053m_{E_3}^2$$

$$+ 0.051m_{Q_2}^2 - 0.11m_{U_2}^2 + 0.051m_{D_2}^2 - 0.052m_{L_2}^2 + 0.053m_{E_2}^2$$

$$+ 0.051m_{Q_1}^2 - 0.11m_{U_1}^2 + 0.051m_{D_1}^2 - 0.052m_{L_1}^2 + 0.053m_{E_1}^2. \qquad (2.8)$$

From this, c_i must be calculated for each independent parameter to find the max-

imum, for example,

$$c_{m_{Q_3}^2} = 0.73 \; \frac{m_{Q_3}^2}{m_Z^2} \; . \qquad (2.9\text{a})$$

For $m_{Q_3} = 3$ TeV (consistent with m_h measurements), $c_{m_{Q_3}^2} = 790$ implying that $\Delta_{BG} \geq 790$, or fine-tuning to at least 0.13%. Instead of considering each parameter in m_Z as fundamental, perhaps one assumes unification between $m_{Q_3} = m_{U_3} = m_{H_u} \equiv m_0$, then one obtains

$$c_{m_0^2} = 0.03 \; \frac{m_0^2}{m_Z^2} \; , \qquad (2.9\text{b})$$

resulting in $\Delta_{BG} \geq 32$, significantly lower than eq. (2.9a). Thus, Δ_{BG} depends strongly on what one assumes to be independent parameters.

2.3 Electro-weak fine-tuning, Δ_{EW}

From section 2.1, one initial problem with Δ_{HS} is the dependence of δm_{H_u} on m_{H_u} itself. To ameliorate this, one can group the Higgs contributions in eq. (2.2) to become m_{H_u} at the weak scale, Q,

$$m_h^2\big|_{\text{phys}} = \mu^2 + \left(m_{H_u}^2 (\Lambda) + \delta m_{H_u}^2 (\Lambda) \right) \qquad (2.10\text{a})$$

$$m_h^2\big|_{\text{phys}} = \mu^2 + \qquad m_{H_u}(Q) \; . \qquad (2.10\text{b})$$

Since the previously mentioned Δ_{HS} and Δ_{BG} are both fine-tuning measures calculated at the GUT scale, eq. (2.10b) will motivate the electro-weak fine-tuning measure, Δ_{EW}, to be calculated at a lower energy scale, Q. While running from

the GUT scale to Q, the RGEs determine the mass of each particle through combinations of GUT scale input parameters. Doing so removes the question of which parameters are fundamental. Δ_{EW} is a comparison of each additive term on the right hand side of eq. (2.6a), p_i, to the value of m_Z itself as

$$\Delta_{EW} \equiv \max \left| \frac{p_i}{m_Z^2/2} \right|. \tag{2.11}$$

Either m_{H_u}, μ, or the largest sparticle contribution to Σ_u^u, listed in table 1.5, will limit Δ_{EW}, leading to two inevitable consequences:

- $m_{H_u}^2 \simeq -m_Z^2$ and

- $\mu^2 \simeq m_Z^2$,

the closer to m_Z, the lower the fine-tuning. The effects of Σ_u^u will depend on the SUSY model and parameters. More often than not, the third generation squarks will lead to the largest fine-tuning contributions to Σ_u^u. A concrete example is shown in section 2.4.

2.4   Fine-tuning: an example from NUHM

This section will consider Δ_{BG} and Δ_{EW} for the case of general SUGRA models, and show an example for a particular non-universal Higgs model (NUHM). From section 1.2.2, all the soft-SUSY breaking terms are multiples of the gravitino

mass, allowing each soft term to be expressed as

$$m_{H_u}^2 = a_{m_{H_u}} \cdot m_{3/2}^2 \tag{2.12a}$$

$$m_{Q_3}^2 = a_{Q_3} \cdot m_{3/2}^2 \tag{2.12b}$$

$$A_t = a_{A_t} \cdot m_{3/2} \tag{2.12c}$$

$$M_i = a_{M_i} \cdot m_{3/2} \tag{2.12d}$$

$$\cdots \; ,$$

where each a_i conveys the information of the breaking of SUSY in the hidden sector to the observable sector particles via the gravitino. Substituting these expressions in eq. (2.8), m_Z is simplified to[28]

$$m_Z^2 = -2.18\mu + a \cdot m_{3/2}^2 \; , \tag{2.13}$$

where a is a linear combination of each a_i. Now, calculating fine-tuning yields

$$c_{m_{3/2}^2} = \left| a \cdot \frac{m_{3/2}^2}{m_Z^2} \right| \tag{2.14a}$$

$$c_{\mu^2} = \left| -2.18 \, \frac{\mu^2}{m_Z^2} \right| \; . \tag{2.14b}$$

leading to more natural models than ones with independent parameters. As an example, for a NUHM model with

- $M_1 = M_2 = M_3 \equiv m_{1/2} = \frac{1}{3}m_{3/2}$,

- $A_\tau = A_b = A_t \equiv A_0 = 1.3m_{3/2}$,

- $m_{H_u} = m_{H_d} \equiv m_H = 1.1m_{3/2}$, and

31

- $m_{Q_i} = m_{U_i} = m_{D_i} = m_{L_i} = m_{E_i} \equiv m_0 = m_{3/2}$,

taking $m_{3/2} = 1$ TeV, μ becomes 270 GeV and

$$m_Z^2 = -2.18\,\mu^2 + 0.172\,m_{3/2}^2 \tag{2.15a}$$

$$\Delta_{BG}\left(\mu^2\right) = 19.7 \tag{2.15b}$$

$$\Delta_{BG}\left(m_{3/2}^2\right) = 20.7 \; . \tag{2.15c}$$

For this model, $\Delta_{BG} = 20.7$. Calculating Δ_{EW}, the largest contributions are

- $\Delta_{EW}\left(\mu^2\right) = 23.1$

- $\Delta_{EW}\left(m_{H_u}^2\right) = 18.5$

- $\Delta_{EW}\left(m_{H_d}^2\right) = 3.1$

- $\Delta_{EW}\left(\Sigma_u^u\left(\tilde{t}_2\right)\right) = 2.2$

- $\Delta_{EW}\left(\Sigma_u^u\left(\tilde{t}_1\right)\right) = 2.2$

This model yields comparable values between $\Delta_{BG} = 20.7$ and $\Delta_{EW} = 23.1$.

2.5 Fine-tuning limit

With the three definitions of fine-tuning, a question about naturalness is left unanswered, "When is a model unnatural?" Any cutoff for an acceptable amount of fine-tuning is arbitrary. Historically, acceptable values for Δ have been 10 to 30. With the increasing amount of parameter space experimentally ruled out, these values have increased to 100[27] or even 1000[29, 30]. Although this choice has variability, the heart of the question is, "How reasonable is it to believe the terms in eq. (2.6a) will conspire to yield the Z-boson mass?" To illustrate how

different these Δ values are, a particular SUSY model is chosen with parameters: $m_0 = 5$ TeV, $m_{1/2} = 700$ GeV, $A_0 = -8.0$ TeV, $\tan\beta = 10$, $m_A = 2.0$ TeV, and μ ranging in values from 150 GeV to 650 GeV. The ten largest contributions to Δ_{EW} for each μ value are shown in fig. 2.1. For lower μ, each parameter contributes approximately equally and comparable to m_Z. One could accept these values to add together to yield the Z-boson mass. As μ increases, the value of m_{H_u} is dialed precisely to produce the measured Z-boson mass. If this was not the case, how extraordinary would it be for nature to choose such a large negative value for m_{H_u} to get just the right cancellation!

Our convention is to take $\Delta_{EW} \leq 30$ as the fine-tuning cutoff, which visually, from fig. 2.1, seems reasonable. With $\Delta_{EW} \leq 30.$, the two consequences mentioned in section 2.3 become:

- -350^2 GeV$^2 \leq m_{H_u}^2 < 0$

- $\mu^2 \leq 350^2$ GeV^2 .
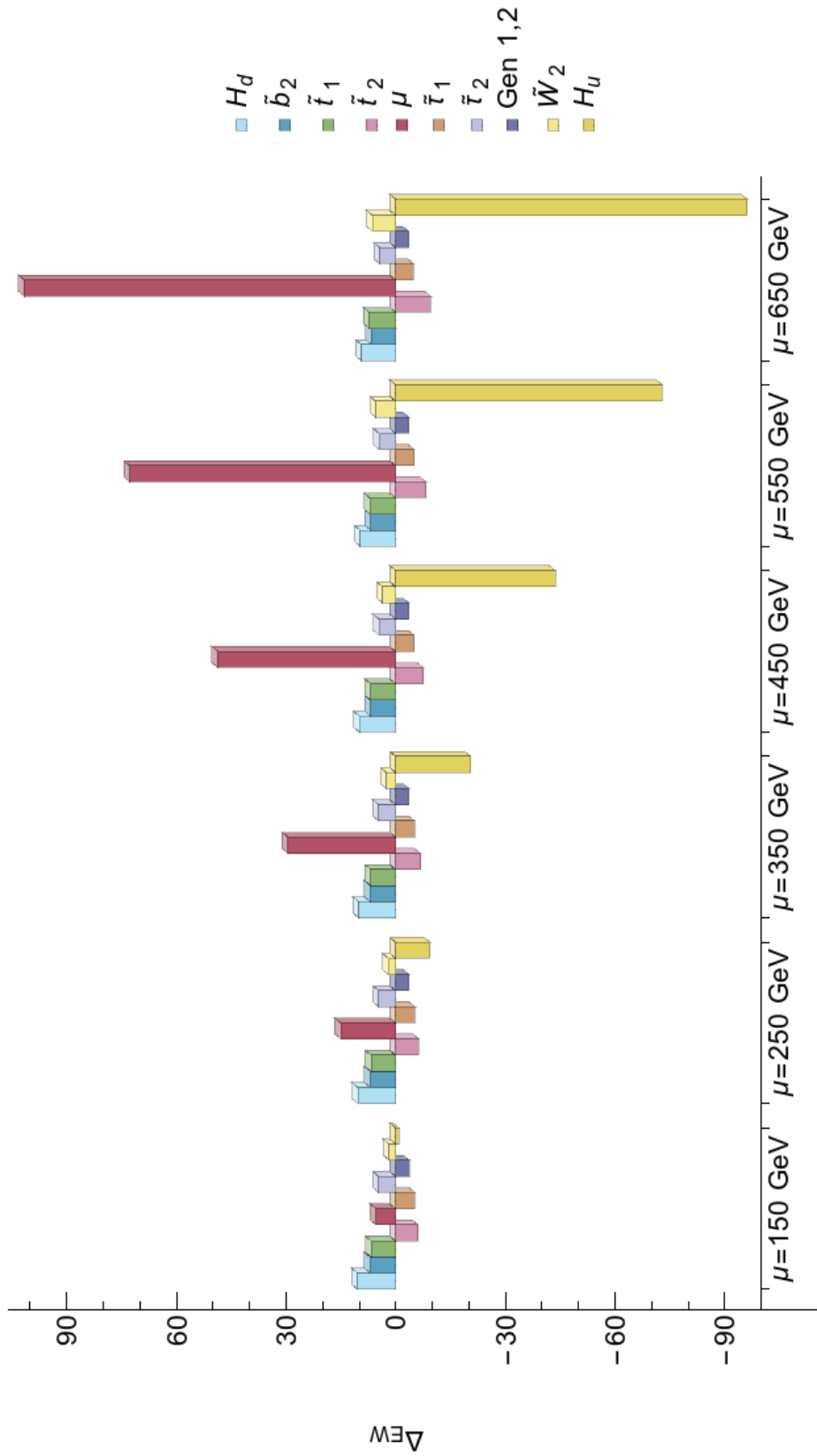
Figure 2.1: Plot of ten highest contributions to Δ_{EW} using parameters $m_0 = 5$ TeV, $m_{1/2} = 700$ GeV, $A_0 = -8$ TeV, $\tan \beta = 10$, $m_A = 2$ TeV, and μ ranging from 150 GeV to 650 GeV. Δ_{EW} is $\{10.4, 15.0, 29.5, 48.7, 72.8, 102.\}$ for μ of $\{150, 250, 350, 450, 550, 650\}$ GeV respectively.

2.6   Cost to goodness of fit

The fine-tuning, Δ, and the likelihood that the model fits the data, L, are not unrelated[31]. To enforce electro-weak symmetry breaking, the scalar potential must be minimized, leading to the two conditions eq. (1.46). The expression for m_Z is dependent on the parameters of the theory, p_i, and can be used to constrain the likelihood. Dirac delta distributions can be utilized in the likelihood to enforce measured values, e.g. m_Z measured to be m_Z^0. This constraint, as well as others, can be factored out of the likelihood. Additionally, nuisance parameters, α_i, can be marginalized (integrated out), leading to an expression for the constrained likelihood of

$$L\left(\text{data}\,|\,p_i^0\right) = N \int d\alpha_i \ \delta\left(m_Z - m_Z^0\right) L\left(\text{data}\,|\,p_i\,;\,\alpha_i\right) , \qquad (2.16)$$

where N is a normalization constant and p_i^0 are values for which the constraint yields the experimentally measured value. After simplifying,

$$L\left(\text{data}\,|\,p_i^0\right) = \left. \frac{1}{\Delta(p_i)} \ L\left(\text{data}\,|\,p_i\right) \right|_{p_i=p_i^0} \qquad (2.17a)$$

where

$$\Delta(p_i) \equiv \left| \frac{\partial\left(\ln m_Z^2\right)}{\partial\left(\ln p_i\right)} \right| . \qquad (2.17b)$$

Here, m_Z can be evaluated at the GUT scale, resulting in eq. (2.8) and Δ_{BG}, or evaluated at the weak scale, resulting in eq. (2.6b) and Δ_{EW}. Similarly, one can use the constraint of the Higgs mass instead, leading to Δ_{HS}.

Wilk's theorem[32, 33] can be used to relate the likelihood to a χ^2 as

$$\chi^2 = -2 \ln L \ . \tag{2.18}$$

From eq. (2.17a) and eq. (2.18), the constrained and unconstrained likelihoods, χ^2_{new} and χ^2_{old} respectively, and are related by

$$\chi^2_{\text{new}} \left(p_i^0 \right) = \left[\chi^2_{\text{old}} \left(p_i \right) + 2 \ln \Delta(p_i) \right] \Big|_{m_Z = m_Z^0} \ . \tag{2.19}$$

Trying to maintain a good fit requires $\chi^2/\text{d.o.f}$ to be near 1. This result clearly shows the additional cost of goodness of fit for fine-tuning. Although the choice for a maximum Δ is said to be vague, it is only as vague as an acceptable value for a χ^2 goodness of fit, therefore neglecting fine-tuning entirely is not permissible.

Chapter 3

Parameter Space

In this chapter, several SUSY models will be scrutinized computationally to determine what the limit of naturalness implies on model parameters and mass limits. Model independent bounds will be generated in section 3.2. Several GUT models will be considered under NUHM2 in section 3.3. In section 3.4, further GUT archetypes will be considered: NUHM2+D, $SU(5)$, and SUGRA12. The commonality between these models is radiatively-driven naturalness. Lastly, an archetype that does not include unification at the GUT scale, generalized mirage mediation (GMM) will be analyzed in section 3.5.

3.1 Radiatively-driven natural supersymmetry

Generally, it is difficult to randomly select input values, chosen at the GUT scale, which will result in a model with low fine-tuning. It is not clear which particular values of a parameter will allow the running of all masses and couplings through the RGEs to arrive at low Δ_{EW} contributions at the weak scale. Of particular difficulty are $m_{\tilde{t}_{1,2}}$, μ, and m_{H_u}, which can be remedied by the following:

- $m_{\tilde{t}_{1,2}}$: An exact choice of the weak scale, Q, has flexibility. Choosing $Q^2 = m_{\tilde{t}_1} m_{\tilde{t}_2}$ minimizes the logarithmic contribution to $\sum_u^u$, reducing the fine-tuning on the third generation squarks.

- μ and m_{H_u} : Instead of taking GUT scale values for $m_{H_{u,d}}$, values of $\mu(Q)$ and $m_A(Q)$ at $Q = m_{\text{weak}}$ may be used as inputs. Doing so enforces natural

values at the weak scale. The RGEs are used to find the corresponding GUT
scale $m_{H_{u,d}}$.

Without specifying the weak scale values of μ and m_A, μ is the necessary value
to enforce the measured value of m_Z and m_A is determined through the RGEs.
The value of m_{H_u} will vary dramatically with the scale as shown in fig. 3.1. If
the GUT value of m_{H_u} is too large, as seen in fig. 3.1(a), the running may not
be sufficient to drive m_{H_u} negative at a lower energy scale, which is necessary for
electro-weak symmetry breaking (EWSB). If the value for m_{H_u} is too low, EWSB
will occur at a higher scale and m_{H_u} will continue running negative. Although
EWSB still occurs, such a large negative value for m_{H_u} will lead to large fine-
tuning in μ to enforce m_Z. From section 2.3, the weak scale values of both μ and
m_{H_u} must be comparable in magnitude to m_Z. Choosing weak scale values of μ
and m_A determines appropriate GUT scale values such that the running of m_{H_u}
will be to small, not large, negative values[34]. This is deemed radiatively-driven
natural supersymmetry (RNS), first introduced by Ferrara et al.[35]. Furthermore,
as m_{H_u} approaches 0, the rate of change becomes large, increasing the difficulty
of keeping m_{H_u} as a small negative value. The choice of Q to be dependent on the
third generation squark masses allows more flexibility than choosing a constant
value. If the choice of Q was the same for $m_0 = 3$ TeV and 6 TeV in fig. 3.1(b),
either there would be no EWSB (black) or $\Delta_{EW} \geq 240$ (blue). RNS models allow
a broad range of parameter space while satisfying the naturalness conditions.
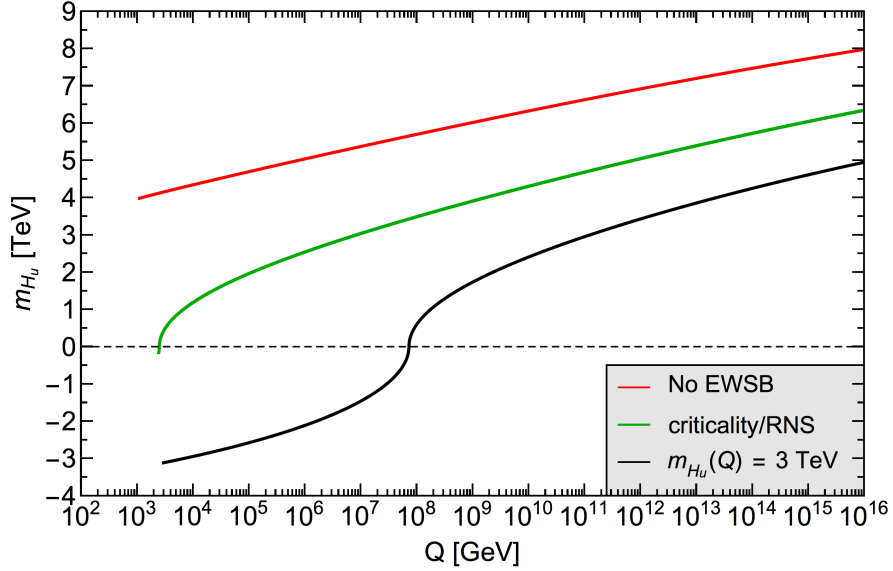
(a) Running of m_{H_u} from the GUT scale down to 1 TeV. The red line does not break electro-weak symmetry, the green line is for radiatively-driven natural SUSY, and the black line breaks electro-weak symmetry and leads to a large m_{H_u} value of 3 TeV.
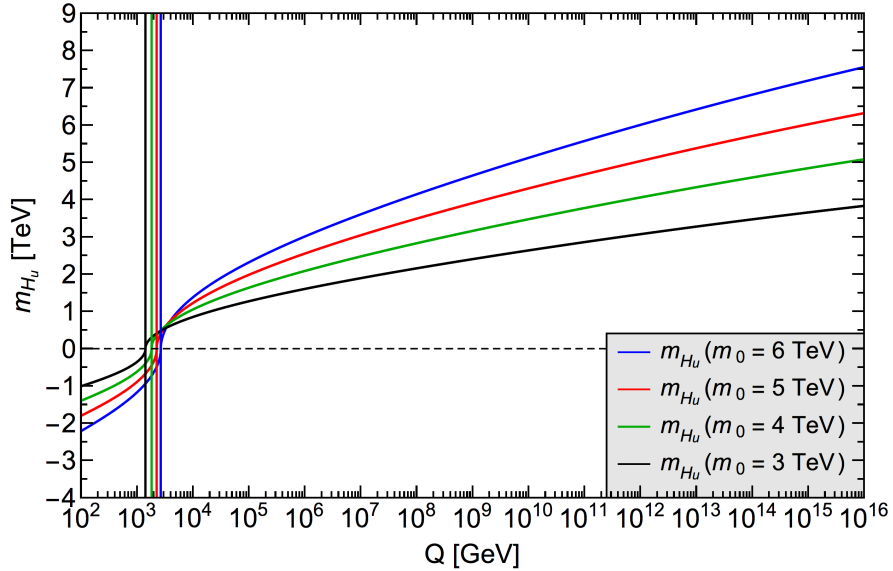
(b) Running of m_{H_u} for values of m_0 of 3 TeV (black), 4 TeV (red), 5 TeV (green), and 6 TeV (blue). Vertical lines denote $Q^2 = m_{\tilde{t}_1} m_{\tilde{t}_2}$.

Figure 3.1: Running of m_{H_u} for different values of $m_{H_u}(\text{GUT})$ (a) and m_0 (b).

3.2 Archetype independent bounds

The amount of fine-tuning comes from the largest contribution to m_Z in eq. (1.46a), where the Σs are denoted in table 1.5. The contribution from Σ_d^d to Δ_{EW} is suppressed by a factor of $\tan^2 \beta - 1$, whereas the contribution from Σ_u^u is enhanced by $\tan^2 \beta / (\tan^2 \beta - 1) \approx 1$. Therefore, for moderate to large $\tan \beta$, the Σ_d^d contributions can be ignored. Recall that the top squark contribution is

$$\Sigma_u^u \left(\tilde{t}_{1,2} \right) = \frac{3}{16\pi^2} \, F\!\left(m_{\tilde{t}_{1,2}}^2 \right) \left(f_t^2 - g_Z^2 \mp \frac{f_t^2 A_t^2 - 8g_Z^2 \left(\frac{1}{4} - \frac{2}{3} x_w \right) \Delta_t}{m_{\tilde{t}_2}^2 - m_{\tilde{t}_1}^2} \right), \qquad (3.1a)$$

$$F\!\left(m_{\tilde{t}_{1,2}}^2 \right) \equiv m_{\tilde{t}_{1,2}}^2 \left(\ln\!\left(\frac{m_{\tilde{t}_{1,2}}^2}{Q^2} \right) - 1 \right), \qquad (3.1b)$$

$$\Delta_t = \frac{1}{2} \left(m_{\tilde{t}_L}^2 - m_{\tilde{t}_R}^2 \right) + m_Z^2 \cos(2\beta) \left(\frac{1}{4} - \frac{2}{3} x_w \right), \text{ and} \qquad (3.1c)$$

$$m_{\tilde{t}_{1,2}}^2 = \frac{1}{2} \left(m_{\tilde{t}_L}^2 + m_{\tilde{t}_R}^2 \right) + \frac{1}{4} m_Z^2 \cos(2\beta) + m_t^2$$

$$\mp \sqrt{ \left(\frac{1}{2} \left(m_{\tilde{t}_L}^2 - m_{\tilde{t}_R}^2 \right) + m_Z^2 \cos(2\beta) \left(\frac{1}{4} - \frac{2}{3} x_w \right) \right)^2 + m_t^2 \left(\mu \cot \beta - A_t \right)^2 }.$$

$$(3.1d)$$

Taking typical values of $m_{\tilde{t}_L} = 2.6 \, m_{\tilde{t}_R}$, $\mu = 150$ GeV, and $f_t = 0.8365$, model independent bounds, determined by $m_{\tilde{t}_R}$ and A_t, are plotted for $\tilde{t}_1$ in fig. 3.2(a) and $\tilde{t}_2$ in fig. 3.2(b). The solid green line denotes the $\Delta_{EW} = 30$ cutoff. From $\tilde{t}_1$, there are asymptotes along the $m_{\tilde{t}_R} = \pm 0.43 \, A_t$ lines, allowing any range of parameters in a confined region. Furthermore, along the $A_t = 0$ TeV line, naturalness only continues to $m_{\tilde{t}_R} \approx 2.5$ TeV. On the other hand, the $\tilde{t}_2$ contri-

bution has different asymptote lines with shallower slopes and more naturalness along the $A_t = 0$ TeV line. Putting the two together, shown in fig. 3.2(c), taking $\sum_u^u \left(\tilde{t}_1, \tilde{t}_2 \right) \equiv \max \left(\sum_u^u \left(\tilde{t}_1 \right), \sum_u^u \left(\tilde{t}_2 \right) \right)$, all asymptotes are truncated, resulting in a finite range of parameters. In addition to just this naturalness plane, other constraints must be held, e.g. the Higgs mass. For $A_t \approx 0$, it is difficult, if not impossible, to generate $m_h = 125$ GeV. To do so requires larger $m_{\tilde{t}}$; however, there is not sufficient natural space to accomplish this. To circumvent the Higgs mass issue, larger A_t must be taken.

A different choice of μ or $\tan \beta$ has negligible effect on $\sum_u^u \left(\tilde{t} \right)$. Varying the relationship between $m_{\tilde{t}_L}$ and $m_{\tilde{t}_R}$ narrows(widens) the angle between the asymptotes for decreasing(increasing) values of $m_{\tilde{t}_L}/m_{\tilde{t}_R}$.

Similar results are shown for $\tilde{b}$ in the $m_{\tilde{b}_R} - \mu$ plane in fig. 3.3 with $m_{\tilde{b}_L} = 0.72 \, m_{\tilde{b}_R}$ and $f_b = 0.13$, $A_b = -8$ TeV, allowing μ to vary, and introducing $Q = 2168$ GeV. h, H, and $H^{\pm}$ are shown in the $\tan \beta - m_A$ plane in fig. 3.4, allowing $\tan \beta$ to vary. $\widetilde{W}$ is shown in the $M_2 - \mu$ plane in fig. 3.5, allowing μ to vary. Lastly, $\widetilde{Z}$ is shown in the $M_2 - M_1$ plane in fig. 3.6.
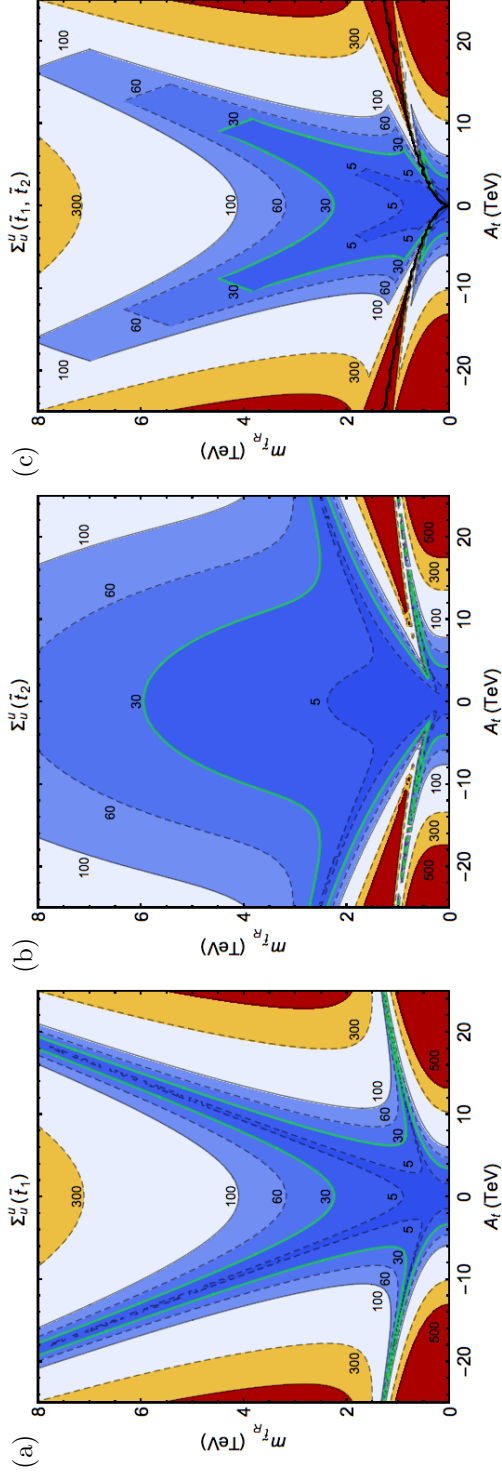
Figure 3.2: $\sum_u^u$ contributions to Δ_{EW} from $\tilde{t}_1$, $\tilde{t}_2$, and $\max(\tilde{t}_1, \tilde{t}_2)$ in (a), (b), and (c) respectively with $m_{\tilde{t}_L} = 2.6 \, m_{\tilde{t}_R}$.
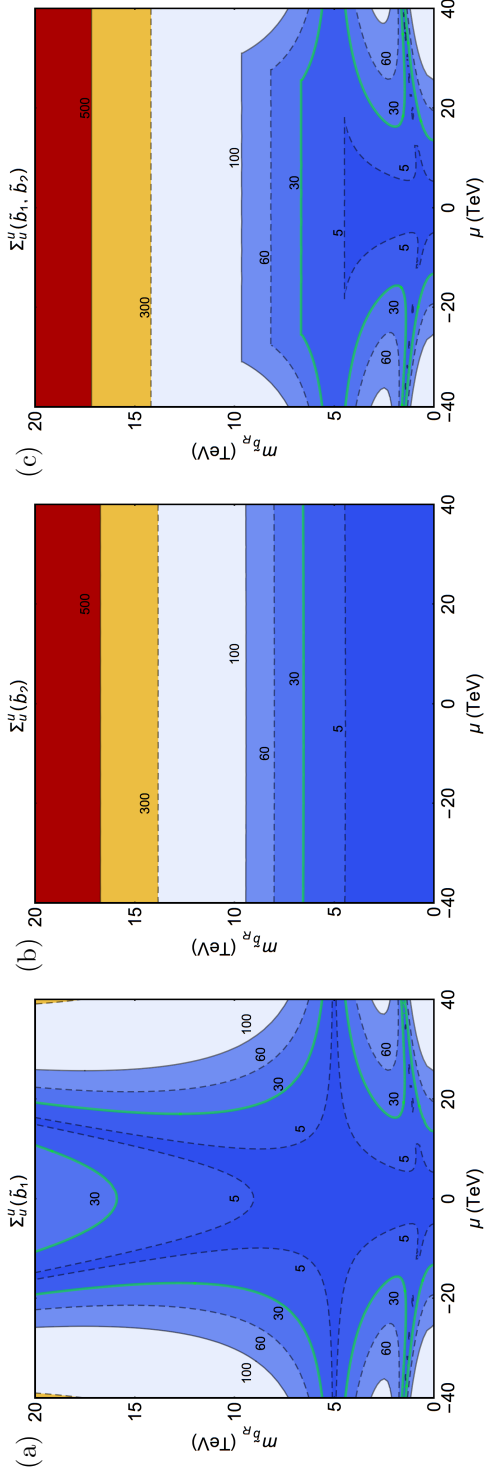
Figure 3.3: $\sum_u^u$ contributions to Δ_{EW} from $\tilde{b}_1$, $\tilde{b}_2$, and $\max(\tilde{b}_1, \tilde{b}_2)$ in (a), (b), and (c) respectively with $m_{\tilde{t}_L} = 2.6 \, m_{\tilde{t}_R}$.
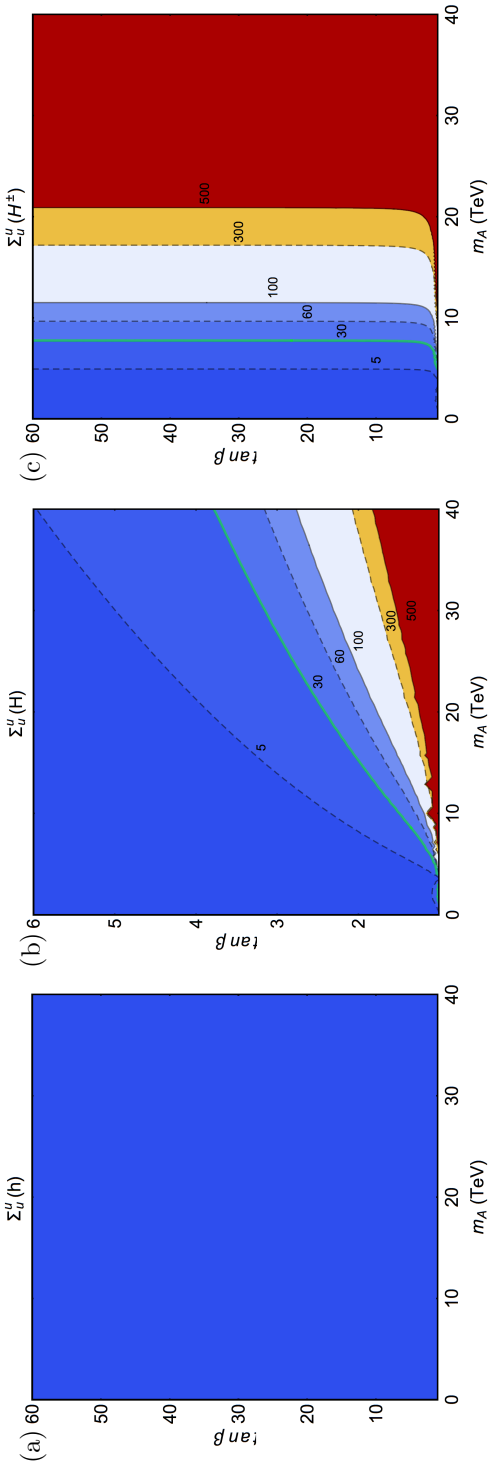
Figure 3.4: $\sum_u^u$ contributions to Δ_{EW} from h, H, and $H^{\pm}$ in (a), (b), and (c) respectively, the largest coming from $H^{\pm}$.
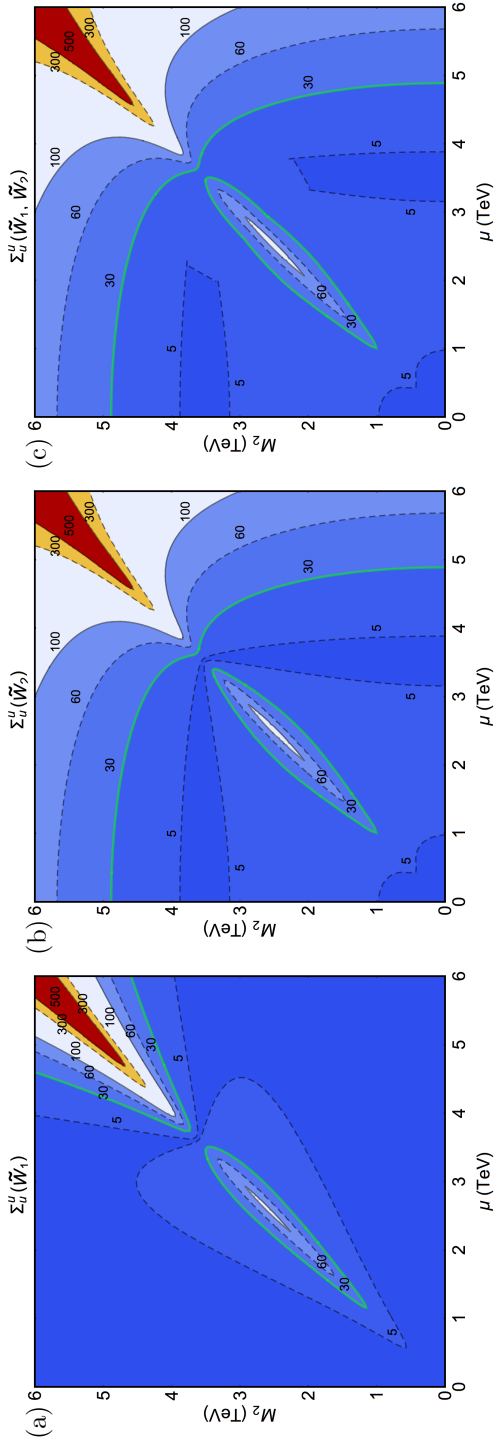
Figure 3.5: $\sum_u^u$ contributions to Δ_{EW} from $\widetilde{W}_1$, $\widetilde{W}_2$, and $\max(\widetilde{W}_1, \widetilde{W}_2)$ in (a), (b), and (c) respectively.

43
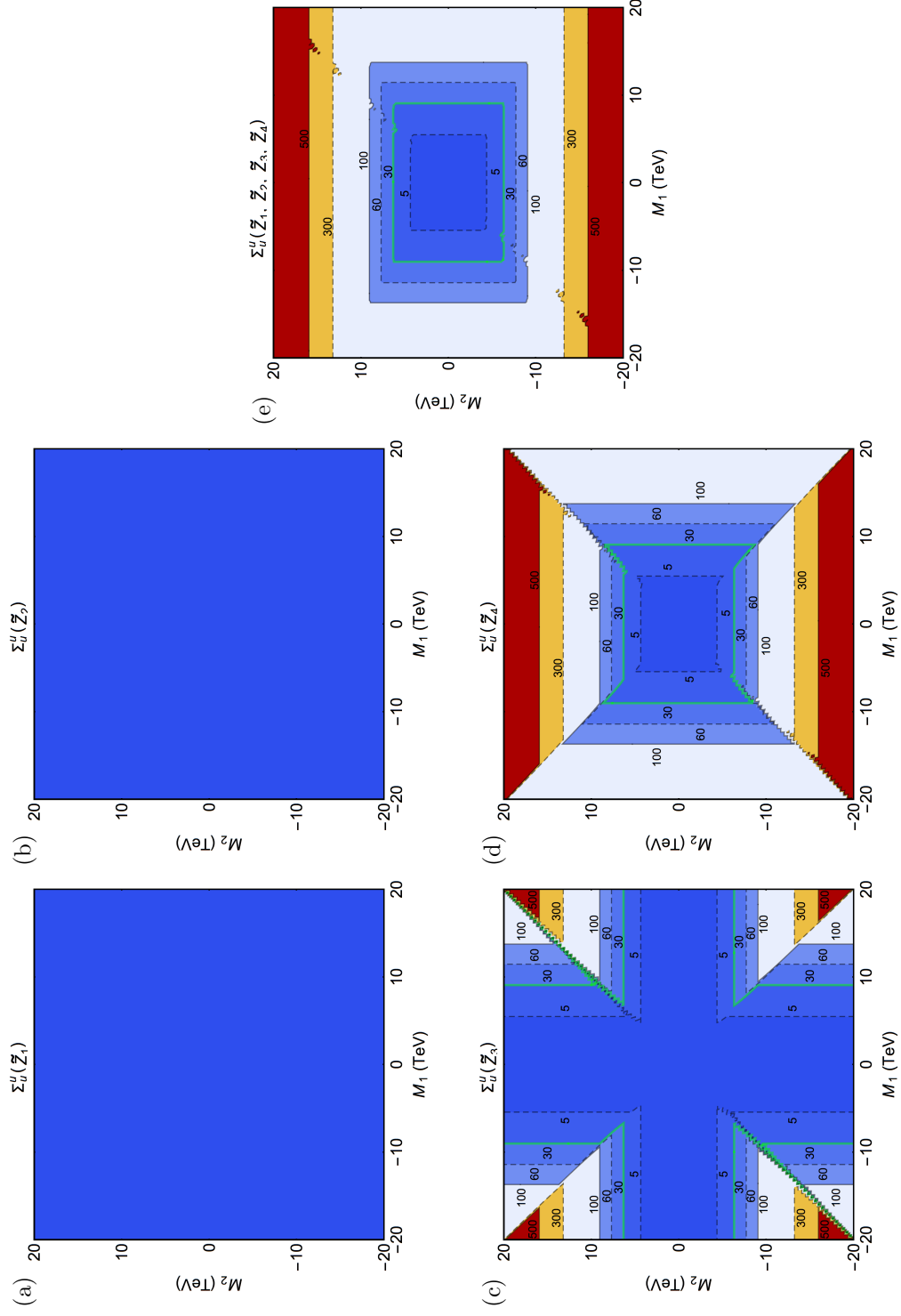
Figure 3.6: $\sum_u^u$ contributions to Δ_{EW} from $\widetilde{Z}_1$, $\widetilde{Z}_2$, $\widetilde{Z}_3$, $\widetilde{Z}_4$, and $\max(\widetilde{Z}_1, \widetilde{Z}_2, \widetilde{Z}_3, \widetilde{Z}_4)$ in (a), (b), (c), (d), and (e) respectively.

Naturalness in $\tilde{b}$ also limits the asymptotes extending in $m_{\tilde{b}_R}$ from the $\tilde{b}_2$ contribution. In the Higgs sector, h is completely unrestricted in the region shown, whereas $H^\pm$ determines the natural range of m_A. $\widetilde{W}$ contributions are fairly unrestricted, though there is an interesting region of high fine-tuning along the $M_2 \approx \mu$ line where the mass gap between $m_{\widetilde{W}_2} - m_{\widetilde{W}_1}$ becomes small, leading to large fine-tuning in both $\widetilde{W}_1$ and $\widetilde{W}_2$. $\widetilde{Z}_{1,2}$ are Higgsino like, and thus their contributions are unconstrained in the region shown. The $\widetilde{Z}_3$ contribution is constrained in regions of simultaneously high M_2 and M_1, more(less) so where $\widetilde{Z}_3$ is bino(wino)-like, i.e. $|M_1| > |M_2|$ ($|M_2| > |M_1|$). The $\widetilde{Z}_4$ contribution is constrained in both M_2 and M_1, more so when $\widetilde{Z}_4$ is wino-like. The total neutralino constraint comes from $\widetilde{Z}_4$, except for when $\widetilde{Z}_3$ is heavy and bino-like.

Although these limits apply in general, selecting a particular SUSY model will further restrict the allowed ranges. The comparison between different model archetypes is the subject of sections 3.3 to 3.5.

3.3   NUHM2

In this section, an archetype of models, deemed two extra parameter non-universal Higgs models (NUHM2), will be presented and analyzed. In NUHM2 models, H_u and H_d reside in different $SO(10)$ irreducible representations, leading to independent mass values. As mentioned in section 3.1, these will be traded out for $\mu(Q)$ and $m_A(Q)$. Putting the matter superfields in a 16-dimensional representation unifies the masses to $m_{16} \equiv m_0$. Furthermore, gaugino unification is assumed; $M_1 = M_2 = M_3 \equiv m_{1/2}$. Also, the t Yukawa coupling may be taken as different than the unified b and τ Yukawa couplings. The parameter space is

determined by the inputs:

$$m_0, \; m_{1/2}, \; A_0, \; \tan\beta, \; \mu, \; m_A. \tag{3.2}$$

Three sample points are shown in table 3.1 with the input values and their associated sparticle mass spectra. Model 1 is quite natural with stop and gluino masses beyond the current exclusion limits set by the Large Hadron Collider (LHC). Model 2 is highly natural, but is currently ruled out by LHC and also does not provide a heavy enough Higgs mass to be valid. Model 3 is beyond LHC detection; however, is very unnatural with $\Delta_{EW} = 109$. The SUSY models of interest are the ones similar to model 1, where all of the parameters are beyond current experimental limits, while maintaining low fine-tuning, $\Delta_{EW} \leq 30$.

To search for these natural models beyond current experimental limits, the NUHM2 parameter space is scanned numerically using the Isajet/Isasugra spectrum generator[36], sampling values within the ranges:

$$0.2 \text{ TeV} \leq m_0 \leq 20 \text{ TeV},$$
$$0.3 \text{ TeV} \leq m_{1/2} \leq 3 \text{ TeV},$$
$$-3 \leq A_0/m_0 \leq 3,$$
$$3 \leq \tan\beta \leq 60,$$
$$0.1 \text{ TeV} \leq \mu \leq 1.5 \text{ TeV},$$
$$0.15 \text{ TeV} \leq m_A \leq 20 \text{ TeV}. \tag{3.3}$$

Each set of input values will produce an individual model under the NUHM2 archetype with its own mass spectrum. For each model to be phenomenologically valid, it must satisfy the following conditions:

46

Parameter	Model 1	Model 2	Model 3
m_0	4000	2000	7000
$m_{1/2}$	900	400	1100
A_0	-6400	3200	-7000
$\tan\beta$	10	30	15
μ	150	175	160
m_A	1000	1000	1700
$m_{\tilde{g}}$	2180	1020	2710
$m_{\tilde{t}_1}$	1290	1030	3750
$m_{\tilde{t}_2}$	3080	1560	5630
$m_{\tilde{b}_1}$	3100	1550	5620
$m_{\tilde{b}_2}$	4190	1930	7040
$m_{\tilde{\tau}_1}$	3780	1700	6660
$m_{\tilde{\tau}_2}$	4090	1900	7050
$m_{\tilde{\nu}_\tau}$	4090	1910	7060
$m_{\widetilde{Z}_1}$	144	135	158
$m_{\widetilde{Z}_2}$	158	187	169
$m_{\widetilde{Z}_3}$	403	192	498
$m_{\widetilde{Z}_4}$	776	351	960
$m_{\widetilde{W}_1^\pm}$	156	168	170
$m_{\widetilde{W}_2^\pm}$	766	344	940
m_h	124.0	115.4	123.6
m_H	1010	1010	1710
m_A	1000	1000	1700
$m_{H^\pm}$	1000	1000	1700
$\Omega_{\widetilde{Z}_1}h^2$	0.0078	0.029	0.0080
$BF(b \to s\gamma) \times 10^4$	3.26	3.33	3.19
$BF(B_s \to \mu^+\mu^-) \times 10^9$	3.85	3.70	3.84
Δ_{EW}	10.5	7.37	109

Table 3.1: Sparticle mass spectra from three NUHM2 points along with their input values and fine-tuning Δ_{EW}. All masses, A_0, and μ are in GeV.

- electro-weak symmetry is radiatively broken (REWSB),

- the lightest SUSY particle is the neutralino, $\widetilde{Z}_1$,

- the model independent LEP2 limit is respected ($m_{\widetilde{W}_1} > 103.5$ GeV[37]),

- LHC8 limits on $m_{\tilde{q}}$ and $m_{\tilde{g}}$ from the $m_{1/2}$ vs m_0 plane[38] are respected,

- the Higgs mass falls within $m_h = (125 \pm 2)$ GeV, allowing for 2 GeV uncertainty in the theoretical calculation, and

- $m_{\tilde{g}} > 1.3$ TeV.

Each model that satisfies these conditions has a unique set of inputs, resulting in unique: mass spectrum at both GUT and Q scales, fine-tuning, decay widths, etc. These data are saved and plotted in the following as an individual data point for each model. To well establish how fine-tuning depends on each input parameter, Δ_{EW} is plotted against m_0 in fig. 3.7(a), $m_{1/2}$ in fig. 3.7(b), A_0 in fig. 3.7(c), μ(full) in fig. 3.7(d), μ(natural) in fig. 3.8(a), and m_A in fig. 3.8(b)[39]. The points are color-coded for $\tan\beta > 30$ (red), $15 < \tan\beta \leq 30$ (blue), and $\tan\beta \leq 15$ (green).

The scan was done in three steps: full, focused, and extremum. The full and focused scans generated inputs from a uniform distribution. The full scan sampled over the entire range of the inputs, whereas the focused scan was over a narrowed range of parameter space, where natural models can be generated. Finally, the extremum scan is an optimization algorithm written to search for inputs yielding locally minimum values of Δ_{EW}. The extremum scan finds a valid and natural starting model, from which it produces the next, more natural, model based off small variations from the previous input values. This process repeats until a sufficient number of iterations or convergence on a local minimum has been achieved and is consequently not a uniform sampling of the parameter space.
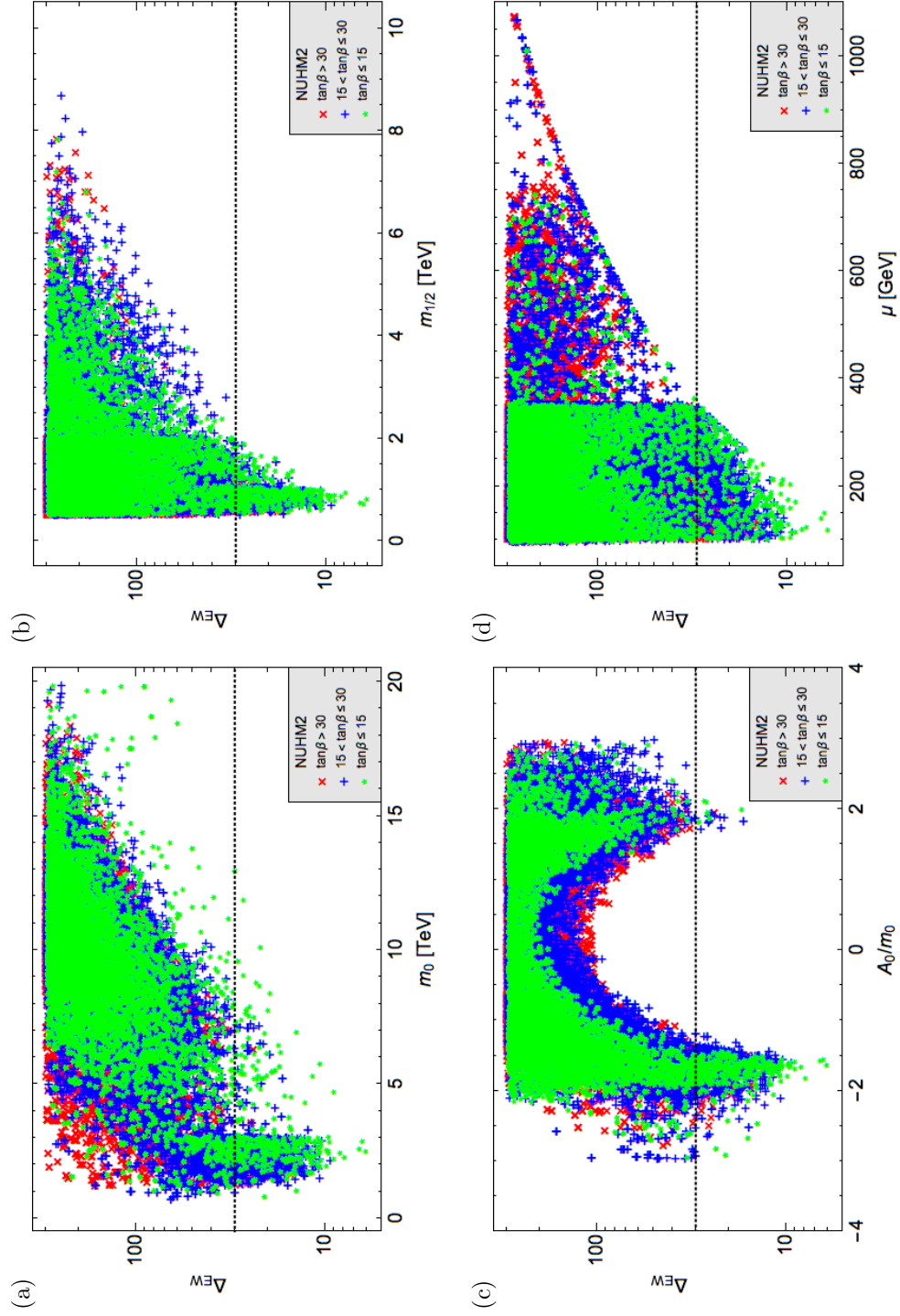
Figure 3.7: Plots of Δ_{EW} vs. m_0, $m_{1/2}$, A_0/m_0, and μ in (a), (b), (c), and (d) respectively. Models are separated by $\tan\beta$ into low ($\tan\beta \leq 15$), mid ($15 < \tan\beta \leq 30$) and high ($30 < \tan\beta \leq 60$) regions.
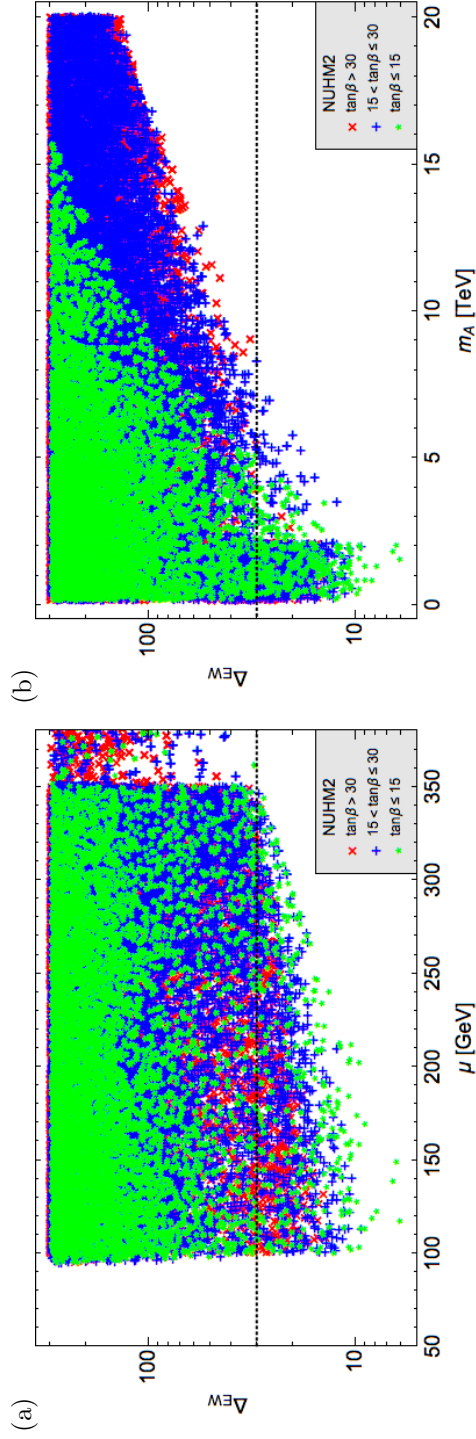
Figure 3.8: Plots of Δ_{EW} vs. μ (restricted region) and m_A (a) and (b) respectively. Models are separated by $\tan\beta$ into low ($\tan\beta \leq 15$), mid ($15 < \tan\beta \leq 30$) and high ($30 < \tan\beta \leq 60$) regions.

Natural limits on the NUHM2 archetype input parameters can be extracted:

- $m_0 \lesssim 13$ TeV,

- $m_{1/2} \lesssim 2$ TeV,

- $-3 \lesssim A_0/m_0 \lesssim -1$ or $1.4 \lesssim A_0/m_0 \lesssim 2.4$,

- $\mu \lesssim 350$ GeV,

- $m_A \lesssim 9$ TeV.

The ranges for the outputs of the masses, at scale Q, can be examined similarly. Of particular interest are m_h, plotted in fig. 3.9(a), and the masses of the searched for $\widetilde{W}_1$, $\tilde{g}$, and $\tilde{t}_1$ which are plotted in fig. 3.15(a), 3.13(a), and 3.14(a) respectively. The vertical lines denote the current experimental search limits of $m_{\widetilde{W}_1} > 103.5$ GeV, $\tilde{g} > 2.1$ TeV, and $m_{\tilde{t}_1} > 0.95$ TeV. Results from the outputs in fig. 3.9 are:

- $m_{\widetilde{W}_1} \lesssim 350$ GeV,

- $m_{\tilde{g}} \lesssim 4.5$ TeV, and

- $m_{\tilde{t}_1} \lesssim 3$ TeV.

Similarly for other masses[40], not shown here:

- $m_{\widetilde{Z}_1}, m_{\widetilde{Z}_2} \lesssim 350$ GeV,

- $m_{\widetilde{Z}_3}, M_1 \lesssim 900$ GeV,

- $m_{\widetilde{Z}_4}, m_{\widetilde{W}_2}, M_2 \lesssim 1600$ GeV,

- $m_{\tilde{t}_2}, m_{\tilde{b}_1} \lesssim 9$ TeV,

- $m_{\tilde{\tau}_1} \lesssim 12$ TeV, and

- $m_{\text{gen 1}}, m_{\text{gen 2}}, m_{\tilde{b}_2}, m_{\tilde{\tau}_2} \lesssim 13$ TeV.
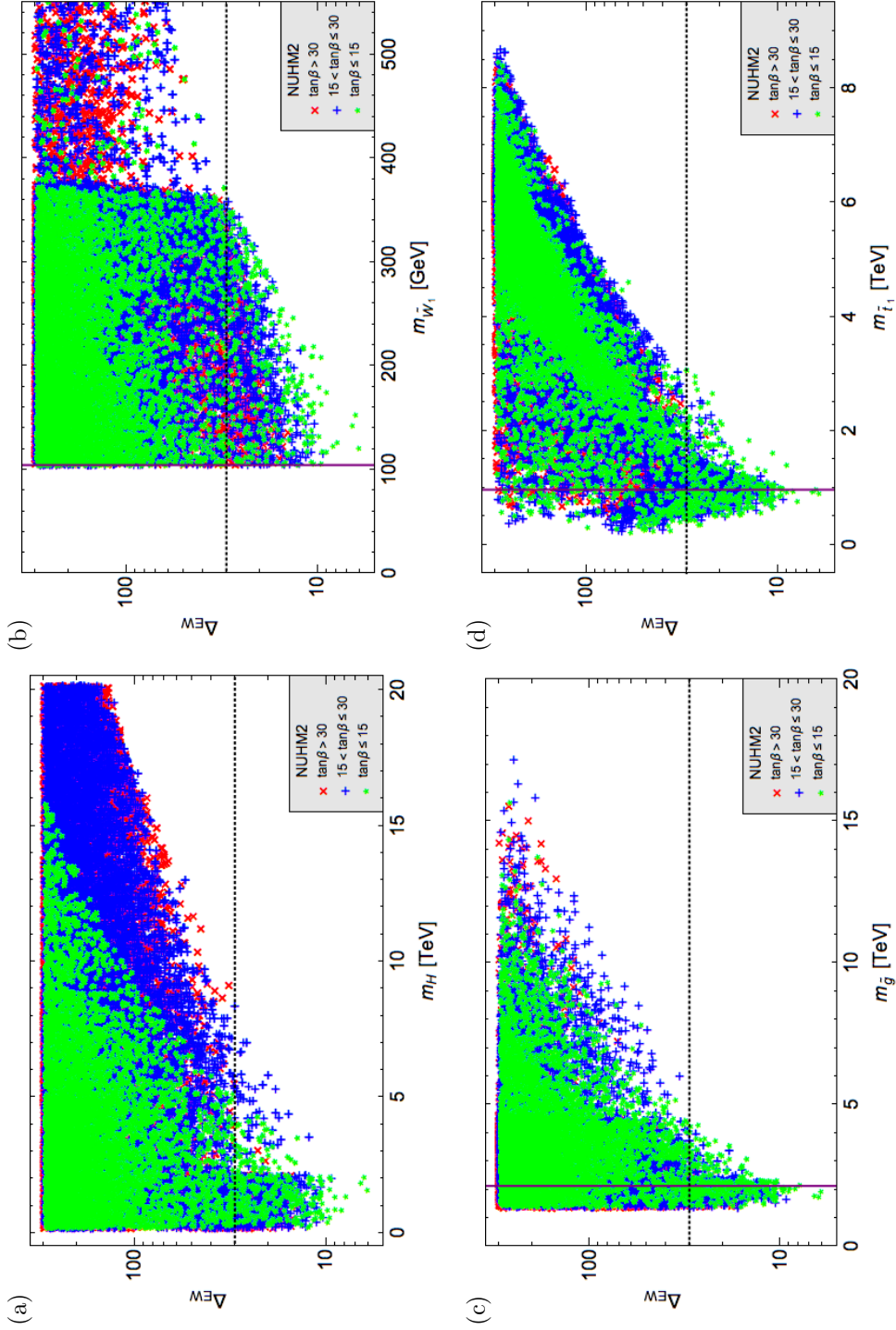
Figure 3.9: Plots of Δ_{EW} vs. m_h, $m_{\widetilde{W}_1}$, $m_{\tilde{g}}$, and $m_{\tilde{t}_1}$ in (a), (b), (c), and (d) respectively. Models are separated by $\tan\beta$ into low ($\tan\beta \leq 15$), mid ($15 < \tan\beta \leq 30$) and high ($30 < \tan\beta \leq 60$) regions. The vertical line displays the current experimental limits of $m_{\widetilde{W}_1} > 103.5$ GeV, $m_{\tilde{g}} > 2.1$ TeV, and $m_{\tilde{t}_1} > 0.95$ TeV.

mass bound	Δ_{BG} [GeV]	here [GeV]
μ	350	350
$m_{\tilde{g}}$	350	4000
M_1	90	900
M_2	170	1600
$m_{\tilde{u}_R}$	700	13000
$m_{\tilde{e}_R}$	520	13000

Table 3.2: Comparison of upper bounds on NUHM2 outputs found by Barbieri and Giudice and using Δ_{EW} with the consistent cutoff of $\Delta \leq 30$.

These results can be compared to those determined by Barbieri and Giudice, as shown in table 3.2. Truly, if the results of Barbieri and Giudice were the full story, then SUSY would indeed be in a crisis! Fortunately, implementing the conservative $\Delta_{EW} \leq 30$ on NUHM2, the bounds increase greatly. The $m_{1/2} - m_0$ plane is shown in fig. 3.10 with contours for $\Delta_{EW} = \{15, 30, 50, 75\}$ in black, $m_{\tilde{g}} = \{1, 2, 3, 4\}$ TeV in green, $m_{\tilde{t}_1} = \{1, 2, 3\}$ TeV in blue, and $m_h = \{123, 127\}$ GeV in red.

The search limits in the $m_0 - m_{1/2}$ plane from the ATLAS collaboration at $\sqrt{s} = 8$ TeV with $L = 20$ fb^{-1} integrated luminosity are shown in fig. 3.11[41]. The limit on $m_{1/2}$ extends to only ≈ 500 GeV (≈ 800 GeV for lower m_0), which is only about 1/4 of the parameter space in $m_{1/2}$. Furthermore, in m_0, only about half of the parameter space is being explored. While the most natural models ($\Delta_{EW} \lesssim 10$) are being explored, there is a significant amount of natural parameter space untouched. For $\sqrt{s} = 13$ TeV with $L = 36.1$ fb^{-1}, $\tilde{t}_1$ is shown in fig. 3.12(a)[42], where only 1/3 of the space is searched and less than half for $\tilde{g}$, shown in fig. 3.12(b)[43]. The LHC is ever running, currently taking data at $\sqrt{s} = 13$ TeV and is projected to gather 3000 fb^{-1} integrated luminosity by 2030. Plans for post high luminosity LHC (HL-LHC) include using the existing tunnel
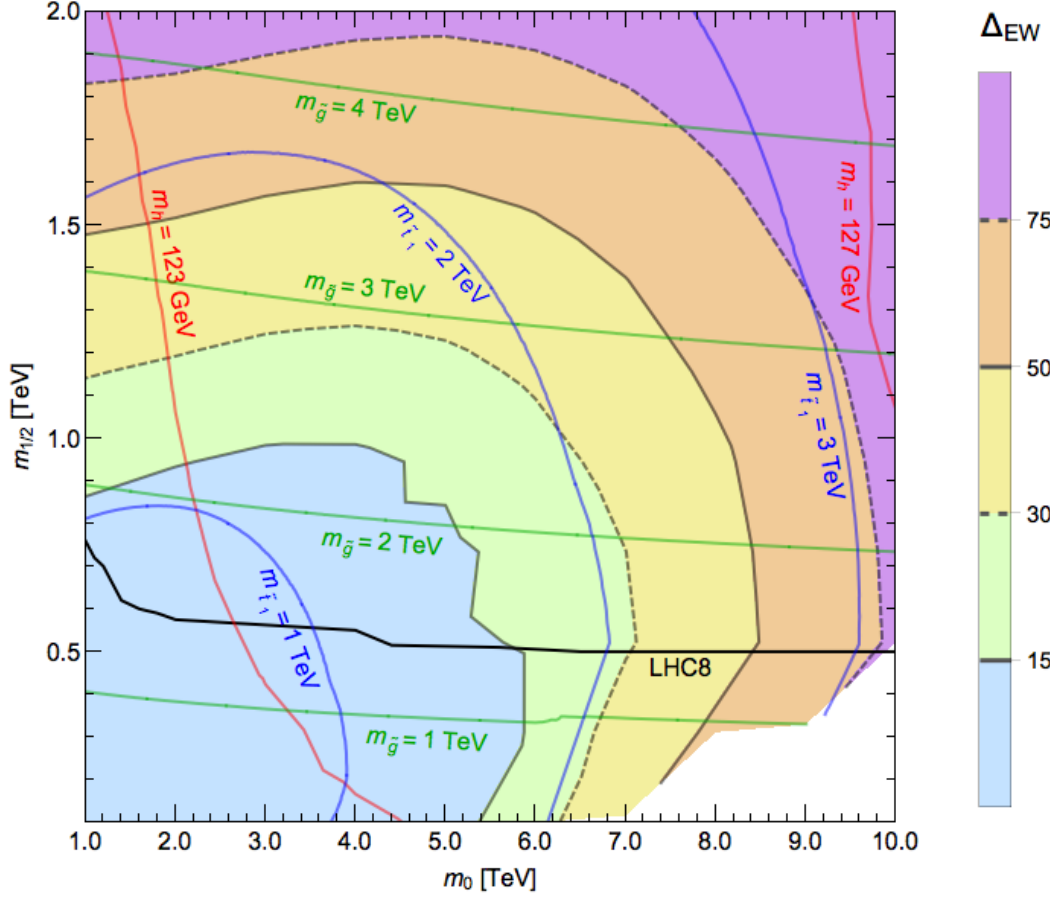
Figure 3.10: Contour plot of Δ_{EW} in the $m_{1/2} - m_0$ plane for NUHM2 with $A_0 = -1.66m_0$, $\tan\beta = 10$, $\mu = 110$ GeV, and $m_A = 2.0$ TeV. Additional contours show $m_{\tilde{g}}$, $m_{\tilde{t}_1}$, and m_h in green, blue, and red respectively. The black line shows the ATLAS exclusion for $\sqrt{s} = 8$ TeV as shown in fig. 3.11. The white region in high m_0 and low $m_{1/2}$ has no EWSB.

and upgrading the strength of the magnets, which could push $\sqrt{s}$ up to 28 or 33 TeV, or alternatively, diggin a larger tunnel and upgrading the strength of the magnets to increase $\sqrt{s}$ up to 100 TeV. The projected range of observation at HL-LHC and possible upgrades, as well as the International Linear Collider (ILC), is the focus of chapter 4.
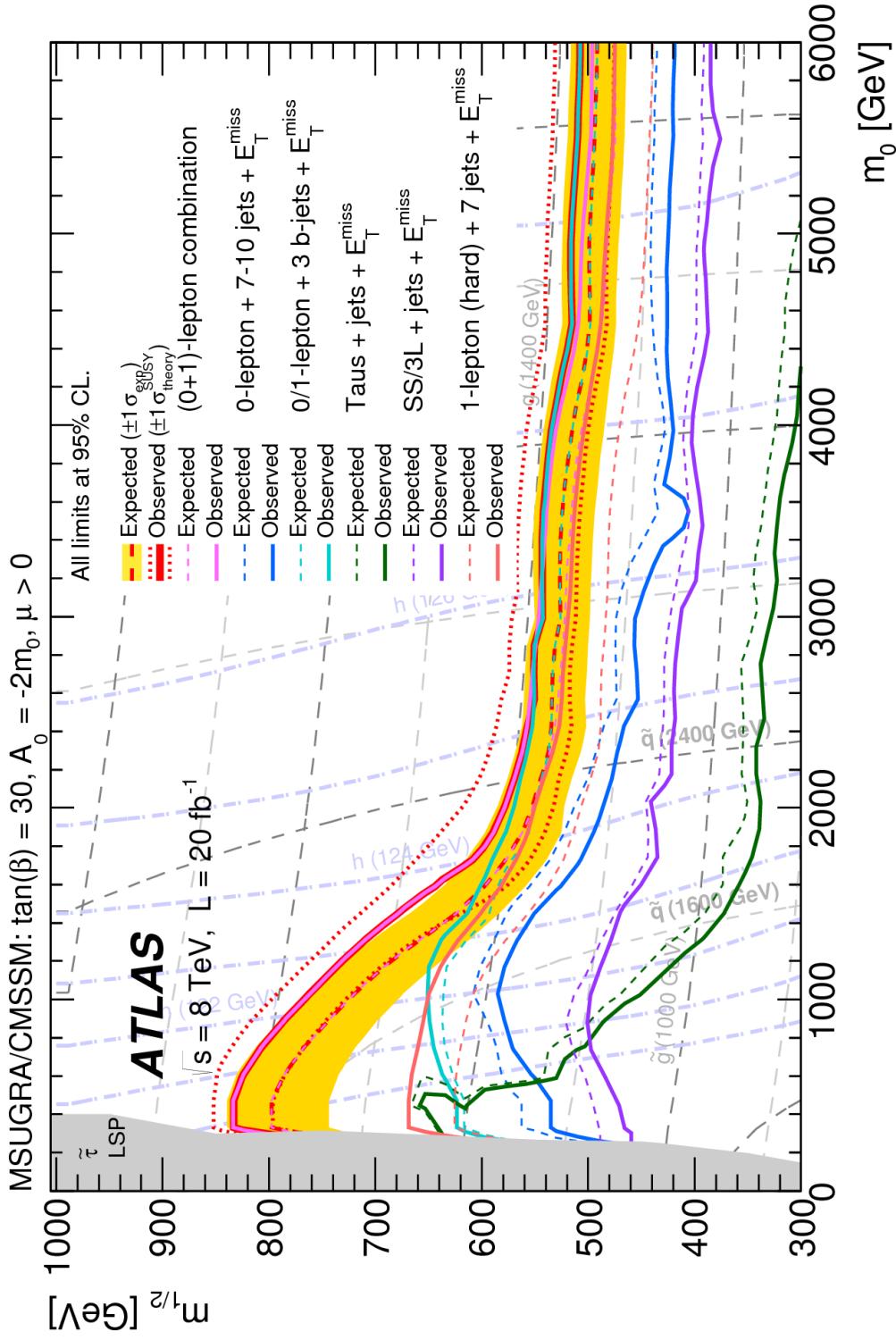
Figure 3.11: ATLAS inclusive searches for squarks and gluinos at $\sqrt{s} = 8$ TeV. 95% exclusion regions shown in the $m_0 - m_{1/2}$ plane.
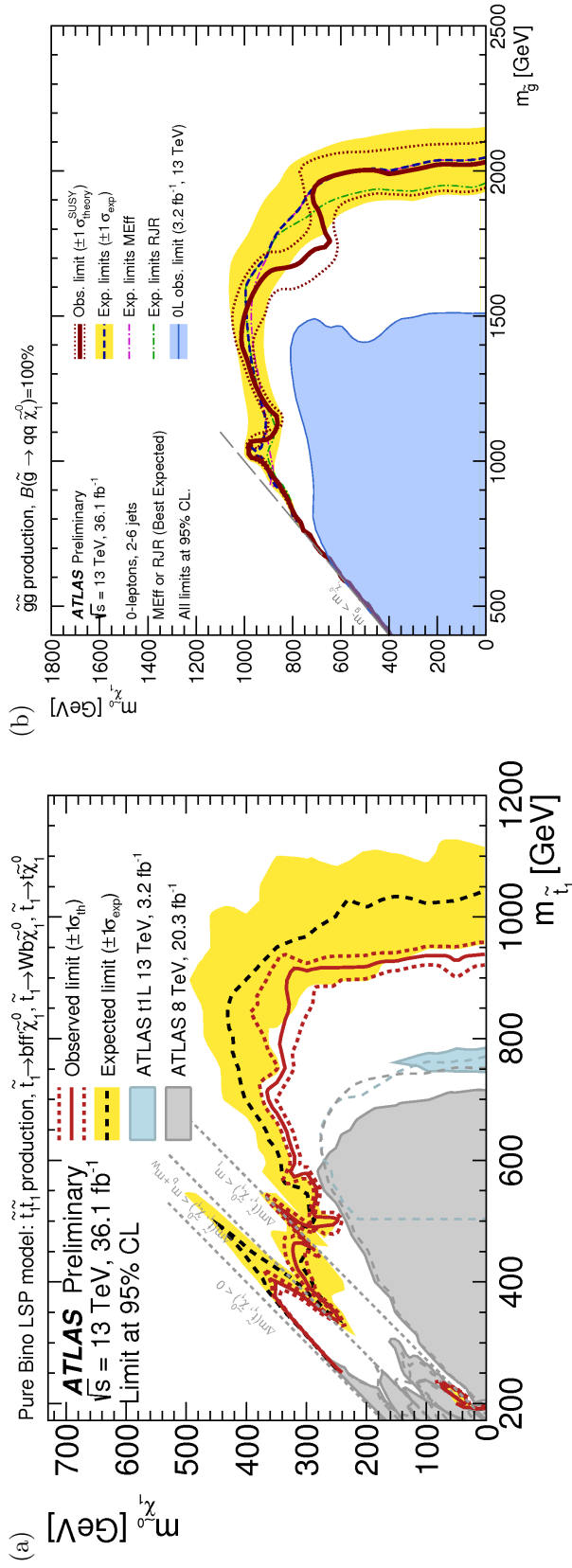
Figure 3.12: (a) ATLAS top squark pair production searches at both $\sqrt{s} = 8$ TeV with $L = 20.3$ fb^{-1} and $\sqrt{s} = 13$ TeV with $L = 36.1$ fb^{-1}. Expected and observed exclusion regions shown in the $m_{\tilde{t}_1} - m_{\tilde{\chi}_1^0}$ plane with assumed 100% BF for either $\tilde{t}_1 \to t\tilde{\chi}_1^0$, $\tilde{t}_1 \to W b \tilde{\chi}_1^0$, or $\tilde{t}_1 \to b f f' \tilde{\chi}_1^0$. (b) ATLAS gluino pair production search at $\sqrt{s} = 13$ TeV with $L = 36.1$ fb^{-1}. Expected and observed exclusion regions shown in the $m_{\tilde{g}} - m_{\tilde{\chi}_1^0}$ plane with decay of $\tilde{g} \to q \bar{q} \tilde{\chi}_1^0$.

56

3.4 NUHM2(+D), $SU(5)$, and SUGRA12

The previous section detailed the numerical analysis of NUHM2 models. This section will compare different GUT archetypes: NUHM2, NUHM2+D, $SU(5)$, and SUGRA12, defined below. Table 3.3 lists the inputs of each archetype and shows the imposed unifications while table 3.4 shows the ranges of the free parameters, defining each model, scanned numerically.

NUHM2+D assumes matter scalars are in a 16-dimensional irreducible representation, just as in NUHM2; however, the MSSM Higgs are elements of a single 10-dimensional representation of the Higgs ($\mathbf{10} = \mathbf{5} \oplus \mathbf{5^*}$). The breaking of $SO(10)$ yields a D-term, M_D^2, which gives rise to the GUT scale splitting between both the Higgs masses and the scalar masses. The relations are listed in table 3.3. Gauge bosons can also be assumed to unify at the GUT scale.

$SU(5)$ assumes L_i and D_i are in a $\mathbf{5^*}$ multiplet, while Q_i, U_i, and E_i are in a $\mathbf{10}$ multiplet, leading to masses m_5 and m_{10} respectively. H_u resides in a $\mathbf{5}$ irreducible Higgs representation while H_d lives in a $\mathbf{5^*}$ irreducible Higgs representation, allowing for non-unified Higgs boson masses. A color triplet Higgs accompanies each of H_u and H_d to fill out the $\mathbf{5}$ and $\mathbf{5^*}$ multiplets. The color triplets are assumed to stay heavy as the doublets become light, leading to the doublet-triplet splitting.

SUGRA12 is a more general archetype that simply assumes unification between all three generation squarks, providing a degeneracy solution to the SUSY flavor and CP problems. Gaugino mass unification is also assumed.

Archetype	Model Parameters
NUHM2	$m_0 \equiv m_{Q_i} = m_{U_i} = m_{D_i}$ $m_{Q_i} = m_{L_i} = m_{E_i}$ $m_{1/2} \equiv M_1 = M_2 = M_3$ $A_0 \equiv A_t = A_b = A_\tau$ $\tan\beta, \ \mu(Q), \ m_A(Q)$
NUHM2+D	$m_{16}^2 + M_D^2 \ = m_{Q_i}^2 = m_{E_i}^2 = m_{U_i}^2$ $m_{16}^2 - 3M_D^2 = m_{D_i}^2 = m_{L_i}^2$ $m_{10}^2 \mp 2M_D^2 = m_{H_{u,d}}^2$ $m_{16}^2 + 5M_D^2 = m_N^2$ $m_{1/2} \equiv M_1 = M_2 = M_3$ $\tan\beta, \ \text{sign}(\mu)$
$SU(5)$	$m_{10} \equiv m_{Q_i} = m_{U_i} = m_{E_i}$ $m_5 \equiv m_{L_i} = m_{D_i}$ $m_{1/2} \equiv M_1 = M_2 = M_3$ $A_b = A_\tau$ A_t $\tan\beta, \ \mu, \ m_A$
SUGRA12	$m_Q \equiv m_{Q_1} = m_{Q_2} = m_{Q_3}$ $m_U \equiv m_{U_1} = m_{U_2} = m_{U_3}$ $m_D \equiv m_{D_1} = m_{D_2} = m_{D_3}$ $m_L \equiv m_{L_1} = m_{L_2} = m_{L_3}$ $m_E \equiv m_{E_1} = m_{E_2} = m_{E_3}$ $m_{1/2} \equiv M_1 = M_2 = M_3$ $A_t, \ A_b, \ A_\tau$ $\tan\beta, \ \mu, \ m_A$

Table 3.3: List of the unifications of GUT archetypes: NUHM2, NUHM2+D, $SU(5)$, and SUGRA12.

For the NUHM2+D archetype, the usual trade of m_{H_u} and m_{H_d} can be made for μ and m_A. $m_{16} \equiv m_0$ to match the structure of NUHM2, both now having inputs of m_0, $m_{1/2}$, A_0, $\tan\beta$, μ, and m_A.

Similar to NUHM2, models from the four archetypes are plotted[44] with Δ_{EW} against $m_{\tilde{g}}$ in fig. 3.13, $m_{\tilde{t}_1}$ in fig. 3.14, and $m_{\widetilde{W}_1}$ in fig. 3.15. Results are enumerated in table 3.5. These can be compared to the current exclusion limits of $m_{\tilde{t}_1} > 950$ GeV and $m_{\tilde{g}} > 2.1$ TeV. Natural NUHM2 models can extend far beyond the current limits from LHC, but does that imply the LHC is insufficient for detecting natural SUSY? An in depth analysis of the expected reach of the LHC is the subject of chapter 4.

Archetype	Parameter	Scan Limits
NUHM2 (+D)	m_0	$[0.10, 20.]$ TeV
	$m_{1/2}$	$[0.20, 3.0]$ TeV
	A_0/m_0	$[-3, 3]$
	$\tan\beta$	$[3, 60]$
	$\mu(Q)$	$[0.15, 0.50]$ TeV
	$m_A(Q)$	$[0.15, 20.]$ TeV
$SU(5)$	m_{10}	$[0.10, 20.]$ TeV
	m_5	$[0.10, 20.]$ TeV
	$m_{1/2}$	$[0.20, 3.0]$ TeV
	$A_b = A_\tau$	$[-40, 40]$ TeV
	A_t	$[-40, 40]$ TeV
	$\tan\beta$	$[3, 60]$
	μ	$[0.15, 0.50]$ TeV
	m_A	$[0.15, 20.]$ TeV
SUGRA12	m_Q	$[0.10, 20.]$ TeV
	m_U	$[0.10, 20.]$ TeV
	m_D	$[0.10, 20.]$ TeV
	m_L	$[0.10, 20.]$ TeV
	m_E	$[0.10, 20.]$ TeV
	$m_{1/2}$	$[0.20, 3.0]$ TeV
	A_t	$[-40, 40]$ TeV
	A_b	$[-40, 40]$ TeV
	A_τ	$[-40, 40]$ TeV
	$\tan\beta$	$[3, 60]$
	μ	$[0.15, 0.50]$ TeV
	m_A	$[0.15, 20.]$ TeV

Table 3.4: List of the scan limits of inputs for GUT archetypes: NUHM2, NUHM2+D, $SU(5)$, and SUGRA12.
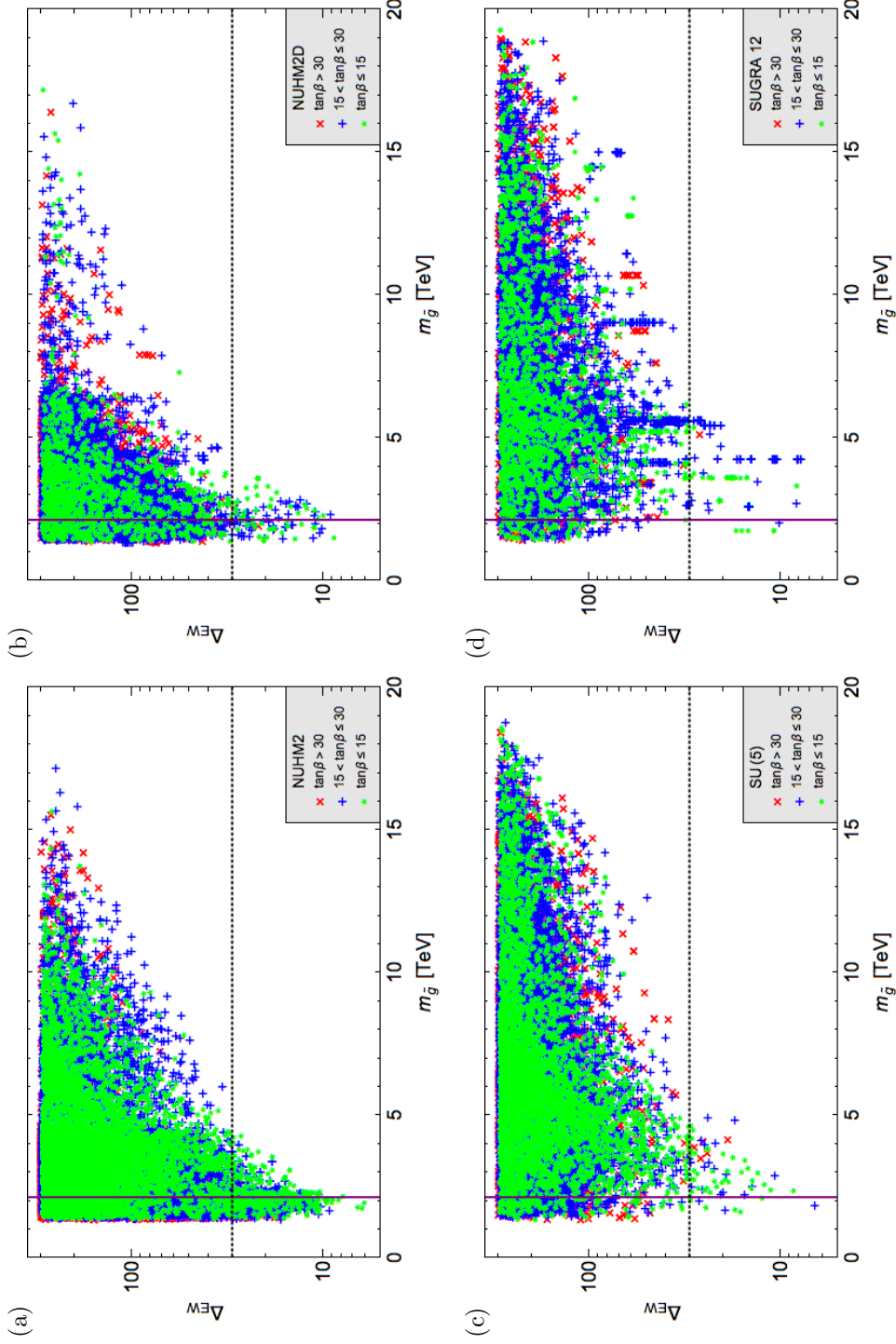
Figure 3.13: Plots of Δ_{EW} vs. $m_{\tilde{g}}$ for archetypes NUHM2, NUHM2+D, $SU(5)$, and SUGRA12 in (a), (b), (c), and (d) respectively. Models are separated by $\tan\beta$ into low ($\tan\beta \leq 15$), mid ($15 < \tan\beta \leq 30$) and high ($30 < \tan\beta \leq 60$) regions. The vertical line displays the current limit from LHC of 2.1 TeV.
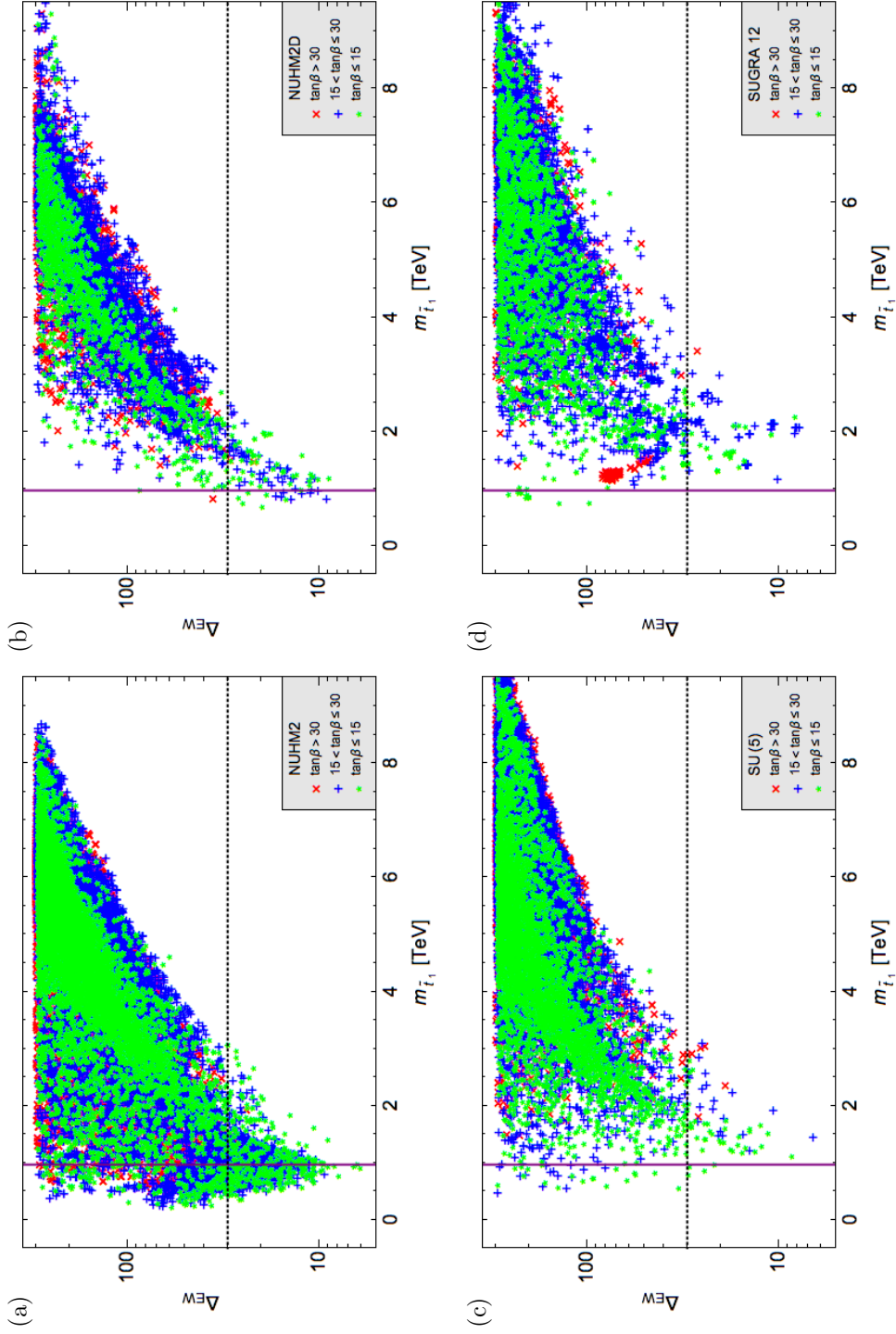
Figure 3.14: Plots of Δ_{EW} vs. $m_{\tilde{t}_1}$ for archetypes NUHM2, NUHM2+D, $SU(5)$, and SUGRA12 in (a), (b), (c), and (d) respectively. Models are separated by $\tan\beta$ into low ($\tan\beta \le 15$), mid ($15 < \tan\beta \le 30$) and high ($30 < \tan\beta \le 60$) regions. The vertical line displays the current limit from LHC of 0.95 TeV.
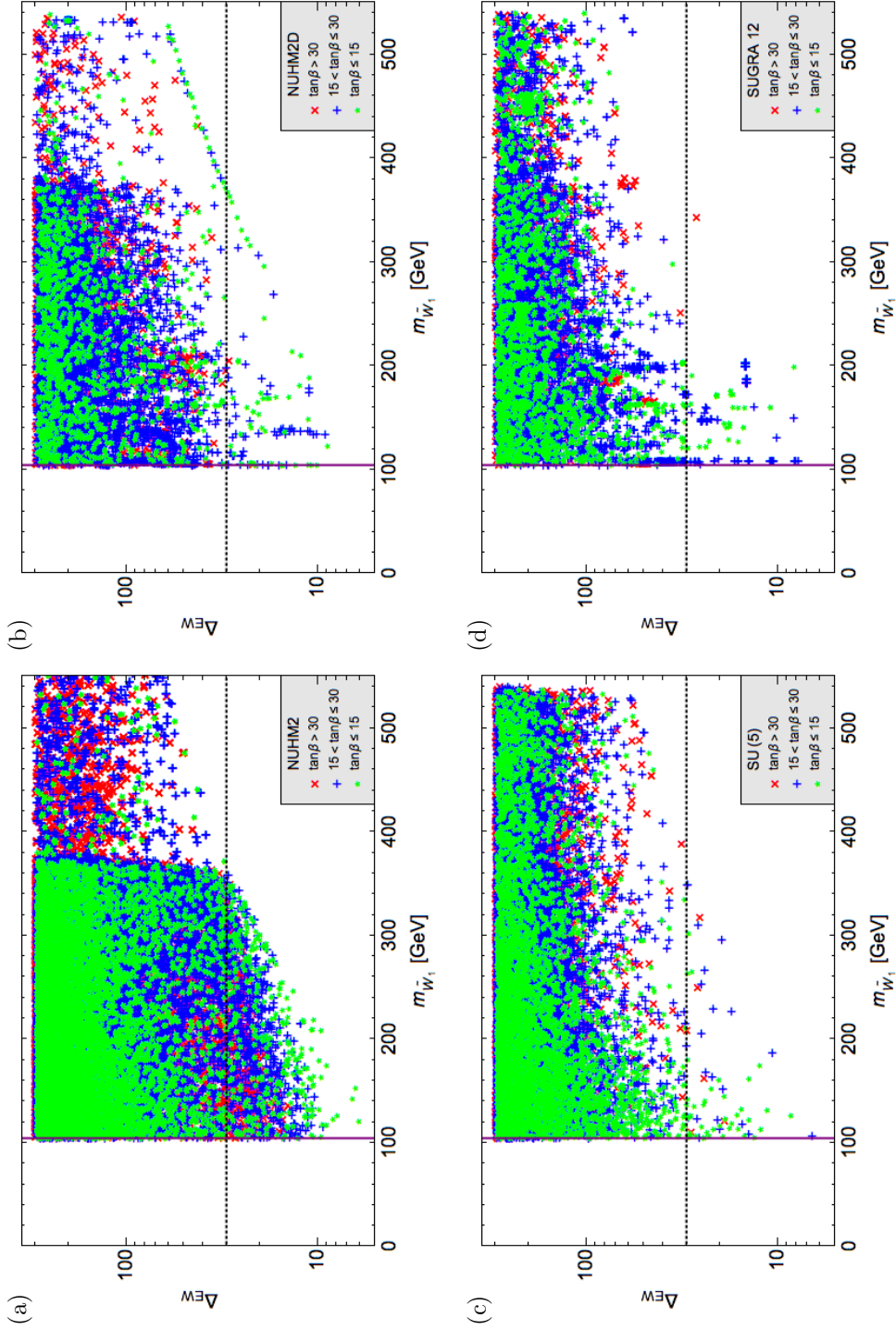
Figure 3.15: Plots of Δ_{EW} vs. $m_{\widetilde{W}_1}$ for archetypes NUHM2, NUHM2+D, $SU(5)$, and SUGRA12 in (a), (b), (c), and (d) respectively. Models are separated by $\tan\beta$ into low ($\tan\beta \leq 15$), mid ($15 < \tan\beta \leq 30$) and high ($30 < \tan\beta \leq 60$) regions. The vertical line displays the current limit from LEP of 103.5 GeV.

63

Parameter	NUHM2 [TeV]	NUM2+D [TeV]	$SU(5)$ [TeV]	SUGRA12 [TeV]
$m_{\tilde{g}}$	4.5	4.0	5.0	5.6
$m_{\tilde{t}_1}$	3.0	2.4	3.1	3.4
$m_{\widetilde{W}_1}$	0.35	0.35	0.32	0.35
μ	0.35	0.35	0.35	0.35
m_h	0.127	0.126	0.127	0.127
m_H	9.0	9.0	9.5	9.5
$m_{H^\pm}$	9.0	9.0	9.5	9.5
m_A	9.0	9.0	9.5	9.5
$m_{\widetilde{Z}_1}$	0.35	0.35	0.35	0.35
$m_{\widetilde{Z}_2}$	0.35	0.35	0.35	0.35
$m_{\widetilde{Z}_3}$	0.90	0.70	1.0	1.2
$m_{\widetilde{Z}_4}$	1.6	1.3	1.8	2.2
$m_{\widetilde{W}_2}$	1.6	1.3	1.9	2.2
$m_{\tilde{t}_2}$	9.0	5.3	8.5	9.0
$m_{\tilde{b}_1}$	9.0	5.3	8.0	9.0
$m_{\tilde{b}_2}$	13.	12.	10.	13.
$m_{\tilde{\tau}_1}$	12.	6.8	9.0	12.
$m_{\tilde{\tau}_2}$	13.	12.	11.	13.
m_{gen1}	13.	7.5	13.	13.
m_{gen2}	13.	7.5	13.	13.
$M_1(\text{GUT})$	0.85	0.70	1.0	1.2
$M_2(\text{GUT})$	1.5	1.3	1.8	2.1
$M_3(\text{GUT})$	4.0	3.5	4.5	5.3

Table 3.5: Limits on parameters in GUT archetypes: NUHM2, NUHM2+D, $SU(5)$, and SUGRA12. Above the double line are results shown in fig. 3.13, fig. 3.14, and fig. 3.15 and below the double line the associated figures are not shown here.

3.5 Generalized mirage mediation

All of the GUT models considered have assumed gravity mediation as the dominant form of SUSY breaking. Here, gravity mediation will be combined with anomaly mediation to form generalized mirage mediation (GMM). String theory offers a UV complete, finite theory treating gravity quantum mechani-

cally. The low energy, effective string theory can include the SM. String theory, formulated as 10-dimensional superstring or 11-dimensional M-theory, has a vast landscape for 4-D theories after compactification of the extra dimensions. Much work has been done to understand how the SM or SUSY may arise from these compactifications[45, 46]. Because string theory includes a high mass scale, M_{string}, near m_{GUT}, the low energy, effective theory is desired to be the MSSM due to its handling of the Higgs mass stability[15].

The small subspace of the landscape vacua in string theory that provides phenomenological viable, low energy theories is known as the mini-landscape[47, 48]. The mini-landscape assumes the gauge structure $E_8 \otimes E_8$. One E_8 may contain a hidden sector with subgroups, $SU(n)$, that are strongly interacting at an intermediate scale $\Lambda \approx 10^{13}$ GeV. These interacting subgroups would lead to gaugino condensation, leading to supergravity breaking[49–51].

Grand unified structures and the SM are subgroups of E_8 as seen in $E_8 \supset E_6 \supset SO(10) \supset SU(5) \supset SU(3)_C \otimes SU(2)_L \otimes U(1)_Y$. The herotic string group, E_8, can be compactified on a $Z_6 - II$ orbifold[52] to arrive at the low energy theories of the MSSM and SM, potentially with additional exotic matter states. The properties of the low energy theory, after compactification down to 4-D, is essentially determined by the geometry, and location, of the matter superfields on the compactified manifold. The low energy gauge theory is the SM group, with possible symmetry enhancements for fields confined to fixed points, fixed tori, or in extra dimensions. Models that provide an MSSM-like structure have the following in common[53]:

- The Higgs, H_u and H_d, are bulk fields that live in the untwisted sector with SM gauge symmetry, resulting in incomplete GUT multiplets, solving the doublet-triplet splitting problem.

- The first two matter generations live on fixed orbifold points with $SO(10)$ symmetry, filling the 16-dimensional spinor representation. These do not extend into the bulk and lead to small Yukawa couplings.

- Third generation quark doublet and top singlet live in the bulk with the Higgs, leading to large Yukawa couplings. Other third generation matter fields' residence is model dependent.

- Supergravity breaking may arise from gaugino condensation at a scale $\Lambda \approx 10^{13}$ GeV, providing a gravitino mass of $m_{3/2} \approx \Lambda^3/m_{\rm pl}^2$. Due to the various locations of the MSSM fields, the effects of SUSY breaking are experienced differently:

  - the Higgs and top squark fields in the untwisted sector experience extended supersymmetry (at tree level) in 4-D, being more protected[54, 55], leading to masses, $m \approx m_{3/2}/(4\pi^2)$,

  - the first/second generation matter scalars on fixed orbifold points are protected by only $N = 1$ supersymmetry, leading to masses $m \approx m_{3/2}$,

  - the gaugino masses and trilinear soft terms are suppressed by the same $4\pi^2 \approx \log(m_{\rm pl}/m_{3/2})$ factor as the Higgs and top squark masses.

Suppression of different soft SUSY breaking terms implies anomaly-mediated loop corrections[56–59] and modulus- (gravity-) mediated contributions are comparable, resulting in mixed moduli-anomaly mediation[60–64] or mirage mediation

66

(MM) for short. Within MM, gaugino masses unify at an intermediate scale,

$$\mu_{\text{mir}} \approx m_{\text{GUT}}\, e^{-8\pi^2/\alpha} \ , \tag{3.4}$$

where α is a parametrization of the amount of anomaly mediation to gravity mediation in SUSY breaking. The MM, SSB Lagrangian terms[60–66] are:

$$M_a = M_s \left(\alpha + b_a\, g_a^2 \right) \ ,$$

$$A_{ijk} = M_s \left(-a_{ijk}\, \alpha + \gamma_i + \gamma_j + \gamma_k \right) \ ,$$

$$m_i^2 = M_s^2 \left(c_i\, \alpha^2 + 4\, \alpha\, \xi_i - \dot{\gamma}_i \right) \ ,$$

$$c_i = 1 - n_i \ ,$$

$$a_{ijk} = 3 - n_i - n_j - n_k \ ,$$

$$\xi_i = \sum_{j,k} a_{ijk}\, \frac{y_{ijk}^2}{4} - \sum_a g_a^2\, C_2^a(f_i) \ ,$$

$$\dot{\gamma}_i = 8\pi^2\, \frac{\partial \gamma_i}{\partial (\ln \mu)} \ , \tag{3.5}$$

where $M_s = \frac{m_{3/2}}{16\pi^2}$, b_a are the β function coefficients for gauge group a with gauge couplings, g_a, y_{ijk} are the superpotential Yukawa couplings, C_2^a is the quadratic Casimir for the ath gauge group containing sfermion $\tilde{f}_i$, γ_i is the anomalous dimension, and n_i are the modular weights.

The parameter space of MM is given by

$$m_{3/2}, \ \alpha, \ \tan\beta, \ \text{sign}(\mu), \ n_i \ . \tag{3.6}$$

67

The original models, where n_i adopted only values of 0, 1/2, or 1, involve a large amount of fine-tuning[28]. To generalize this to allow for soft masses determined by field location in the compactification dimensions, the MM is extended to the generalized mirage mediation (GMM) with parameters[67]:

$$m_{3/2}, \ \alpha, \ c_m, \ c_{m3}, \ a_3, \ \tan\beta, \ \mu, \ m_A, \tag{3.7}$$

where c_m is for the first/second generation and c_{m3} is for the third generation matter scalars, and a_3 is short for $a_{Q_3 H_u U_3}$. The SSB Lagrangian terms for the GMM model are:

$$M_a = M_s \left(\alpha + b_a \, g_a^2 \right) \ ,$$

$$A_\tau = M_s \left(-a_3 \, \alpha + \gamma_{L_3} + \gamma_{H_d} + \gamma_{E_3} \right) \ ,$$

$$A_b = M_s \left(-a_3 \, \alpha + \gamma_{Q_3} + \gamma_{H_d} + \gamma_{D_3} \right) \ ,$$

$$A_t = M_s \left(-a_3 \, \alpha + \gamma_{Q_3} + \gamma_{H_u} + \gamma_{U_3} \right) \ ,$$

$$m_i^2(1,2) = M_s \left(c_m \, \alpha^2 + 4 \, \alpha \, \xi_i - \dot{\gamma}_i \right) \ ,$$

$$m_j^2(3) = M_s \left(c_{m3} \, \alpha^2 + 4 \, \alpha \, \xi_j - \dot{\gamma}_j \right) \ ,$$

$$m_{H_{u,d}} = M_s \left(c_{H_{u,d}} \, \alpha^2 + 4 \, \alpha \, \xi_{H_{u,d}} - \dot{\gamma}_{H_{u,d}} \right) \ , \tag{3.8}$$

where $i \in \{Q_{1,2}, U_{1,2}, D_{1,2}, L_{1,2}, E_{1,2}\}$ and $j \in \{Q_3, U_3, D_3, L_3, E_3\}$. The common value, c_m, suppresses flavor-changing neutral current processes. With this set of parameters, an analysis similar to one for the GUT models can be done, searching for natural regions and confining the parameter space. To build intuition for the GMM archetype, a benchmark point was found: $m_{3/2} = 10.$ TeV, $\alpha = 20.$, $c_m = 100$, $c_{m3} = 18$, $a_3 = 6.0$, $\tan\beta = 10.$, $\mu = 0.15$ TeV, $m_A = 2.0$ TeV. Using

this benchmark, each input parameter is separately varied and the results for Δ_{EW}, m_h, and $m_{\tilde{t}_1}$ are plotted in fig. 3.16, fig. 3.17, and fig. 3.18. The green star denotes the location of the benchmark point and the red line shows where $\Delta_{EW} \leq 30$ denoting the natural generalized mirage mediation (nGMM) and the blue line shows the unnatural $\Delta_{EW} > 30$. It can be seen that $m_{3/2}$ and a_3 have small, highly variable, natural regions.

Furthermore, c_m and c_{m3} are both varied and the plane is plotted in fig. 3.19 with the blue region showing the unnatural $\Delta_{EW} > 30$, but the natural region is split into two pieces: red for $15 < \Delta_{EW} \leq 30$ and green for $\Delta_{EW} \geq 15$. nGMM is confined to a narrow region along which c_m is as large as possible while still maintaining EWSB, where the most natural models lie along the EWSB boundary.
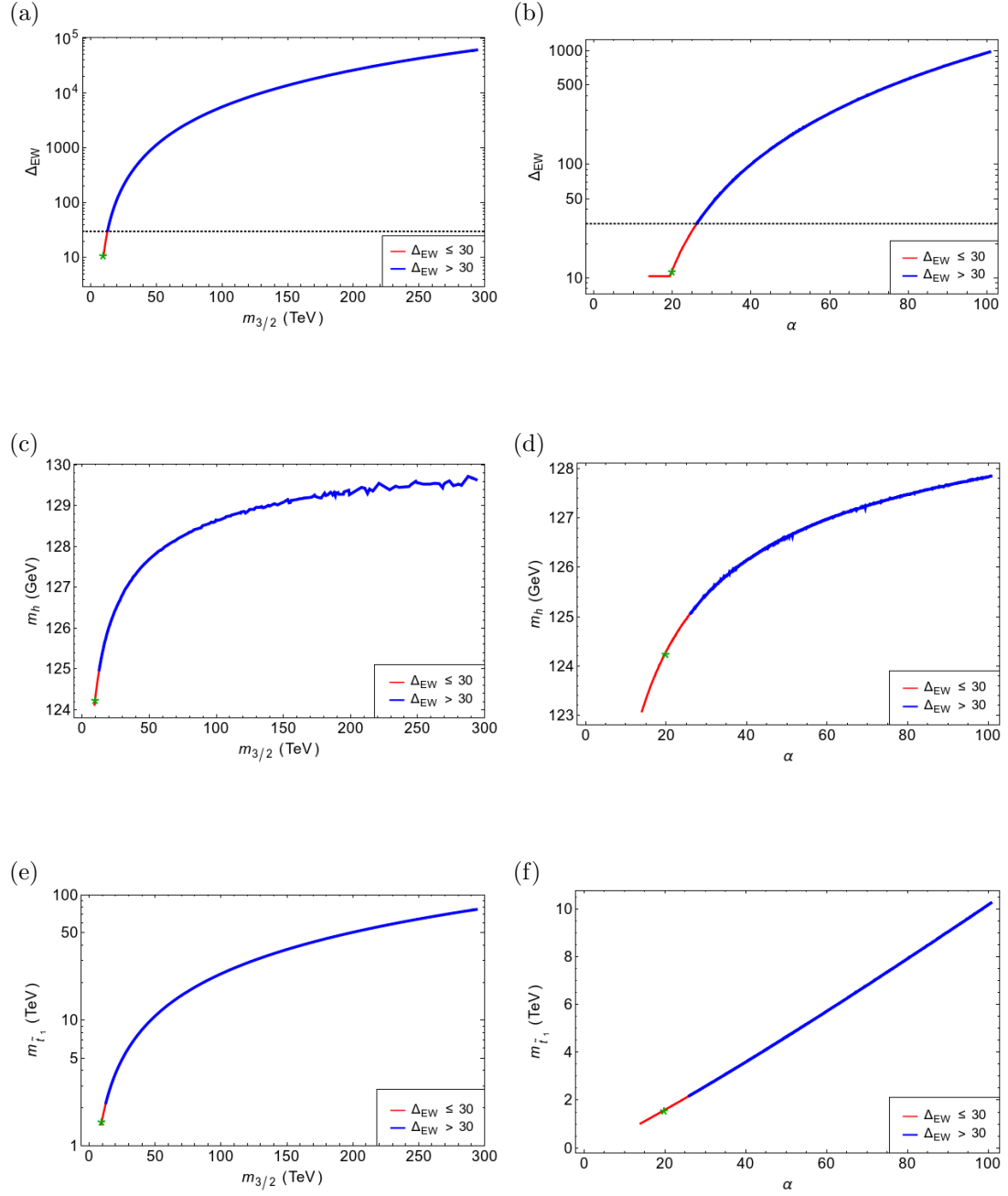
Figure 3.16: Plots of Δ_{EW}, m_h, and $m_{\tilde{t}_1}$ vs. $m_{3/2}$ (left) and α (right). The blue is for $\Delta_{EW} > 30$ and red for $\Delta_{EW} \leq 30$. The green star denotes the benchmark point: $m_{3/2} = 10.$ TeV, $\alpha = 20.$, $c_m = 100$, $c_{m3} = 18$, $a_3 = 6.0$, $\tan\beta = 10.$, $\mu = 0.15$ TeV, $m_A = 2.0$ TeV .

Figure 3.17: Plots of Δ_{EW}, m_h, and $m_{\tilde{t}_1}$ vs. c_m (left) and c_{m3} (right). The blue is for $\Delta_{EW} > 30$ and red for $\Delta_{EW} \leq 30$. The green star denotes the benchmark point: $m_{3/2} = 10.$ TeV, $\alpha = 20.$, $c_m = 100$, $c_{m3} = 18$, $a_3 = 6.0$, $\tan\beta = 10.$, $\mu = 0.15$ TeV, $m_A = 2.0$ TeV .
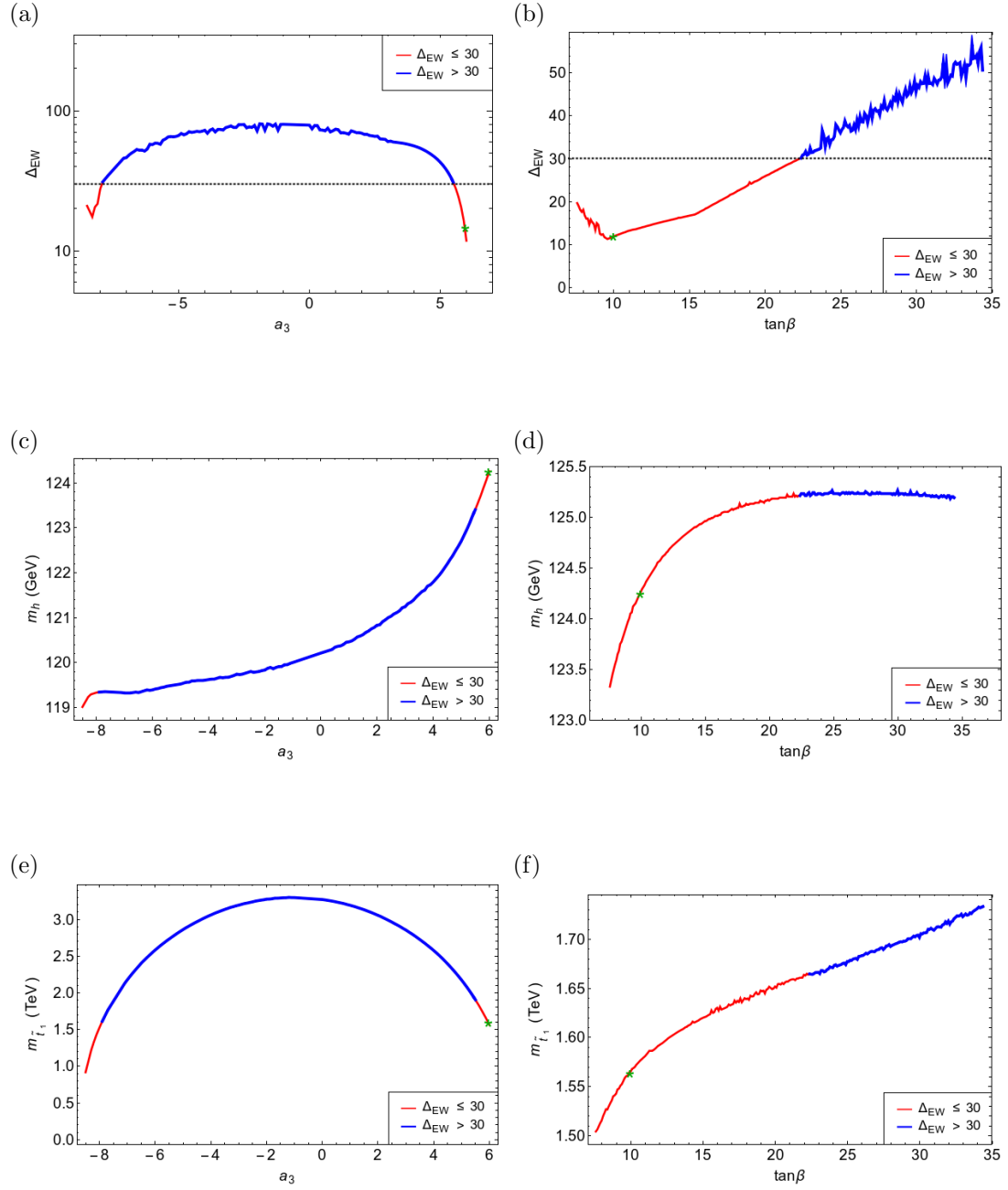
Figure 3.18: Plots of Δ_{EW}, m_h, and $m_{\tilde{t}_1}$ vs. a_3 (left) and $\tan\beta$ (right). The blue is for $\Delta_{EW} > 30$ and red for $\Delta_{EW} \leq 30$. The green star denotes the benchmark point: $m_{3/2} = 10.$ TeV, $\alpha = 20.$, $c_m = 100$, $c_{m3} = 18$, $a_3 = 6.0$, $\tan\beta = 10.$, $\mu = 0.15$ TeV, $m_A = 2.0$ TeV .
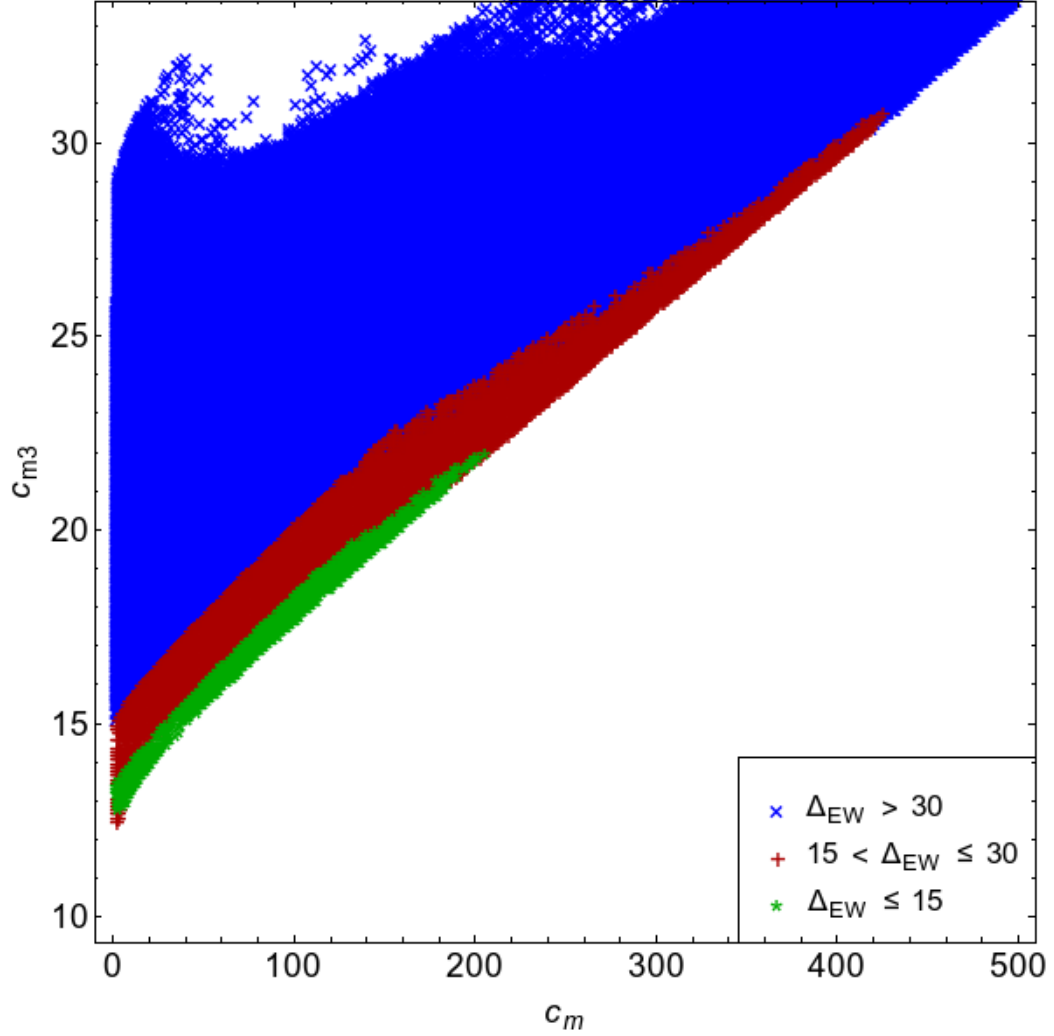
Figure 3.19: Δ_{EW} in the c_{m3} vs c_m plane for the benchmark point: $m_{3/2} = 10.$ TeV, $\alpha = 20.$, $c_m = 100$, $c_{m3} = 18$, $a_3 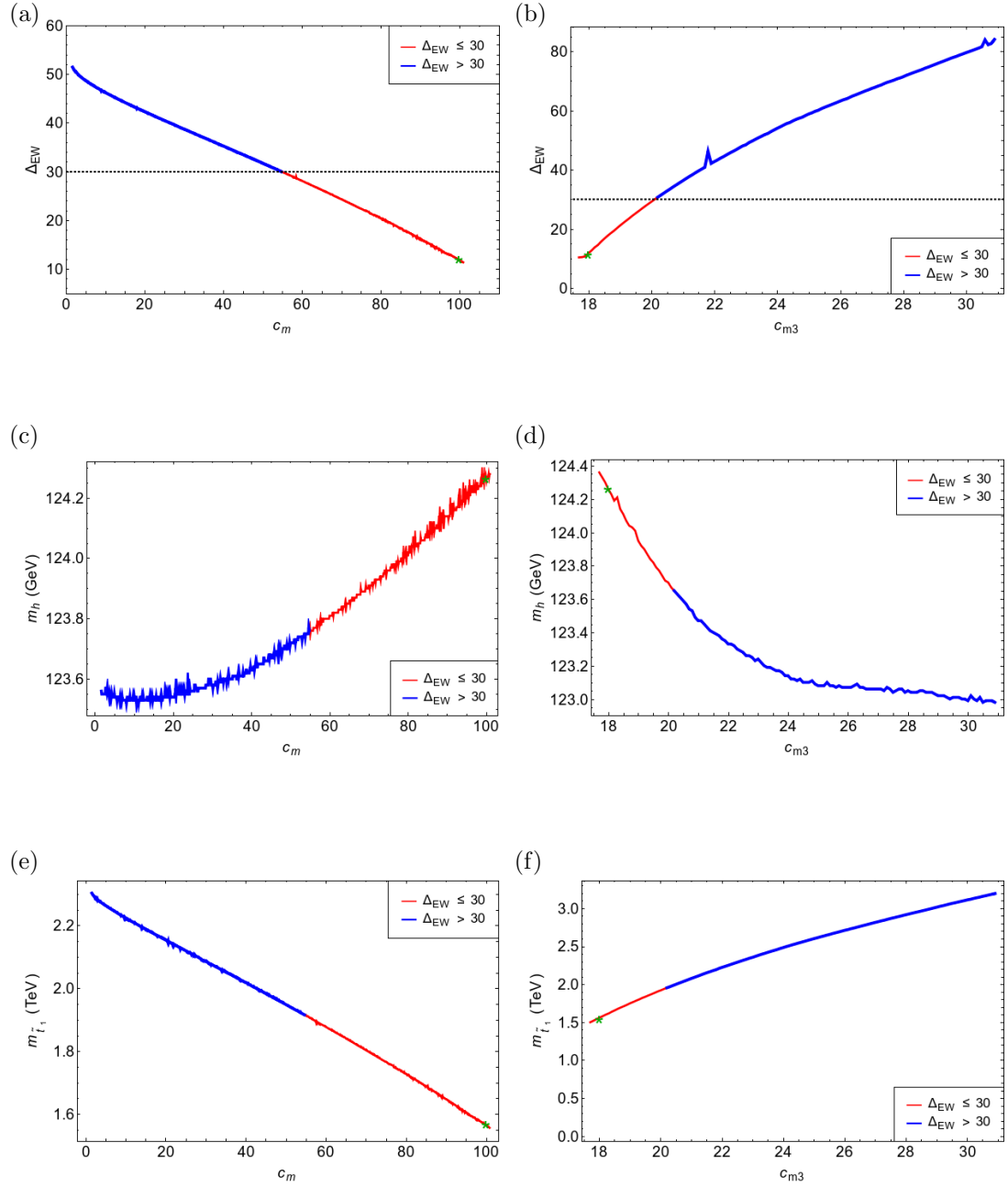= 6.0$, $\tan\beta = 10.$, $\mu = 0.15$ TeV, $m_A = 2.0$ TeV, varying c_m and c_{m3}. The empty space on the right is where EWSB does not occur. The gap in the blue region for higher c_{m3} has $m_h < 123$ GeV.

Table 3.6 lists the ranges of values for the scan, conducted with Isajet7.86.

Parameter	Scan Limits
$m_{3/2}$	$[10., 300]$ TeV
α	$[2.0, 20.]$
c_m	$[1.0, 40.]$
c_{m3}	$[1.0, 40.]$
a_3	$[-10., 10.]$
$\tan\beta$	$[3.0, 60.]$
μ	$[0.10, 0.50]$ TeV
m_A	$[0.30, 8.0]$ TeV

Table 3.6: List of ranges of input parameters for GMM archetype

Additional constraints imposed for a model to be valid are:

- EW symmetry is appropriately broken,

- the Higgs mass falls within $m_h = (125 \pm 2)$ GeV,

- $m_{\tilde{g}} > 2.1$ TeV (in accord with recent LHC13 $\tilde{g}\tilde{g}$ searches), and

- $m_{\tilde{t}_1} > 0.95$ TeV (in accord with recent LHC13 $\tilde{t}_1\tilde{t}_1$ searches)[68, 69].

An analysis similar to the GUT models has been done for GMM. The optimization algorithm used before was modified to simultaneously maximize $m_{\tilde{g}}$ and $m_{\tilde{t}_1}$ while maintaining $\Delta_{EW} \leq 30$. The highest $m_{\tilde{g}}$ and $m_{\tilde{t}_1}$ with $\Delta_{EW} \leq 29$ found in the general scan were chosen as the starting points for the optimization algorithm. Results on the limits of natural parameter space are shown in fig. 3.20. The red, blue, and green points are from the general scan and the yellow points are from the optimization algorithm. Results for nGMM inputs are listed in table 3.7 and full results in table 3.8.
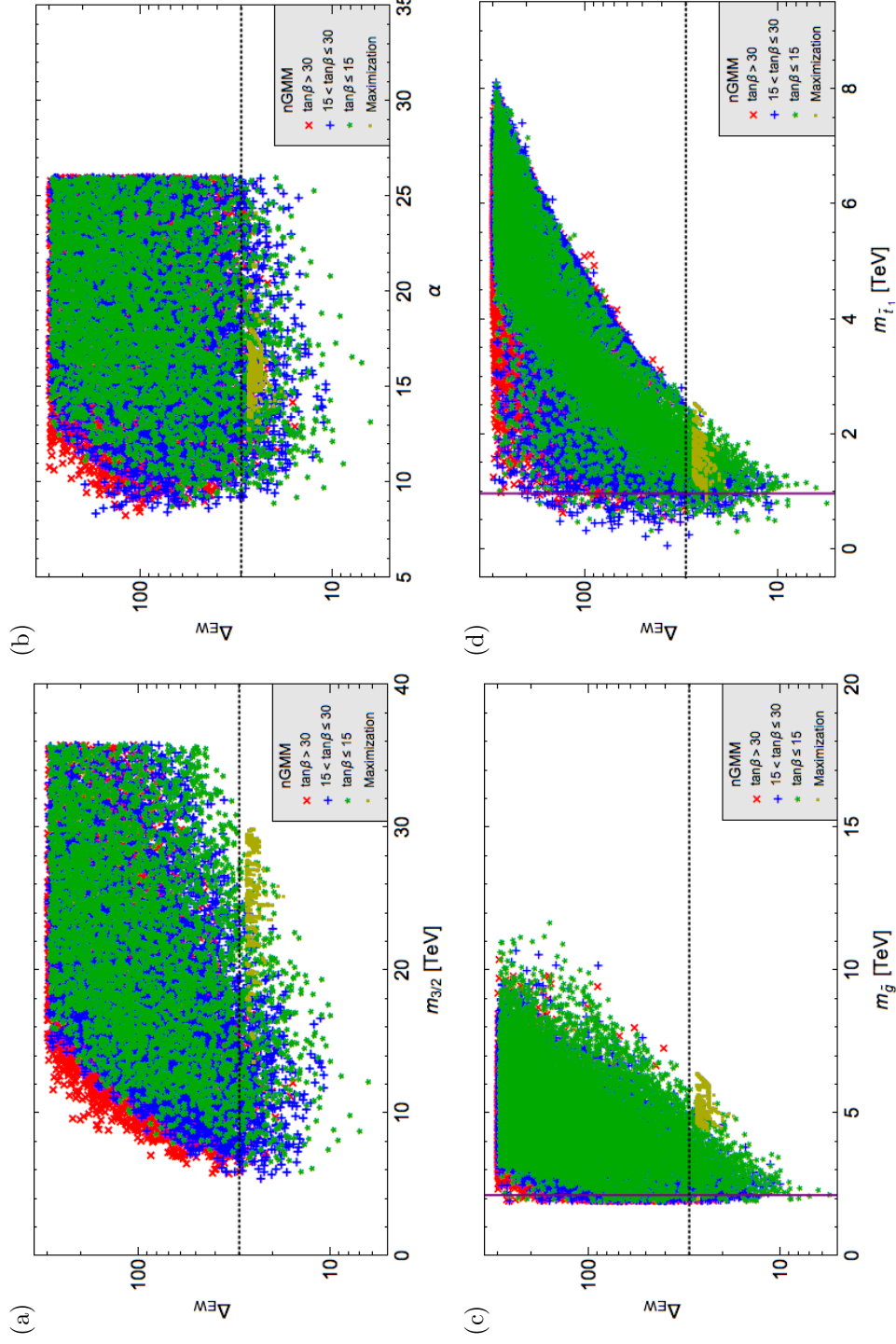
Figure 3.20: Plots of Δ_{EW} vs. $m_{3/2}$, α, $m_{\tilde{g}}$, and $m_{\tilde{t}_1}$ in (a), (b), (c), and (d) respectively for the nGMM archetype. Models are separated by $\tan\beta$ into low ($\tan\beta \leq 15$), mid ($15 < \tan\beta \leq 30$) and high ($30 < \tan\beta \leq 60$) regions. The yellow points are results from the optimization of $m_{\tilde{g}}$ and $m_{\tilde{t}_1}$.

75

Parameter	Limit
$m_{3/2}$	30 TeV
α	> 26
c_m	420
c_{m3}	31
a_3	10.5
μ	0.35 TeV
m_A	6.5 TeV

Table 3.7: List of limits on the parameter space for the nGMM inputs.

The nGMM archetype is unique from the GUT models in the sense that it can probe the gravitino mass, finding a maximum of $m_{3/2} \approx 30$ TeV. Furthermore, the value of α will determine how far from the GUT scale the gaugino masses unify. For a lower limit of $\alpha \approx 8.5$, $\mu_{\mathrm{mir}} \approx 10^{15}$, not too far from m_{GUT}. From the full results, the gluino mass in nGMM can reach as high as 6 TeV. The current $m_{\tilde{g}}$ exclusion from LHC is 2.1 TeV, with an expected exclusion at 3000 fb^{-1} = 2.3 TeV. At 14 TeV, the HL-LHC won't even probe all of $\Delta_{EW} \leq 20$. The top squark mass for nGMM can only reach 2.3 TeV, while reaching up to 3.4 TeV in SUGRA12, while maintaining naturalness. While the gluino may be heavier in nGMM than other archetypes, the top squark tends to be lighter. Hopefully light stops will help in searching the parameter space. The $m_{\tilde{t}_1} - m_{\tilde{g}}$ plane is shown for GMM in fig. 3.21. Fortunately, for the heaviest gluinos, $m_{\tilde{g}} \approx 6$ TeV, the top squarks are quite light, $m_{\tilde{t}_1} \approx 1$ TeV.
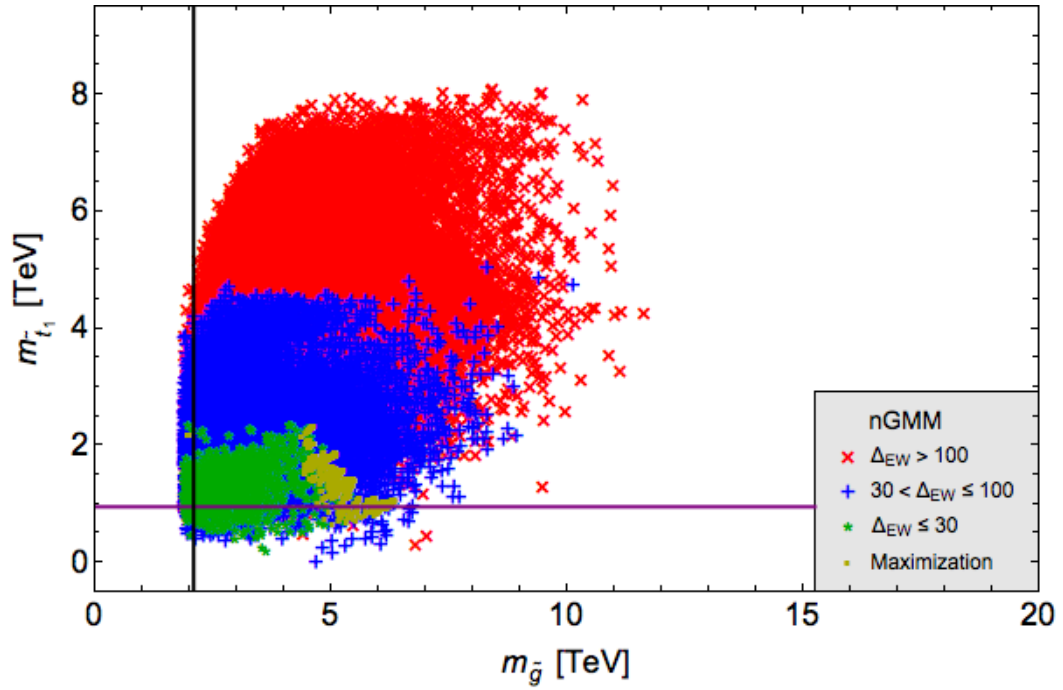
Figure 3.21: Plot of Δ_{EW} in the $m_{\tilde{t}_1} - m_{\tilde{g}}$ plane. $\Delta_{EW} > 100$ in red, $30 < \Delta_{EW} \leq 100$ in blue, and $\Delta_{EW} \leq 30$ in green and yellow. The yellow points were obtained from the optimization algorithm, maximizing $m_{\tilde{g}}$ and $m_{\tilde{t}_1}$ while maintaining $\Delta_{EW} \leq 30$. The vertical(horizontal) black(purple) line shows the current experimental limit of 2.1(0.95) TeV on $m_{\tilde{g}}(m_{\tilde{t}_1})$.

Parameter	NUHM2 [TeV]	NUM2+D [TeV]	$SU(5)$ [TeV]	SUGRA12 [TeV]	nGMM [TeV]
$m_{\tilde{g}}$	4.5	4.0	5.0	5.6	6.0
$m_{\tilde{t}_1}$	3.0	2.4	3.1	3.4	2.3
$m_{\widetilde{W}_1}$	0.35	0.35	0.32	0.35	0.37
μ	0.35	0.35	0.35	0.35	0.35
m_h	0.127	0.126	0.127	0.127	0.127
m_H	9.0	9.0	9.5	9.5	6.5
$m_{H^\pm}$	9.0	9.0	9.5	9.5	6.5
m_A	9.0	9.0	9.5	9.5	6.5
$m_{\widetilde{Z}_1}$	0.35	0.35	0.35	0.35	0.35
$m_{\widetilde{Z}_2}$	0.35	0.35	0.35	0.35	0.36
$m_{\widetilde{Z}_3}$	0.90	0.70	1.0	1.2	1.6
$m_{\widetilde{Z}_4}$	1.6	1.3	1.8	2.2	2.6
$m_{\widetilde{W}_2}$	1.6	1.3	1.9	2.2	2.6
$m_{\tilde{t}_2}$	9.0	5.3	8.5	9.0	6.2
$m_{\tilde{b}_1}$	9.0	5.3	8.0	9.0	6.3
$m_{\tilde{b}_2}$	13.	12.	10.	13.	8.7
$m_{\tilde{\tau}_1}$	12.	6.8	9.0	12.	8.3
$m_{\tilde{\tau}_2}$	13.	12.	11.	13.	8.9
m_{gen1}	13.	7.5	13.	13.	30.
m_{gen2}	13.	7.5	13.	13.	30.
$M_1(\text{GUT})$	0.85	0.70	1.0	1.2	1.6
$M_2(\text{GUT})$	1.5	1.3	1.8	2.1	2.4
$M_3(\text{GUT})$	4.0	3.5	4.5	5.3	5.2

Table 3.8: Expanded table 3.5 to include limits from nGMM.

Chapter 4

Collider signatures

What do the results from chapter 3 experimentally say about supersymmetry? Can natural SUSY be detected or is it only a hope for the distant future? In this chapter, I will present how signals are found at the LHC using two different software methods: Isajet and MadGraph. IsaJet has a sparticle mass spectrum generator that allows for generation of RNS models. IsaJet also computes the appropriate sparticle decay branching fractions and decay widths. To closely connect with previous work in chapter 3, IsaJet is used to simulate background and signal events; however, it only allows for $2 \rightarrow 2$ processes, which would be the dominant modes. In the case where the IsaJet events are significantly small, or zero, after cuts have been applied, the $2 \rightarrow 3$ and $2 \rightarrow 4$ events are significant. In this case, the MadGraph analysis will be used in addition.

Four different signals will be considered: gluino pair production, Same-Sign diBoson (SSdB), higgsino pair production, and top squark pair production. The SSdB and higgsino pair production cuts are optimized for an NUHM2 signal benchmark point for LHC with $\sqrt{s} = 14$ TeV. The $m_{1/2} - m_0$ plane from fig. 3.10 will be updated to include the projected experimental discovery limits for LHC with luminosities of 300 and 3000 fb^{-1}. Additionally, the $\mu - m_{1/2}$ plane will show the discovery limits for both the LHC and the proposed e^+e^- ILC in Japan with $\sqrt{s} = 500$ or 1000 GeV, intended to be a Higgs factory, and consequently, a higgsino factory. The gluino analysis is optimized for LHC with $\sqrt{s} = 33$ TeV. Both the gluino and top squark pair productions show the reach of possible future upgrades of the LHC to $\sqrt{s} = 33$ or 100 TeV.

4.1   Software

In simulating the background and SUSY events, two software packages were implemented: Isajet[36] and MadGraph[70] interfaced with Pythia[71] with the detector simulator Delphes[72]. The following subsections will elaborate on standard definitions and parameters used by Isajet and the changes made to the standard MadGraph cards[73]. Both Isajet and MadGraph are Monte-Carlo event generators used for both the background and SUSY signal events. Isajet is strictly a $2 \to 2$ process generator, whereas MadGraph can also simulate $2 \to 3$ and $2 \to 4$ processes. Isajet has its own SUSY spectrum generator, with various archetypes pre-programmed that includes the substitution of GUT scale m_{H_u} and m_{H_d} for weak scale μ and m_A, which is convenient for generating RNS models. When interfacing between Isajet and other software, Les Houches accord files are generated by Isajet to maintain the particular SUSY spectrum.

4.1.1   Isajet

The Isajet detector simulator[73] has a cell size of $\Delta\eta \times \Delta\phi = 0.05 \times 0.05$ with $-5 < \eta < 5$, where $\eta = -\ln(\tan(\theta/2))$ is the pseudorapidity, ϕ is the azimuthal angle, and θ is the angle from the beam. The hadronic calorimeter has energy resolution of $80\%/\sqrt{E} \oplus 3\%$ for $|\eta| < 2.6$ and $100\%/\sqrt{E} \oplus 5\%$ for $|\eta| > 2.6$. The jet finding algorithm is UA1-like with jet cone size $R = 0.4$ and requires transverse energy, $E_T(\text{jet}) > 50$ GeV and $|\eta(\text{jet})| < 3.0$. A hadronic cluster with $E_T > 50$ GeV and $|\eta(\text{jet})| < 1.5$ is a b-jet if there exists a B hadron with transverse momentum $p_T(B) > 15$ GeV and $|\eta(B)| < 3$ within a cone of $\Delta R \equiv \sqrt{(\Delta\phi)^2 + (\Delta\eta)^2} < 0.5$ around the jet axis. Tagging efficiency of a b-jet is assumed to be 60% with a

light quark and gluon jet mistag rate (based on ATLAS efficiency studies and rejection factors in $t\bar{t}H$ and WH processes[74]) of 1/150 for $E_T < 100$ GeV, 1/50 for $E_T > 250$ GeV, and a linear interpolation for 100 GeV $\leq E_T \leq$ 250 GeV.

The electromagnetic calorimeter has energy resolution of $3\%/\sqrt{E} \oplus 0.5\%$. Leptons are considered isolated if they have $p_T(e$ or $\mu) > 20$ GeV with $|\eta| < 2.5$ with visible activity of ΣE_T(cells) < 5 GeV within a cone of size $\Delta R < 0.2$. These strict isolation critera help reduce multi-lepton backgrounds from heavy quark production.

4.1.2 MadGraph

Events were showered and hadronized using the default MadGraph interfaced with Pythia using the default parameters. Delphes performed the detector simulations using the 3.3.0 "CMS" parameter card with the following changes made to be in agreement with the Isajet simulations[73]:

- set hadronic and electromagnetic calorimeter resolutions to match Isajet,

- turned off jet energy scale correction,

- use anti-k_T jet algorithm[75] with $R = 0.4$ for jet finding with FastJet[76]. The jet criteria were changed to match those from Isajet,

- implement jet flavor association module, based on the "ghost hadron" procedure [77], to unambiguously assign decayed hadrons to jets. A jet with $|\eta| < 1.5$ is a b-jet if there is a B hadron with $|\eta| < 3.0$ and $p_T > 15$ GeV in accordance with Isajet, and lastly,

- turned off tau tagging to remove mistagging a true b-jet as a tau jet when the B hadron decays leptonically to a tau.

81

4.2   Initial cuts

In simulating SUSY processes, the goal is to select processes that give events distinguishable from the known SM backgrounds (BG) events. It is necessary to generate enough background to sample the SM statistically well so results are not due to insufficient numbers in the SM. Table 4.1 lists the background processes and number of events generated with Isajet, as well as the resulting cross section.

To identify which events came from SUSY, signatures must be distinguishable in some way, typically in amount of missing energy, number of b-jets, etc. To help SUSY stand out from the extensive background a set of cuts are implemented to all events, both BG and SUSY signal. A baseline set of cuts, referred to as the C1 cuts, are as follows:

- $\not{E}_T > \max(100 \text{ GeV}, 0.2 M_{\text{eff}})$

- $n_{\text{jets}} \geq 4$,

- $E_T(j_1, j_2, j_3, j_4) > 100, 50, 50, 50 \text{ GeV}$, and

- $S_T > 0.2$,

where $\not{E}_T$ is missing transverse energy; $M_{\text{eff}} \equiv \not{E}_T + E_T(j_1) + E_T(j_2) + E_T(j_3) + E_T(j_4)$; j_1, j_2, j_3, and j_4 are the four highest E_T jets, listed highest to lowest; and S_T is transverse sphericity, defined as

$$S_t = \frac{2\lambda_2}{\lambda_2 + \lambda_1} ,$$

(4.1)

where the λs are the eigenvalues of the S_{xy} matrix

$$S_{xy} = \frac{1}{\sum_i p_{T\mathrm{i}}} \sum_{\mathrm{i}} \frac{1}{p_{T\mathrm{i}}} \begin{bmatrix} p_{x\mathrm{i}}^2 & p_{x\mathrm{i}}p_{y\mathrm{i}} \\ p_{x\mathrm{i}}p_{y\mathrm{i}} & p_{y\mathrm{i}}^2 \end{bmatrix} . \tag{4.2}$$

SM Process		Events	$\sigma(\mathrm{total})$ [fb]	$\sigma(\mathrm{C1})$ [fb]
QCD	($p_T : 50 - 100$ GeV)	10^6	2.6×10^{10}	0
QCD	($p_T : 100 - 200$ GeV)	10^6	1.5×10^9	1.5×10^3
QCD	($p_T : 200 - 400$ GeV)	10^6	7.3×10^7	3.9×10^3
QCD	($p_T : 400 - 1000$ GeV)	10^6	2.7×10^6	4.9×10^2
QCD	($p_T : 1000 - 2400$ GeV)	10^6	1.5×10^4	4.4×10^0
W+jets	($p_T : 100 - 4000$ GeV)	5×10^5	3.9×10^5	1.8×10^3
Z+jets	($p_T : 100 - 3000$ GeV)	5×10^5	1.4×10^5	8.5×10^2
$t\bar{t}$		3×10^6	1.0×10^6	2.0×10^3
$WW,\ WZ,\ ZZ$		5×10^5	8.0×10^4	9.3×10^0

Table 4.1: Background processes and number of events with cross section before and after C1 cuts. The QCD background has been broken up into five processes based on transverse momentum.

To claim a discovery, three criteria must be met:

- $n_{\mathrm{SUSY}} \geq 5\,\sigma_{\mathrm{BG}} \xrightarrow[\mathrm{Gaussian}]{} 5\,\sqrt{n_{\mathrm{BG}}}$

- $n_{\mathrm{SUSY}} \geq 5$

- $n_{\mathrm{SUSY}} \geq 0.2\,n_{\mathrm{BG}}$,

where $n_{\mathrm{SUSY}}(n_{\mathrm{BG}})$ is the total number of signal(background) events for an assumed integrated luminosity. The first criterion is a statistical distinction between SUSY and SM BG, requiring the number of SUSY events to be greater than 5σ in BG to minimize type 1 error rate. The second criterion reduces false claims due to insufficient data. Requiring at least 5 events prevents claims based on few, anomalous events. The last criterion requires sufficient number of SUSY events compared to BG events. With enough data, the SM BG may become known well to reduce σ_{BG} enough for an unreasonably small number of SUSY events to stand out.

With the extensive amount of BG left over after the C1 cuts, a more detailed analysis must be performed. The following sections will investigate optimal cuts for the particular processes of interest and enumerate the results.

4.3   Gluino pair production

Because the LHC is a hadronic machine, colliding protons, gluons are readily available for all production processes. Both quark and gluon pairs contribute to the production of gluinos as shown in fig. 4.1. After production, the gluinos will decay to either $\tilde{g} \rightarrow t\,\bar{t}\,\widetilde{Z}_{\mathrm{i}}$, $\bar{t}\,b\,\widetilde{W}_{\mathrm{i}}^{+}$, or $t\,\bar{b}\,\widetilde{W}_{\mathrm{i}}^{-}$. The lightest two charginos, $\widetilde{W}_{1}^{\pm}$, and two neutralinos, $\widetilde{Z}_{1,2}$, are typically higgsino-like. Through these cascade decays, gluino pair production events will be abundant in b-jets with an isolated lepton, multiple light quark jets, and typical of SUSY events, high missing energy, $\not{E}_{T}$.

Due to the large number of b-jets available from $\tilde{g}\tilde{g}$, the first cut beyond those of C1 would be on the number of b-jets. Figure 4.2 shows the events vs. number of b-jets, broken down by SM process and by same-sign(SS) or opposite-sign(OS) leptons when $n(\mathrm{lep}) = 2$.
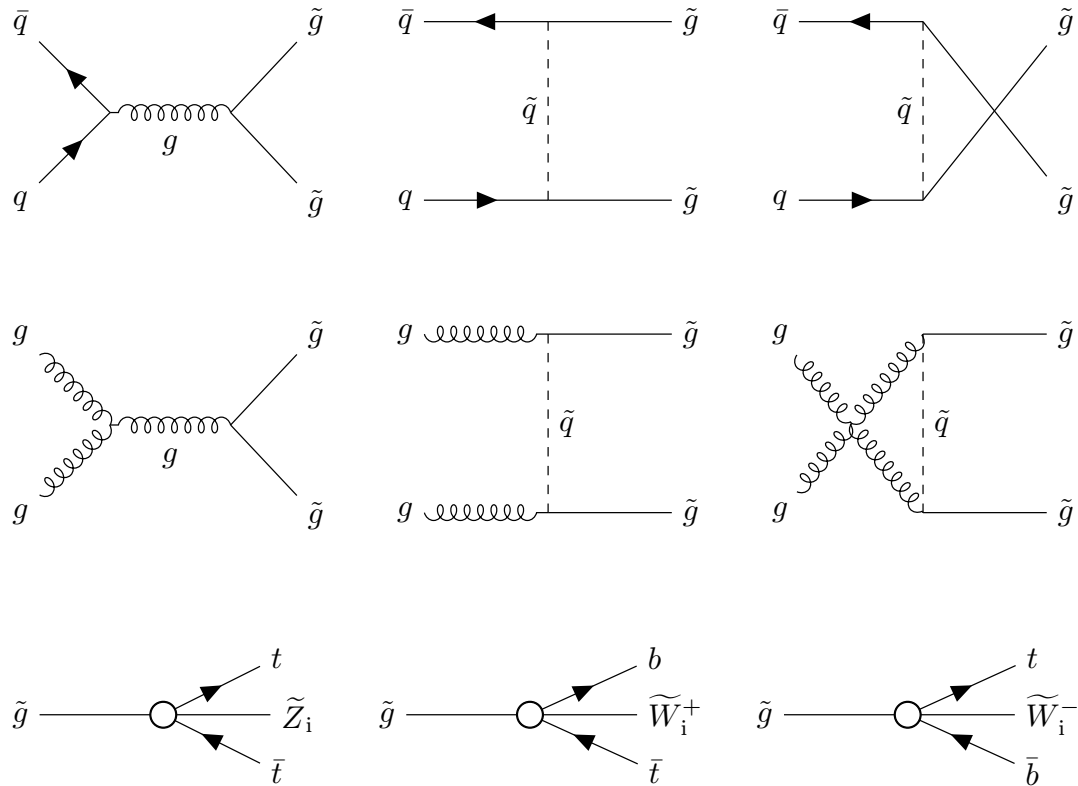
Figure 4.1: Quark (top) and gluon (middle) Feynman diagram contribution to gluino pair production accompanied by decays of the gluino (bottom) to $\widetilde{Z}_i\, t\, t$, $\widetilde{W}_i^+\, \bar{t}\, b$, and $\widetilde{W}_i^-\, t\, \bar{b}$.
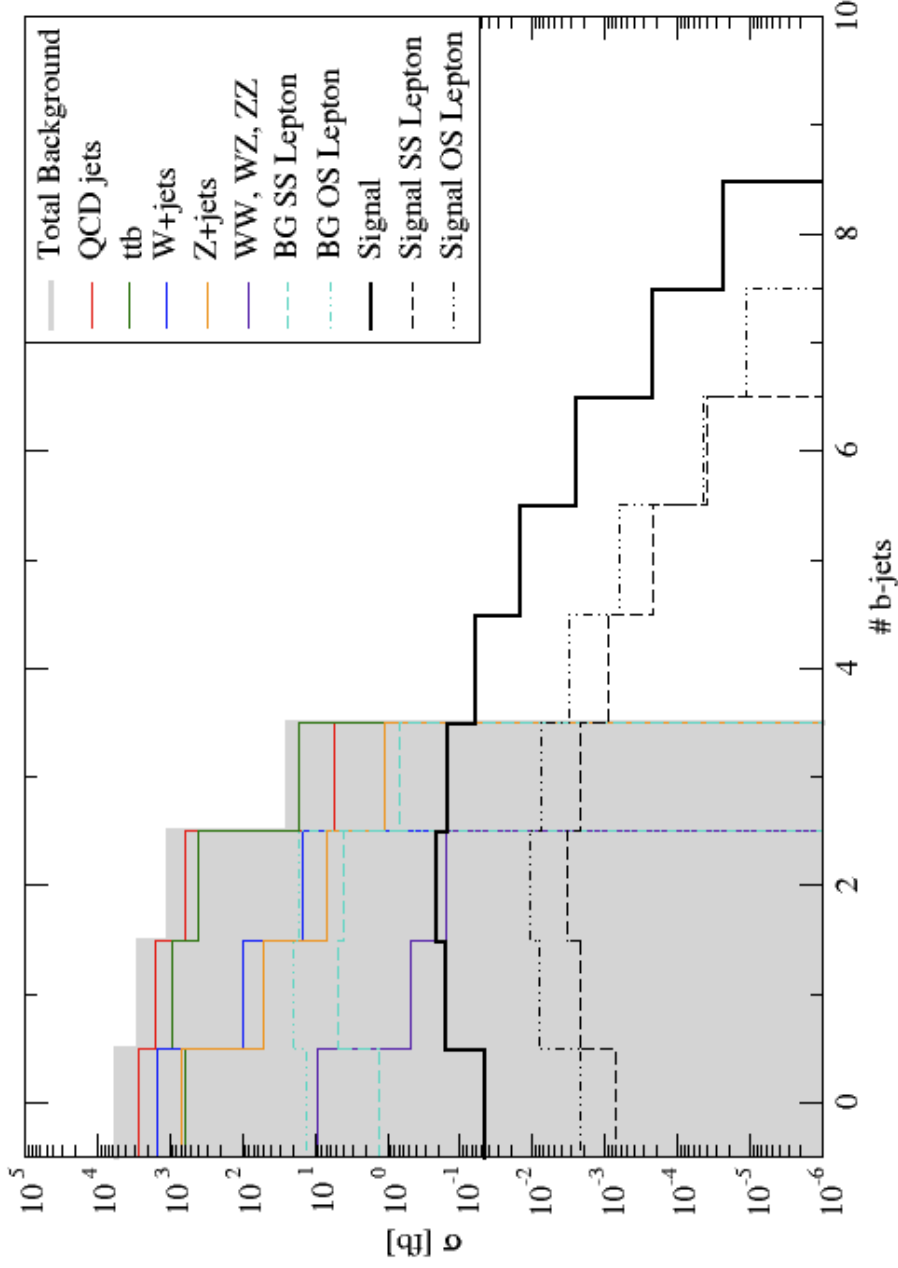
Figure 4.2: Events simulated in Isajet as a function of number of b-jets. The shaded gray region is the total SM background, the red denotes the total QCD background, green is the $t\bar{t}$ background, yellow is the Z+jets, purple is the W+jets, and cyan dashed(dot-dashed) is the SS(OS) background events containing exactly two leptons. The solid black is the total $\tilde{g}\tilde{g}$ signal with the dashed(dot-dashed) for the SS(OS) events.

Cut	σ_{BG} [fb]	σ_{SUSY} [fb]
C1	1.05×10^3	6.31×10^{-1}
C1, $n(b-\text{jet}) \geq 4$	0	7.64×10^{-2}
C1, $n(b-\text{jet}) \geq 3$	2.32×10^1	2.26×10^{-1}
C1, $n(b-\text{jet}) \geq 3$, $\not{E}_T \geq 500$ GeV, $m_T \geq 150$ GeV	1.48×10^{-2}	1.75×10^{-1}
C1, $n(b-\text{jet}) \geq 2$	1.08×10^3	4.35×10^{-1}
C1, $n(b-\text{jet}) \geq 2$, $\not{E}_T \geq 500$ GeV, $m_T \geq 150$ GeV	4.33×10^{-1}	3.33×10^{-1}
C1, $n(b-\text{jet}) \geq 2$, $\not{E}_T \geq 750$ GeV, $m_T \geq 150$ GeV	0	2.18×10^{-1}

**Table** 4.2: List of cuts implemented on Isajet events with resulting BG and signal.

The most obvious way to differentiate the signal from the BG is to select the region where there is no BG, that is with the number of b-jets ≥ 4. While this does eliminate the SM BG from Isajet while keeping $\sigma_{\text{SUSY}} = 0.0764$ fb, this first cut choice is not optimal. An alternative is to make a soft(hard) cut on $n(b-\text{jet}) = 2(3)$. Since there is the most signal in the $n(b-\text{jet}) = 2$ bin, the soft cut is preferred over the hard cut.

A couple further cuts to apply are on transverse missing energy and, if $n_{\text{lep}} = 1$, transverse mass, $\not{E}_T$ and $m_T(\ell, \not{E}_T)$ respectively. Requiring $\not{E}_T > 500$ GeV and $m_T > 150$ GeV leads to cross sections of $\sigma_{BG}(\text{C1}, 2b, \not{E}_T, m_T) = 0.433$ fb and $\sigma_{SUSY}(\text{C1}, 2b, \not{E}_T, m_T) = 0.333$ fb for ≥ 2 b-jets or $\sigma_{BG}(\text{C1}, 3b, \not{E}_T, m_T) = 0.0148$ fb and $\sigma_{SUSY}(\text{C1}, 3b, \not{E}_T, m_T) = 0.175$ fb for ≥ 3 b-jets. The leftover BG is from $t\bar{t}$. Increasing the $\not{E}_T$ cut to $\not{E}_T > 750$ GeV removes all Isajet BG and leaves a total signal of $\sigma_{SUSY}(\text{C1}, 2b, \not{E}_T(750), m_T) = 0.218$ fb. A summary of the cuts is listed in table 4.2.

From these results, it would appear that the cuts (C1, $2b$, $\not{E}_T(750$ GeV), $m_T(150$ GeV)) are optimal; however, this does eliminate all the generated $2 \to 2$ Isajet events. To further analyze this, MadGraph calculated the dominant $2 \to$

$2, 3, 4$ processes involving t and b quarks: $t\bar{t}$, $b\bar{b}Z$, $t\bar{t}b\bar{b}$, and $t\bar{t}t\bar{t}$. Figure 4.3 shows the cuts made to optimize signal detection from MadGraph from 2 b-jets. The resulting cross sections after the (C1, 2b, $\not{E}_T$(750 GeV), m_T(150 GeV)) cuts have been applied are: $\sigma_{t\bar{t}} = 0.134$ fb, $\sigma_{b\bar{b}Z} = 0.0149$ fb, $\sigma_{t\bar{t}b\bar{b}} = 0.013$ fb, and $\sigma_{t\bar{t}t\bar{t}} = 0.000368$ fb totaling $\sigma_{\text{MadGraph}} = 0.160$ fb, which no longer appear so optimal after the MadGraph analysis.

To optimize the MadGraph cuts, an additional cut on $\Delta\phi$ between $\not{E}_T$ and nearest jet (j_1, j_2, j_3, or j_4) was introduced. Figure 4.3(c) shows the distribution of events with respect to $\Delta\phi$. A conservative cut of $\Delta\phi > 30°$ eliminates the highest BG while cutting minimal signal. After the $\Delta\phi$ cut, fig. 4.3(d) shows the distribution in $\not{E}_T$ again, where the cut will be hardened to 900 GeV. The surviving signal after each cut is listed in table 4.3.
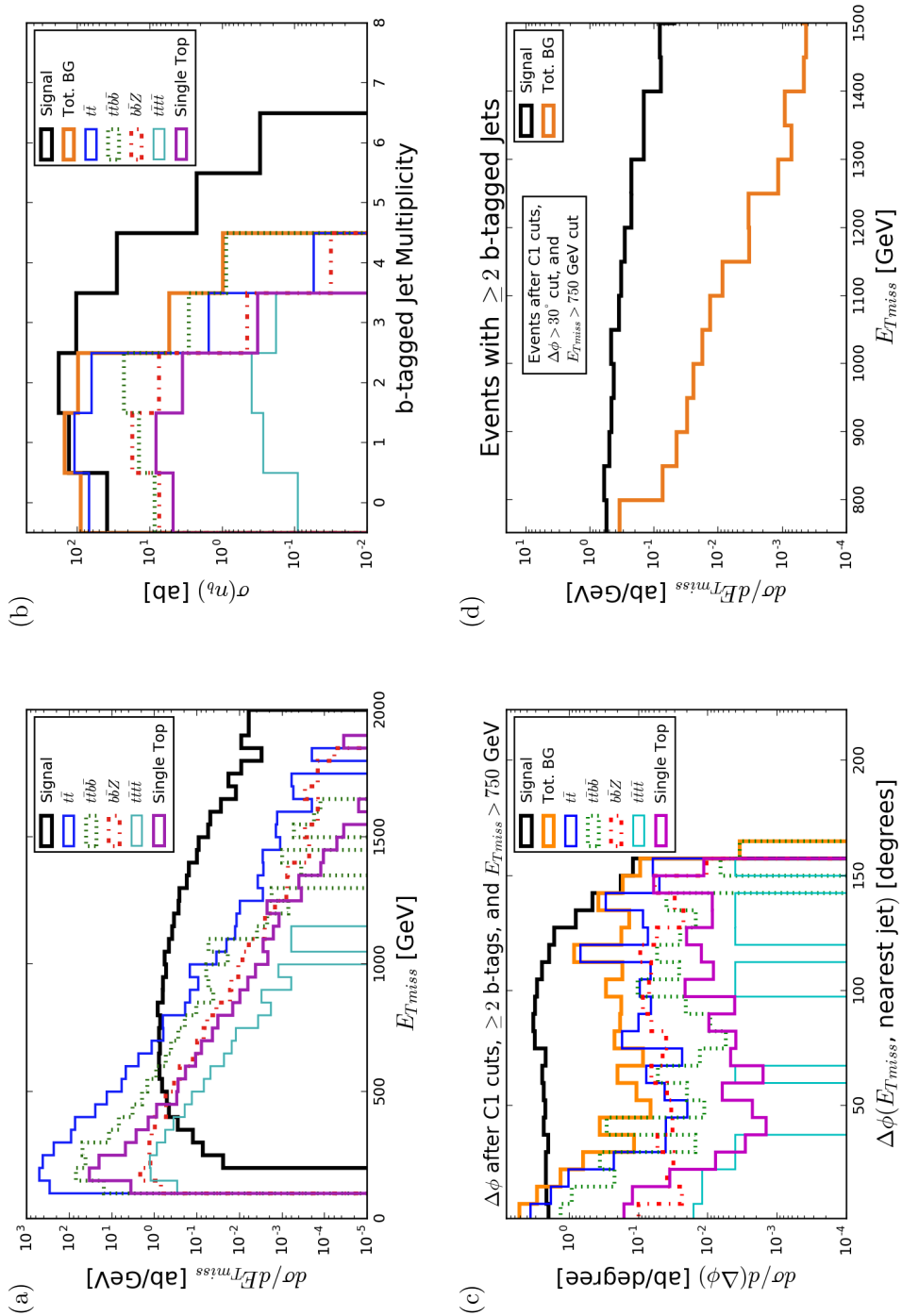
Figure 4.3: Cross sections after cuts from MadGraph analysis plotted against: $\not{E}_T$ after cuts C1 and $m_T(150 \text{ GeV})$ in (a); b-jets after C1, $m_T(150 \text{ GeV})$, and $\not{E}_T(750 \text{ GeV})$ in (b); $\Delta\phi$ after C1, $m_T(150 \text{ GeV})$, $\not{E}_T(750 \text{ GeV})$, and $n(b-\text{jet} \geq 2)$ in (c); and $\not{E}_T$ after C1, $m_T(150 \text{ GeV})$, $\not{E}_T(750 \text{ GeV})$, $n(b-\text{jet} \geq 2)$, and $\Delta\phi > 30°$ in (d).

89

Cut	$\sigma_{BG}(2b)$ [fb]	$\sigma_{SUSY}(2b)$ [fb]	$\sigma_{BG}(3b)$ [fb]	$\sigma_{SUSY}(3b)$ [fb]
C1, $m_T > 150$ GeV	499.	0.872	499.	0.872
$\not{E}_T > 750$ GeV	0.323	0.479	0.323	0.479
b-jets	0.0991	0.311	0.00598	0.133
$\Delta\phi > 30°$	0.0268	0.249	0.00165	0.105
$\not{E}_T > 900$ GeV	0.00502	0.167	0.00165	0.105

Table 4.3: Cuts applied to MadGraph events with surviving cross-section for background and $\tilde{g}\tilde{g}$ SUSY signal for both $2b$ and $3b$ cuts. Each subsequent cut is applied after all previous cuts have been applied.
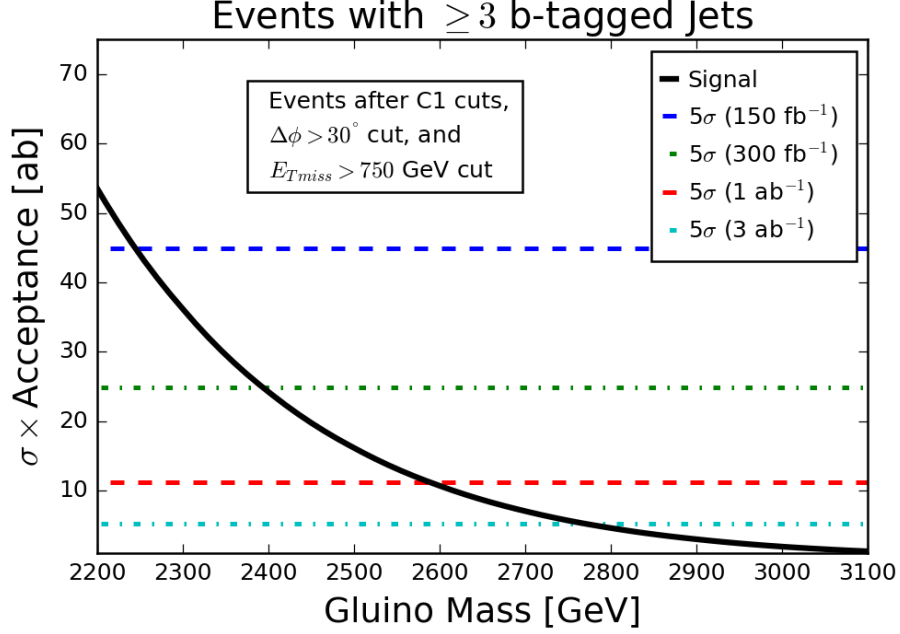
Finally, after establishing optimal cuts to distinguish SUSY $\tilde{g}\tilde{g}$ signal from SM BG, the discovery reach for a gluino can be determined. For a low number of expected events from a low cross section, the central limit theorem will not necessarily apply. Instead of using Gaussian statistics, Poisson statistics are more appropriate. The three criteria listed in section 4.2 are used to find the discovery limit in $m_{\tilde{g}}$, but implementing Poisson statistics with an α cutoff of 2.87×10^{-7} for the first criterion. The range of $m_{\tilde{g}}$ that can be discovered at HL-LHC is shown in fig. 4.4 with assumed luminosities of $L = \{150, 300, 1000, 3000\}$ fb^{-1}. A summary of reach limits for HL-LHC and possible future upgrades is shown in fig. 4.5[78]. The possible upgrades are to $\sqrt{s} = 33$ TeV with a discovery(5σ) limit of $m_{\tilde{g}} = 5.2$ TeV and exclusion limit(95% CL) $m_{\tilde{g}} = 6.2$ TeV or to $\sqrt{s} = 100$ TeV with a discovery limit of $m_{\tilde{g}} = 10.5$ TeV.

Events with ≥ 2 b-tagged Jets

Events after C1 cuts,
$\Delta\phi > 30°$ cut, and
$E_{Tmiss} > 900$ GeV cut

— Signal
-- 5σ (150 fb^{-1})
.. 5σ (300 fb^{-1})
-- 5σ (1 ab^{-1})
-.. 5σ (3 ab^{-1})
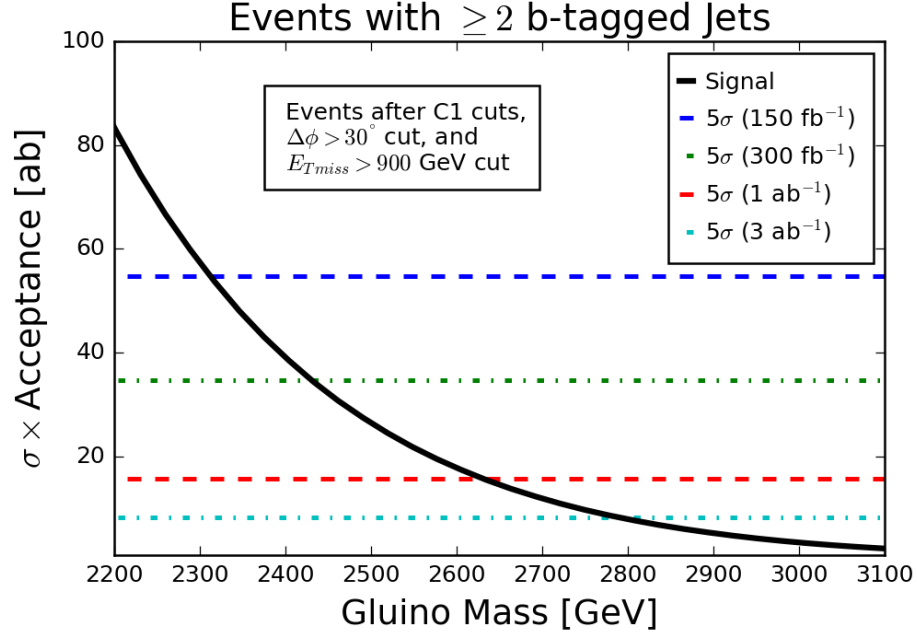
(a) With $n(b-\text{jet}) \geq 2$, the discovery reach is $m_{\tilde{g}} = \{2320, 2430, 2630, 2800\}$ GeV for $\sqrt{s} = 14$ TeV with $L = \{150, 300, 1000, 3000\}$ fb^{-1}.

Events with ≥ 3 b-tagged Jets

Events after C1 cuts,
$\Delta\phi > 30°$ cut, and
$E_{Tmiss} > 750$ GeV cut

— Signal
-- 5σ (150 fb^{-1})
.. 5σ (300 fb^{-1})
-- 5σ (1 ab^{-1})
-.. 5σ (3 ab^{-1})

(b) With $n(b-\text{jet}) \geq 3$, the discovery reach is $m_{\tilde{g}} = \{2240, 2390, 2590, 2780\}$ GeV for $\sqrt{s} = 14$ TeV with $L = \{150, 300, 1000, 3000\}$ fb^{-1}.

Figure 4.4: Discovery reach with $n(b-\text{jet}) \geq 2$ in (a) and $n(b-\text{jet} \geq 3)$ in (b). The solid black line is the SUSY cross section and the dashed {blue, green, red, cyan} lines are for luminosities of {150, 300, 1000, 3000} fb^{-1}.
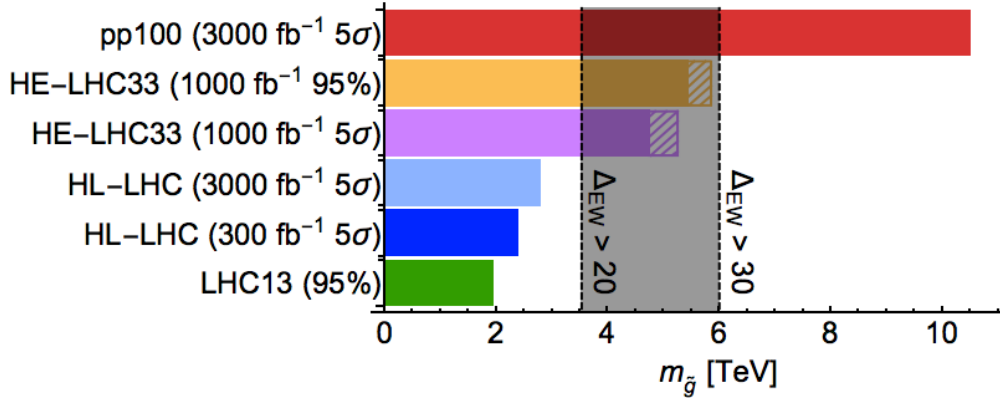
Figure 4.5: Discovery reach in $m_{\tilde{g}}$ for LHC and possible future upgrades. The vertical dashed lines are for $\Delta_{\mathrm{EW}} = 20$ and 30.

4.4 Same-Sign diBoson production

Models with light higgsinos produce a unique signal, SSdB, with two SM W bosons with the same charge. An example Feynman diagram with SSdB is shown in fig. 4.6, where a virtual W boson is produced, which then decays to a chargino and a heavier neutralino, $W^{*\pm} \to \widetilde{W}_2^{\pm} \widetilde{Z}_4$. This chargino would decay to a lighter SUSY particle, possibly the lightest neutralino, $\widetilde{Z}_1$, along with a SM boson, W. The heavier neutralino could decay to the lighter chargino $\widetilde{Z}_4 \to W^{\pm} \widetilde{W}_1^{\mp}$. Half of the time, the W boson from the chargino and the W boson from the heavier neutralino decays will have the same sign. With the dominant decay for the W bosons $W \to \ell \nu_{\ell}$, the signal will have same-sign (SS) dilepton events, which are qualitatively different from the $\tilde{g}\tilde{g}$ dilepton events due to the lack of jet activity from gluino pair events.

The leading-order (LO) and next-to-leading order (NLO) $\widetilde{Z}_4 \widetilde{W}_2$ and $\widetilde{W}_2 \widetilde{W}_2$ production cross sections were computed using Prospino[79]. Figure 4.7 shows the LO and NLO cross sections vs. $m_{\widetilde{W}_2}$ for $\{\widetilde{Z}_4 \widetilde{W}_2^+, \widetilde{W}_2^+ \widetilde{W}_2^-, \widetilde{Z}_4 \widetilde{W}_2^-\}$ shown in {red, blue, green} respectively with the total cross section in black.
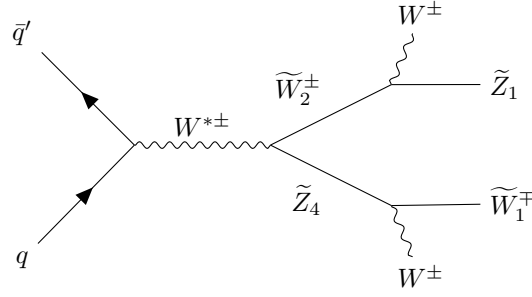
Figure 4.6: Feynman diagram for SSdB production. The chargino is chosen to be $\widetilde{W}_2$ with the heavier $\widetilde{Z}_4$ neutralino.
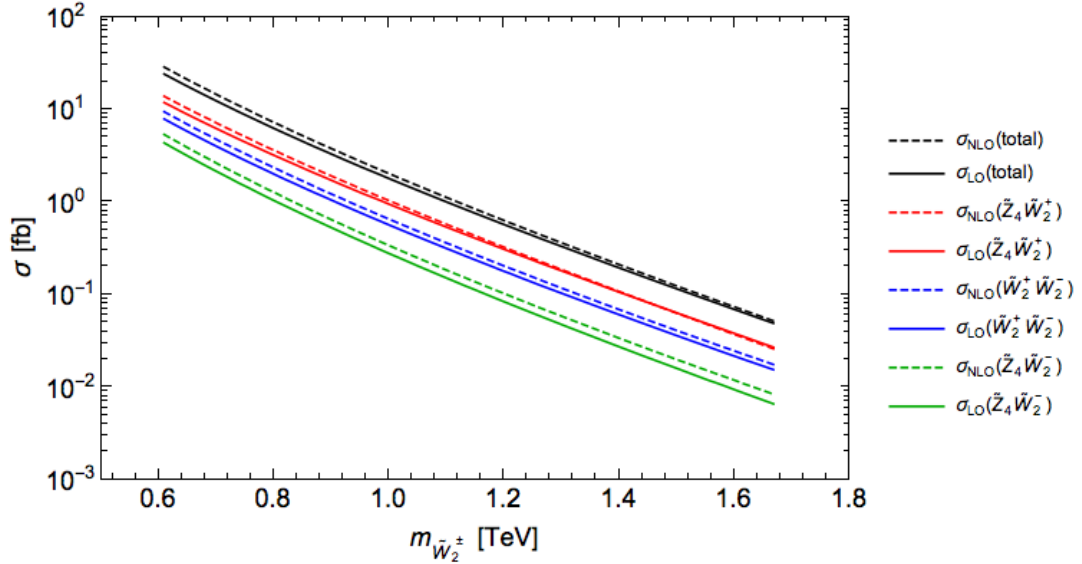
Figure 4.7: LO (solid) and NLO (dashed) cross sections for $\widetilde{Z}_4\widetilde{W}_2^{\pm}$ and $\widetilde{W}_2^{+}\widetilde{W}_2^{-}$ production vs. $m_{\widetilde{W}_2}$ at LHC with $\sqrt{s} = 14$ TeV. The $\widetilde{Z}_4\widetilde{W}_2^{+}$ cross section is larger than the $\widetilde{Z}_4\widetilde{W}_2^{-}$ due to the LHC being a *pp* collider, colliding positively charged particles.

Similar to the $\tilde{g}\tilde{g}$ analysis, a particular set of cuts must be implemented in order to distinguish SUSY signal from SM BG. For the SSdB signature, a benchmark point $m_0 = 5.0$ TeV, $m_{1/2} = 0.80$ TeV, $A_0 = -1.6m_0 = -8.6$ TeV, $\tan\beta = 10$, $\mu = 0.15$ TeV, $m_A = 2.0$ TeV was chosen for which the cuts were optimized. Before implementing cuts, the total SUSY signal is $\sigma_{SUSY} = 32.3$ fb. The following

cuts are used[80, 81]:

- *exactly* 2 isolated same-sign leptons with

  - $p_T(\ell_1) > 20$ GeV and

  - $p_T(\ell_2) > 10$ GeV,

- $n(b-\text{jets}) = 0$ (assist in removing $t\bar{t}$ BG),

- $\not{E}_T > 200$ GeV, and

- $m_T^{\min} > 175$ GeV,

where $m_T^{\min} \equiv \min\left(m_T\left(\ell_1, \not{E}_T\right), m_T\left(\ell_2, \not{E}_T\right)\right)$. The WZ SM BG has a sharp cut-off in m_T at the Z boson mass, so a cut of $m_T^{\min} > 175$ GeV will eliminate the expected WZ BG. After these cuts, the remaining BG is $\sigma_{BG} = 0.006$ fb and the remaining SUSY signal is $\sigma_{SUSY} = 0.045$ fb.

The SSdB channel can be a probe into the GUT scale value of gaugino mass, M_2. Varying $m_{1/2}$ from the NUHM2 benchmark point used for the SSdB signature varies M_2. A plot of the SSdB cross section after cuts, σ_{SSdB}, is plotted against the GUT scale value of M_2 in fig. 4.8. The reach in M_2 was determined using Poisson statistics with a BG of $\sigma_{BG} = 6$ ab. The LHC can discover up to $M_2(\text{GUT}) \approx 0.81$ TeV or exclude up to $M_2(\text{GUT}) \approx 0.92$ TeV compared to the naturalness limit of ≈ 1.5 TeV for NUHM2.

Multi-channel results for the LHC with $\sqrt{s} = 14$ TeV are shown in section 4.7. The discovery limits for the SSdB signature are plotted in conjunction with the $\tilde{g}\tilde{g}$ signal in the $m_{1/2} - m_0$ plane in fig. 4.14. SSdB and higgsino pair production, $\widetilde{Z}_2\widetilde{Z}_1 j$, to be discussed in section 4.5, are shown in the $\mu - m_{1/2}$ plane in fig. 4.15.
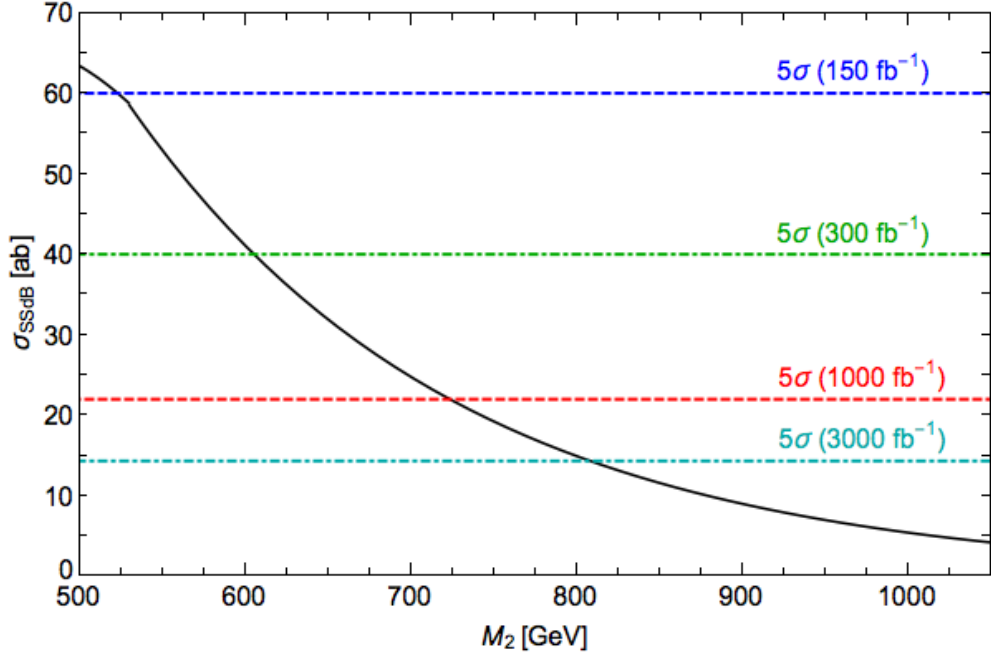
(a) 5σ discovery reach in $M_2(\text{GUT})$ for SSdB.
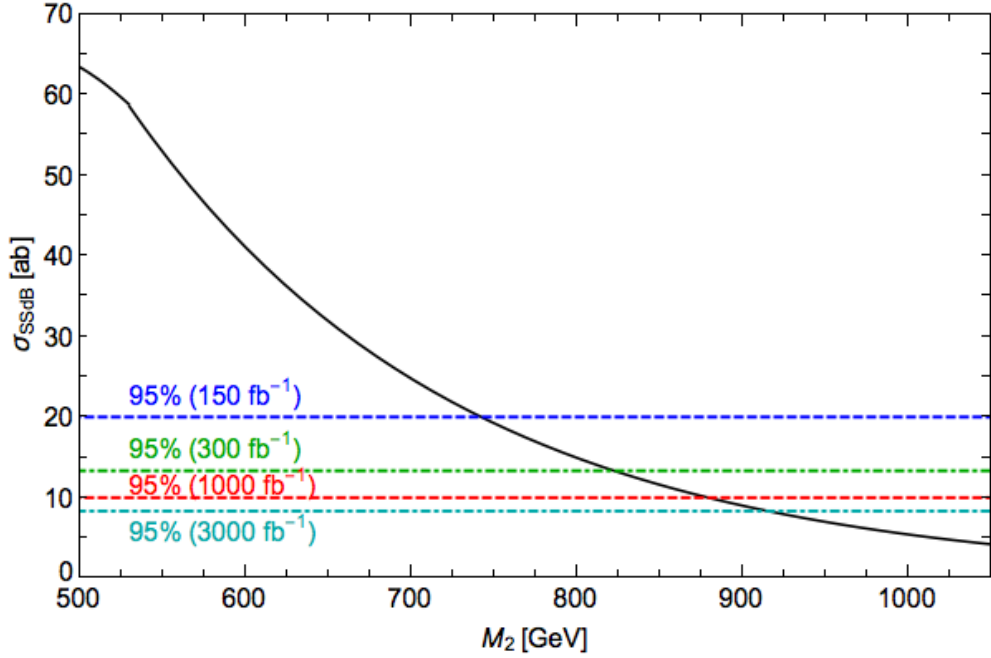
(b) 95% exclusion reach in $M_2(\text{GUT})$ for SSdB..

Figure 4.8: SSdB signal cross section as a function of $M_2(\text{GUT})$, varying $m_{1/2}$ form the benchmark point: $m_0 = 5.0$ TeV, $m_{1/2} = 0.80$ TeV, $A_0 = -1.6m_0 = -8.6$ TeV, $\tan\beta = 10$, $\mu = 0.15$ TeV, $m_A = 2.0$ TeV . The signal is plotted in black and the LHC reach for $L = \{150, 300, 1000, 3000\}\,\text{fb}^{-1}$ are shown in {blue, green, red, teal} respectively.

4.5   Higgsino pair prodution

An inescapable constraint from naturalness is placed on the μ parameter, which is restricted to a tight range of 100 GeV to 350 GeV. A way to experimentally probe μ is through higgsinos. The LHC can produce a pair of higgsinos along with a QCD jet arising from radiation of an initial state gluon. If this is done through the lightest higgsino, $\widetilde{Z}_1\widetilde{Z}_1 j$, it has been shown[82–84] that this signal cross section occurs at only 1% of QCD background. Instead, one can consider production of the heavier higgsino[85], $\widetilde{Z}_2$, with the subsequent decay $\widetilde{Z}_2 \to \widetilde{Z}_1 \ell^+\ell^-$, as shown in fig. 4.9. A feature of this channel is a pair of opposite-sign(OS), same-flavor(SF) leptons.
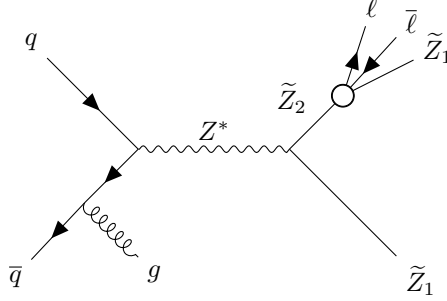
Figure 4.9: Feynman diagram for production of a heavy-light higgsino pair with an initial state radiation of a gluon, which would produce a QCD jet. The key signature is a pair of OS/SF leptons produced by the $\widetilde{Z}_2$ decay.

The higgsino pair, $\widetilde{Z}_2\widetilde{Z}_1 j$, signal allows for only a small amount of visible energy in the leptons, determined by $m_{\ell\bar{\ell}} = m_{\widetilde{Z}_2} - m_{\widetilde{Z}_1} \approx 3 - 20$ GeV. The cuts particular to the higgsino pair production are:

- *exactly* 2 OS/SF leptons and

- $\Delta\phi\left(\ell^+\ell^-\right) < \pi/2$.

The results for the higgsino pair production are shown in fig. 4.15 in a multi-channel diagram along with SSdB in the $\mu - m_{1/2}$ plane.

4.6   Top squark pair production

Natural SUSY has an inverted squark mass structure, with the third generation squarks being the lightest and the first and second generation squarks being more massive. With the low top squark masses, typically below 1.5 TeV, top squark production is a readily available signal[86]. The naturalness limit in NUHM2 on the lightest top squark mass extends out to $m_{\tilde{t}_1} \approx 3$ TeV. Compared to this, the ATLAS search ($pp \rightarrow \tilde{t}_1 \tilde{t}_1^*$ with $\tilde{t}_1 \rightarrow t\widetilde{Z}_1$, $\tilde{t}_1 \rightarrow bW\widetilde{Z}_1$, or $\tilde{t}_1 \rightarrow c\widetilde{Z}_1$) extends to only 0.95 TeV[42]. Figure 4.10 shows the $m_{\widetilde{Z}_1} - m_{\tilde{t}_1}$ plane with the ATLAS 2017 discovery and anticipated 3000 fb^{-1} reaches.
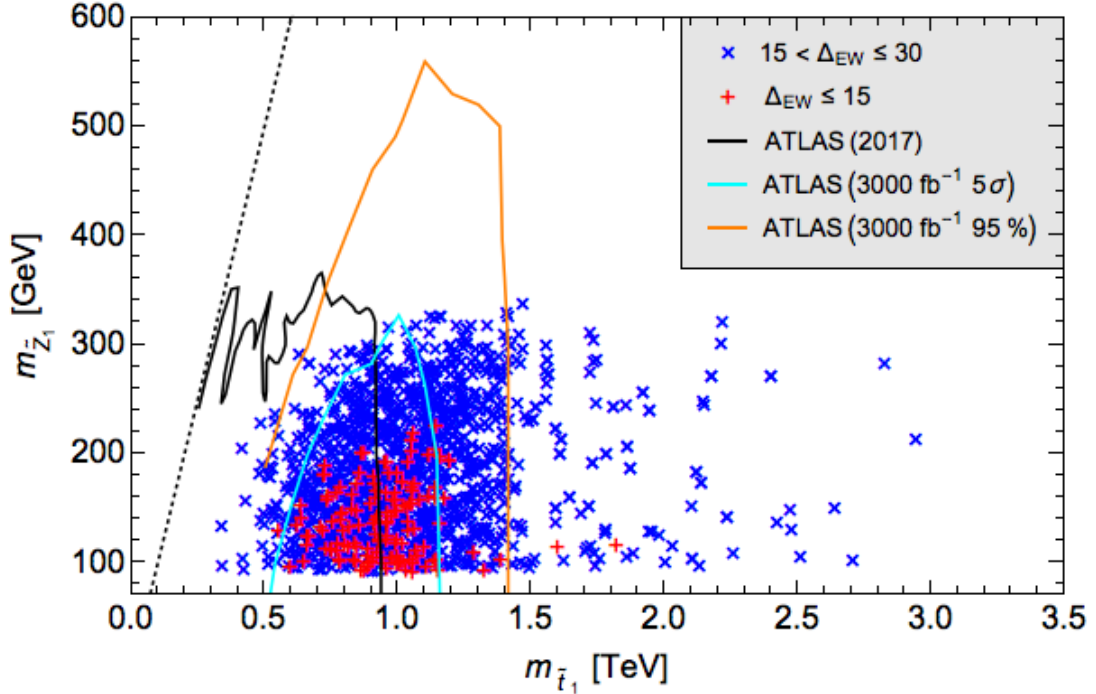
Figure 4.10: Natural NUHM2 in the $m_{\widetilde{Z}_1} - m_{\tilde{t}_1}$ plane showing $\Delta_{EW} \leq 15$ in blue $\times$ and $15 < \Delta_{EW} \leq 30$ in red $+$. The dotted black line is where $m_{\widetilde{Z}_1} = m_{\tilde{t}_1}$. The current reach from ATLAS with $\sqrt{s} = 13$ TeV and $L = 36.1$ fb^{-1} is shown in black with the potential 5σ discovery shown in cyan and 95% exclusion shown in orange for 3000 fb^{-1}.
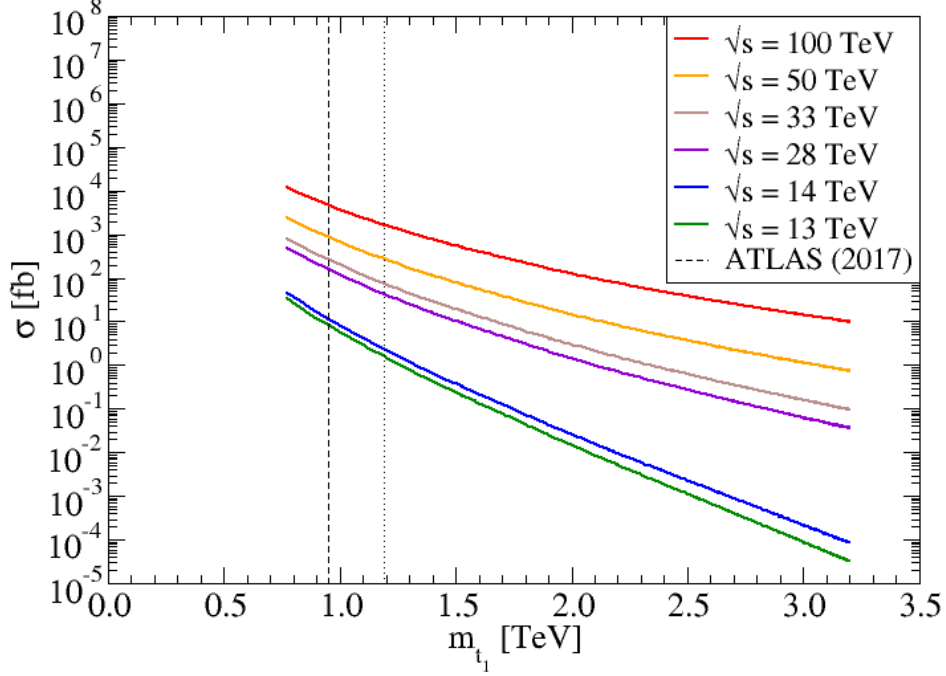
Figure 4.11: NLO top squark pair production cross section vs. $m_{\tilde{t}_1}$ for $\sqrt{s} = \{13, 14, 28, 33, 50, 100\}$ TeV. The vertical dashed(dotted) line shows the current(expected) reach of 0.95(1.15) TeV

Top squark pair production is predominantly through the QCD gg and $q\bar{q}$ annihilation channels. Taking the benchmark point: $m_0 = 5.0$ TeV, $m_{1/2} = 0.80$ TeV, $A_0 = -1.6m_0 = -8.6$ TeV, $\tan\beta = 10$, $\mu = 0.15$ TeV, $m_A = 2.0$ TeV , A_0 was varied from -10 TeV to 10 TeV, which varies $m_{\tilde{t}_1}$. NLO top squark pair production rates vs. $m_{\tilde{t}_1}$ for LHC at $\sqrt{s} = 13$ and 14 TeV, as well as potential upgrades to 28, 33, 50, and 100 TeV, calculated using Prospino, are shown in fig. 4.11. The vertical dashed(dotted) show the current(expected) reach of LHC in $m_{\tilde{t}_1}$.

Top squark decays have multiple dominant modes. The branching fractions of the top squark decay modes are shown in fig. 4.12 as a function of A_0 in (a)

98

and $m_{\tilde{t}_1}$ in (b). For almost the entire region of $m_{\tilde{t}_1}$, the branching fractions to $\{b\widetilde{W}_1, t\widetilde{Z}_1, t\widetilde{Z}_2\}$ are $\{50\%, 25\%, 25\%\}$, leading to the expected signatures of

- A: $\tilde{t}_1 \tilde{t}_1^* \to b\bar{b} + \not{E}_T$ 25%
- B: $\tilde{t}_1 \tilde{t}_1^* \to b\bar{t}, t\bar{b} + \not{E}_T$ 50%
- C: $\tilde{t}_1 \tilde{t}_1^* \to t\bar{t} + \not{E}_T$ 25%

Signature A includes hard b-jets with high $\not{E}_T$. BG would be abundant in $b\bar{b}Z$ with $Z \to \nu\bar{\nu}$. The m_{T2} variable could be implemented to the $b\bar{b}Z$ final state to reconstruct the kinematic upper edge to estimate the top squark mass.

Signature B includes hard t-jets with high $\not{E}_T$. This signature would include $b\bar{b} + \not{E}_T$ along with a W. If the W decays hadronically, $W \to f\bar{f}'$, the W mass may be reconstructed. BG would be abundant in $t\bar{t}$, $Wb\bar{b}$, WZ, and tbZ. This channel has been emphasized by Graesser and Shelton[87].

Signature C includes a hard $t\bar{t}$ pair with high $\not{E}_T$. The dominant BG would be $Zt\bar{t}$. The hard t-jets could benefit from a top-tagger[88–93].

Overall, a credible semi-simplified model could be used for the $m_{\mathrm{higgsino}} - m_{\tilde{t}_1}$ plane, which would include several dominant decay branching fractions, along with the mixed decay mode of $\tilde{t}_1$ to $b\widetilde{W}_1$ and $t\widetilde{Z}_{1,2}$. Figure 4.13 shows the reach of LHC and its possible energy upgrades in $m_{\tilde{t}_1}$ as well as the $\Delta_{EW} = 20$ and 30 natural limits.
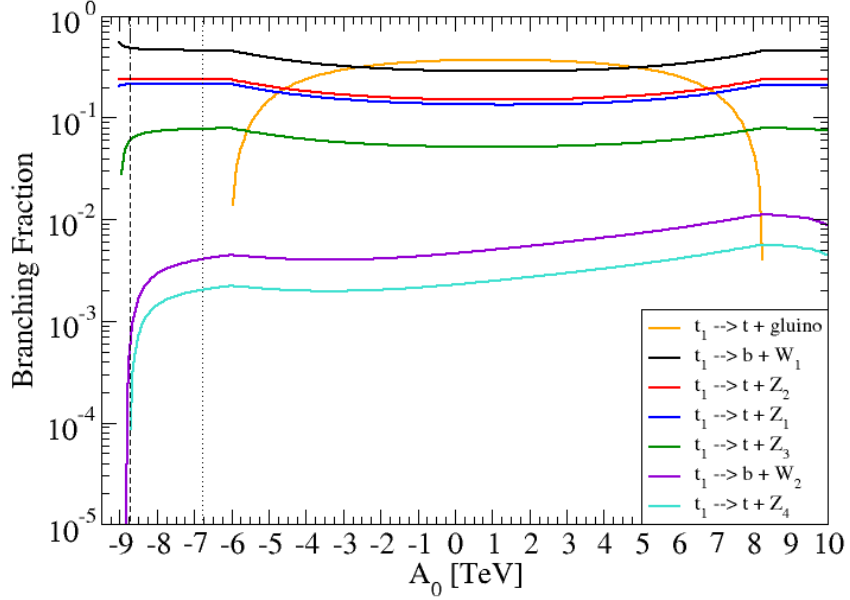
(a) Branching fraction of the top squark as A_0 varies.
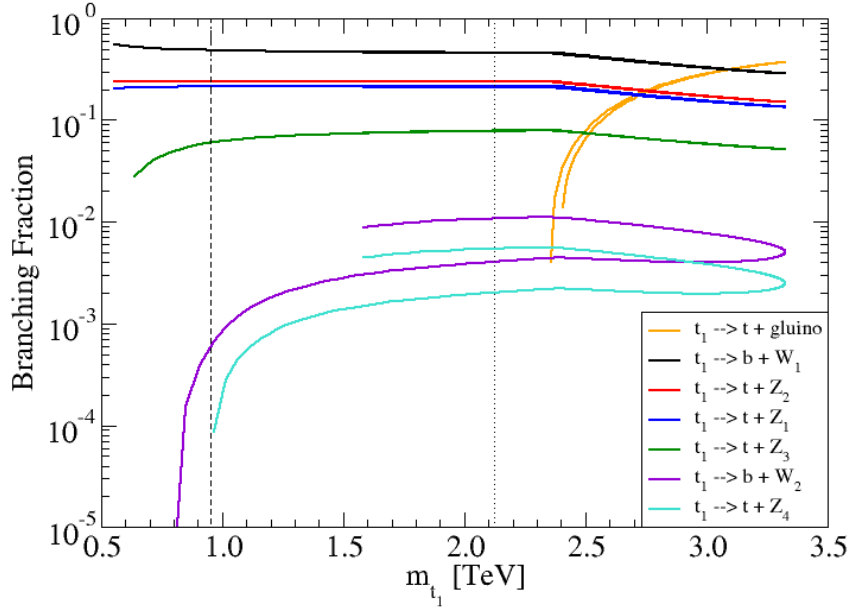
(b) Branching fraction of the top squark as $m_{\tilde{t}_1}$ varies.

Figure 4.12: Top squark branching fractions vs A_0 in (a) and $m_{\tilde{t}_1}$ in (b). Decays $\tilde{t}_1 \to \{t\tilde{g}, b\widetilde{W}_1, t\widetilde{Z}_2, t\widetilde{Z}_1, t\widetilde{Z}_3, b\widetilde{W}_2, t\widetilde{Z}_4\}$ are shown in {orange, black, red, blue, green, violet, cyan} respectively. The vertical dashed line is the current reach of 0.95 TeV and the vertical dotted line is where $m_h = 123$ GeV.
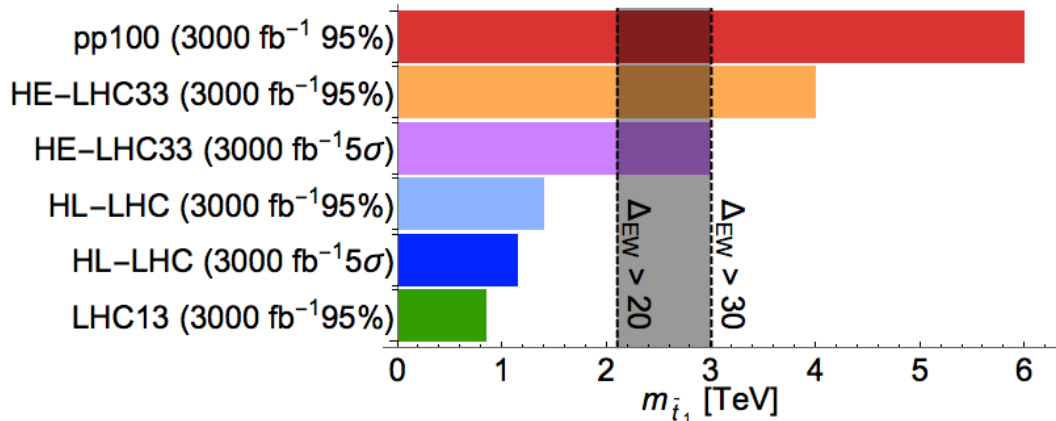
Figure 4.13: Discovery and exclusion limits for LHC at $\sqrt{s} = 13$, 14, 33, and 100 TeV. The vertical lines show $\Delta_{EW} = 20$ and 30.

4.7 Multi-channel detector limits

Summarizing the analyses of the previous sections with their respective channels paints a full picture of the discovery potential of the LHC at $\sqrt{s} = 14$ TeV. The SSdB and $\tilde{g}\tilde{g}$ reaches are shown in the $m_{1/2} - m_0$ plane in fig. 4.14. The 5σ discovery reach extends to almost the entire region of natural SUSY for the NUHM2 archetype. A similar plot for the 95% exclusion extends beyond the $\Delta_{EW} = 30$ contour and covers all of natural SUSY.

The SSdB and $\widetilde{Z}_2\widetilde{Z}_1 j$ reaches are shown in the $\mu - m_0$ plane in fig. 4.15. The 5σ reach barely covers the entire natural SUSY parameter space for the NUHM2 archetype. For comparison, the ILC reach in $e^+e^- \to \widetilde{W}_1\widetilde{W}_1$ and $\widetilde{Z}_2\widetilde{Z}_1$ channels for $\sqrt{s} = 0.5$ TeV and 1.0 TeV are shown in black. For the ILC to cover the entire natural NUHM2 parameter space, $\sqrt{s} \geq 0.6$ TeV is required. The analogous 95% exclusion plot, not shown for brevity, covers up to $m_0 = 1.0(1.4)$ TeV in the SSdB channel and 240(300) GeV in the $\widetilde{Z}_2\widetilde{Z}_1 j$ channel for $L = 300(3000)$ fb^{-1}. These reaches cover almost all the parameter space at $L = 300$ fb^{-1} and nearly all of $\Delta_{EW} \leq 50$ for $L = 3000$ fb^{-1}.
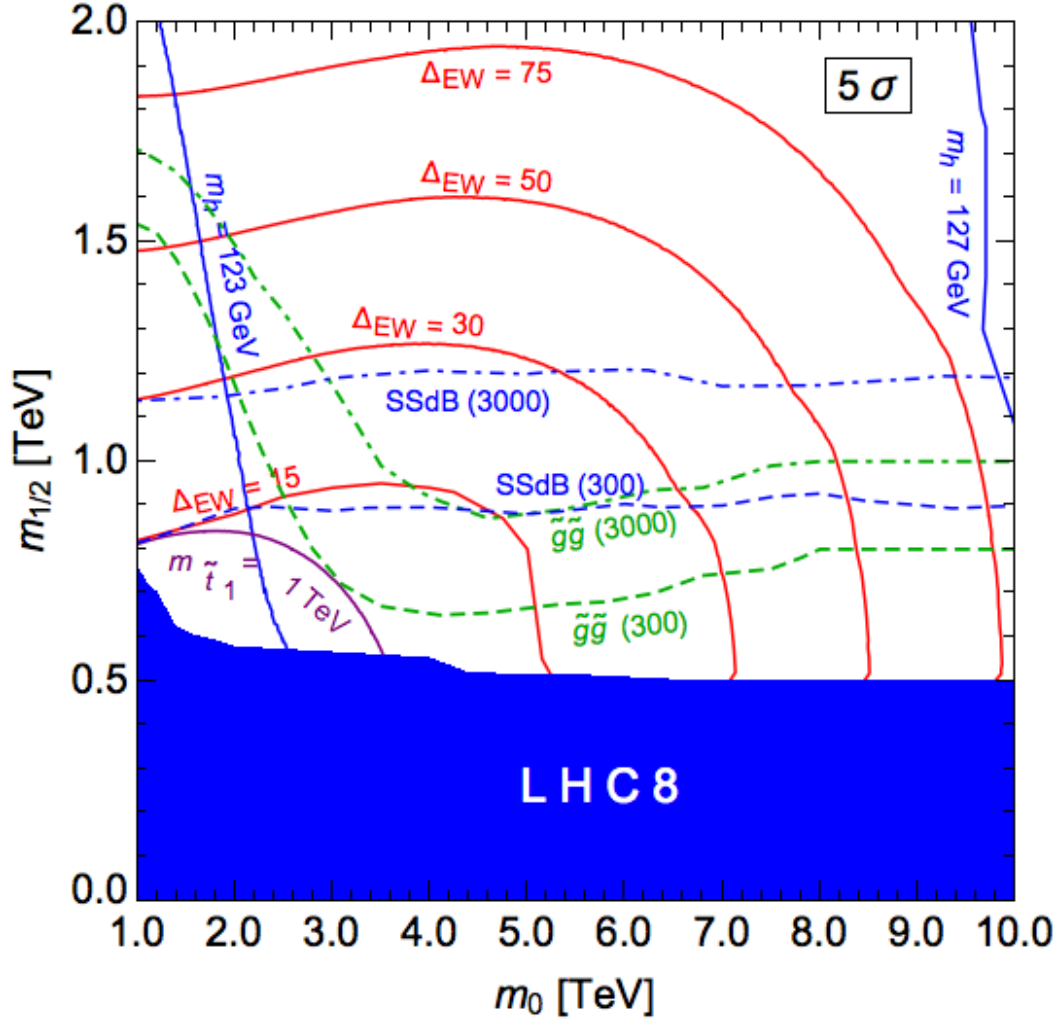
Figure 4.14: LHC discovery potential with $\sqrt{s} = 14$ TeV through the SSdB and $\tilde{g}\tilde{g}$ channels in the $m_{1/2} - m_0$ plane. The solid red contours depict naturalness, the dashed(dot-dashed) blue curve show the SSdB reach for luminosity of 300(3000) fb^{-1} and the dashed(dot-dashed) green curve shows the gluino pair production reach for 300(3000) fb^{-1} integrated luminosity. Also shown are the SM Higgs boson mass in solid blue and $m_{\tilde{t}_1} = 1$ TeV in violet along with the exclusion from LHC with $\sqrt{s} = 8$ TeV.
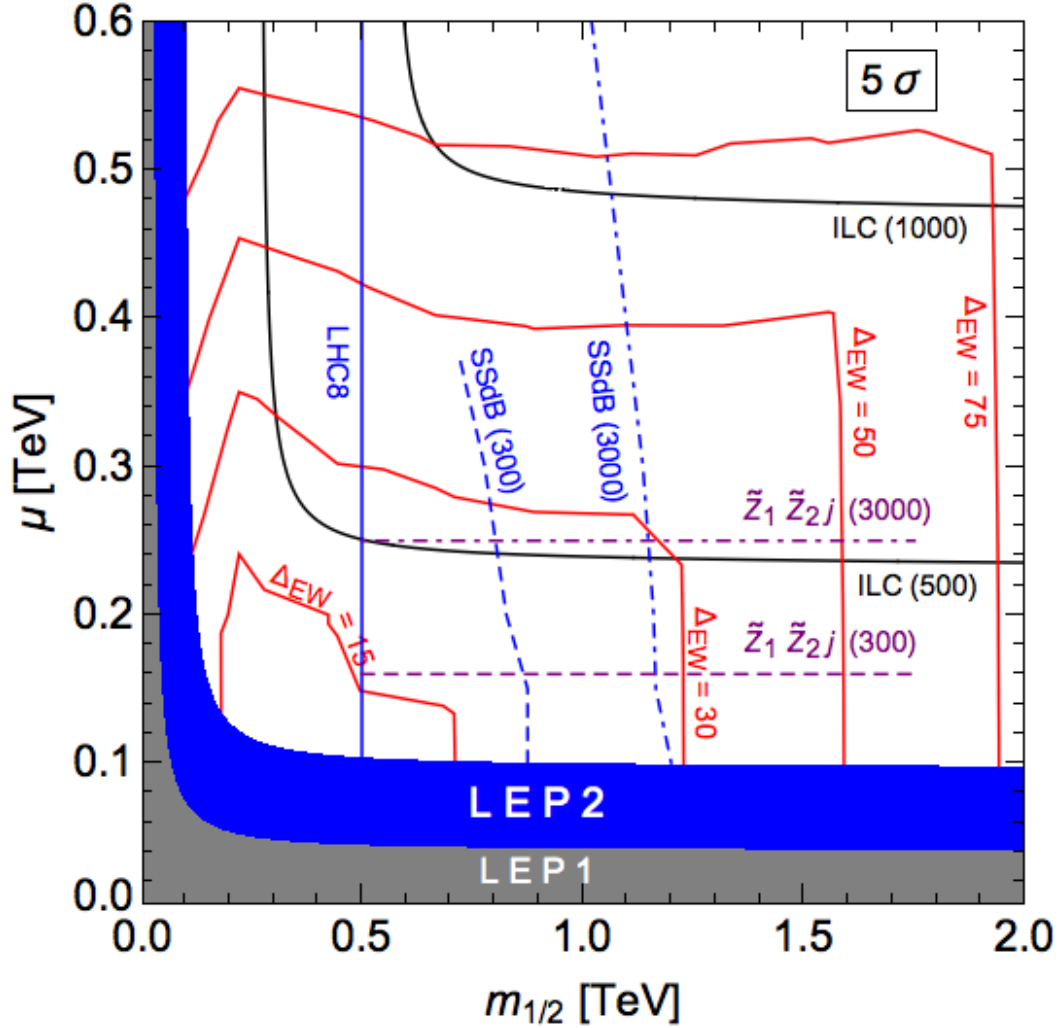
Figure 4.15: LHC discovery potential with $\sqrt{s} = 14$ TeV through the SSdB and $\widetilde{Z}_2\widetilde{Z}j$ channels in the $\mu - m_0$ plane. The solid red contours depict naturalness, the dashed(dot-dashed) blue curve show the SSdB reach for 300(3000) fb^{-1} integrated luminosity and the dashed(dot-dashed) violet curve shows the higgsino pair reach for 300(3000) fb^{-1} integrated luminosity. Also shown are the LEP 1 and 2 exclusion regions. The ILC reaches for $\sqrt{s} = 500$ GeV and $\sqrt{s} = 1000$ GeV are shown in black.

Chapter 5

Conclusions

Searches for new phenomena at the LHC with $\sqrt{s} = 13$ TeV pp collisions have found no evidence for supersymmetry. Lower limits on sparticle masses have been set, such as $m_{\tilde{t}_1} = 0.95$ TeV and $m_{\tilde{g}} = 2.1$ TeV. These limits may be compared to upper bounds on sparticle masses from naturalness, for example: three third generation squark masses below 500 GeV from Δ_{HS} or gluino masses below 350 GeV from Δ_{BG}. This confrontation might lead to the conclusion that SUSY is in a crisis or dead; however, in this thesis I point out that these early measures of fine-tuning are based on faulty calculations and poor assumptions. The measure of Δ_{HS} makes several unwarranted simplifications that hide possible cancellations. The Δ_{BG} measure is ambiguous as to which GUT scale parameters are independent. The revised measure of fine-tuning is Δ_{EW}, which is a conservative measure that is easy to calculate for any SUSY model unambiguously. I showed that values of $\Delta_{EW} > 30$ exhibit significant electroweak fine-tuning. Maintaining $\Delta_{EW} \leq 30$ limits the total SUSY parameter space. In this thesis, I derived new upper bounds on sparticle masses which turn out to be beyond the current limits set from experiment, for example: $m_{\tilde{t}_1} < 3$ TeV and $m_{\tilde{g}} < 4.5$ TeV from NUHM2 models. Thus, LHC has only begun to explore the natural SUSY parameter space.

Several probes to search the SUSY parameter space were discussed. Searching in the $m_{1/2}$ direction are the $\tilde{g}\tilde{g}$ and SSdB channels. In the μ direction is the $\widetilde{Z}_2\widetilde{Z}_1 j$ channel. In the $m_{\tilde{t}_1}$ direction is the $\tilde{t}_1\tilde{t}_1$ channel. Through a multi-channel analysis, the HL-LHC will be able to discover (at 5σ) or exclude (at 95%) all of the natural NUHM2 parameter space. The other GUT models have similar bounds

on $m_{\tilde{t}_1}$ and $m_{\tilde{g}}$ and will yield similar reaches for the $\tilde{g}\tilde{g}$, SSdB, and higgsino pair production limits. Therefore, the exclusion potential of the HL-LHC would extend to the other GUT models sampled.

GMM models, motivated by string theory through the combination of anomaly and gravity mediation, yield even larger limits on sparticle masses from naturalness, e.g. $m_{\tilde{g}} < 6$ TeV. Even the multi-channel analysis from HL-LHC would fall short of the limits in the GMM model. After the HL-LHC finishes collecting data, potential upgrades are to either a $\sqrt{s} = 33$ or 100 TeV HE-LHC. With an energy upgrade to $\sqrt{s} = 33$ TeV (not requiring 100 TeV), the HE-LHC would be able to discover any natural SUSY model considered here. Furthermore, the ILC, if constructed, would be a Higgs/higgsino factory. The higgsino production probes in the μ direction. Because of the model independent limit on $\mu \leq 350$ GeV from naturalness, ILC with $\sqrt{s} = 600 - 700$ GeV would be able to test *any* natural SUSY model based on the MSSM through the discovery or exclusion of higgsino pair production.

References

[1] M. Peskin and D. Shroeder, "An Introduction to Quantum Field Theory," *Westview Press Incorporated* (1995) 864 p.

[2] ATLAS collaboration. *Phys. Rev. Lett.* **114** (2015) 191803 [arXiv:1503.07589].

[3] T. Aoyama, M. Hayakawa, T. Kinoshita, and M. Nio. *Phys. Rev. Lett.* **109** (2012) 111807 [arXiv:1205.5368].

[4] D. Hanneke, S. Fogwell, and G. Gabrielse. *Phys. Rev. Lett.* **100** (2008) [arXiv:0801.1134].

[5] Makoto Kobayashi and Toshihide Maskawa. *Prog. Theor. Phys.* **49** (1973) 2, 652-657.

[6] S. W. Herb, J. A. Appel, A. S. Ito, et al. *Phys. Rev. Lett.* **39** (1997) 5.

[7] F. Abe et al. (CDF collaboration). *Phys. Rev. Lett.* **74** (1995) 2626.

[8] S. Abachi et al. (D∅ collaboration). *Phys. Rev. Lett.* **74** (1995) 2632.

[9] F. Englert and R. Brout. *Phys. Rev. Lett.* **13** (1964) 9, 321-323.

[10] UA1 collaboration. *Phys. Lett. B* **122** (1983) 24, 103-116.

[11] UA2 collaboration. *Phys. Lett. B* **122** (1983) 5-6, 476-485.

[12] P. Higgs. *Phys. Rev. Lett.* **13** (1964) 16, 508-509.

[13] CMS collaboration. *Phys. Lett. B* **716** (2012) 30-61 [arXiv:1207.7235].

[14] ATLAS collaboration. *Phys. Lett. B* **716** (2012) 1-29 [arXiv:1207.7214].

[15] E. Witten, *Nucl. Phys. B* **188**, 513 (1981.

[16] M. S. Carena and H. E. Haber, *Prog. Part. Nucl. Phys.* **50** (2003) 63 [hep-ph/0208209].

[17] H. Baer and X. Tata, "Weak scale supersymmetry: From superfields to scattering events," Cambridge, UK: *Univ. Pr.* (2006) 537 p.

[18] S. K. Soni and H. A. Weldon, *Phys. Lett. B* **126** (1983) 215.

[19] V. S. Kaplunovsky and J. Louis, *Phys. Lett. B* **306** (1993) 269.

[20] A. Brignole, L. E. Ibanez, and C. Munoz, *Nucl. Phys. B* **422** (1994) 125 [*Erratum-ibid. B* **436** (1995) 747].

[21] H. Baer, V. Barger, P. Huang, D. Mickelson, A. Mustafayev and X. Tata, *Phys. Rev. D* **87** (2013) 115028.

[22] H. Baer, V. Barger, and, M. R. Savoy. *Phys. Scripta* **90** (2015) 068003 [arXiv:1502.04127 [hep-ph]].

[23] J. R. Ellis, K. Enqvist, D. V. Nanopoulos, and F. Zwirner, *Mod. Phys. Lett. A* **1** (1986) 57.

[24] R. Barbieri and G. F. Giudice, *Nucl. Phys. B* **306** (1988) 63.

[25] H. Abe, T. Kobayashi, and Y. Omura, *Phys. Rev. D* **76** (2007) 015002.

[26] S. P. Martin, *Phys. Rev. D* **75** (2007) 115005.

[27] J. L. Feng, *Ann. Rev. Nucl. Part. Sci.* **63** (2013) 351.

[28] H. Baer, V. Barger, D. Mickelson, and M. Pade ke-Kirkland, *Phys. Rev. D* **89**, 115019 (2014).

[29] S. Cassel, D. M. Ghilencea, S. Kraml, A. Lessa, and G. G. Ross, *JHEP* **1105** (2011) 120.

[30] G. G. Ross, *Eur. Phys. J. C* **74** (2014) 2699.

[31] D. M. Ghilencea and G. G. Ross. *Nucl. Phys. B* **868** (2012) 1 [arXiv:1208.0837 [hep-ph]].

[32] S.S. Wilks, *Ann. Math. Statist.* **9** (1938) 60-2.

[33] Wilks, S. S. (1962). *Mathematical Statistics.* Wiley, New York; 2d printing, corrected, 1963.

[34] H. Baer, V. Barger, M. Savoy, and H. Serce. *Phys. Lett. B* **758** (2016) 10 [arXiv:1602.07697 [hep-ph]].

[35] H. Baer, V. Barger, P. Huang, D. Mickelson, A. Mustafayev, W. Sreethawong, and X. Tata, *JHEP* **1312** (2013) 013.

[36] ISAJET, by H. Baer, F. Paige, S. Protopopescu, and X. Tata, hep-ph/0312045.

[37] Joint LEP 2 Supersymmetry Working Group, *Combined LEP Chargino Results up to 208 GeV*,
http://lepsusy.web.cern.ch/lepsusy/www/inos_moriond01/charginos_pub.html.

[38] G. Aad et al. (ATLAS collaboration), *Phys. Lett. B* **710** (2012) 67.

[39] K. Bae, H. Baer, V. Barger, D. Mickelson, and M. Savoy, *Phys. Rev. D* **90**, 075010 (2014). [arXiv:1407.3853 [hep-ph]].

[40] H. Baer, V. Barger, and M. Savoy. *Phys. ReV. D* **93** (2016) 035016 [arXiv:1509.02929 [hep-ph]].

[41] Gabriella Pásztor, *ATL-PHYS-PROC-* **2016-020** (2015) [arXiv:1602.01536 [hep-ex]].

[42] The ATLAS collaboration [ATLAS Collaboration], ATLAS-CONF-2017-037.

[43] The ATLAS collaboration [ATLAS Collaboration], ATLAS-CONF-2017-053.

[44] H. Baer, V. Barger, and M. Savoy. *Phys. Rev. D* **93** (2016) 075001 [arXiv:1602.06973 [hep-ph]].

[45] K. R. Dienes, *Adv. Ser. Direct. High Energy Phys.* **22** (2015) 81.

[46] H. P. Nilles and P. K. S. Vaudrevange, *Adv. Ser. Direct. High Energy Phys.* **22** (2015) 49.

[47] O. Lebedev, H. P. Nilles, S. Raby, S. Ramos-Sanchez, M. Ratz, P. K. S. Vaudrevange and A. Wingerter, *Phys. Lett. B* **645** (2007) 88 [hep-th/0611095].

[48] O. Lebedev, H. P. Nilles, S. Ramos-Sanchez, M. Ratz and P. K. S. Vaudrevange, *Phys. Lett. B* **668** (2008) 331 [arXiv:0807.4384 [hep-th]].

[49] H. P. Nilles, *Phys. Lett.* **115B** (1982) 193.

[50] H. P. Nilles, *Nucl. Phys. B* **217** (1983) 366.

[51] S. Ferrara, L. Girardello, and H. P. Nilles, Phys. Lett. 125B (1983) 457.

[52] T. Kobayashi, S. Raby, and R. J. Zhang, Nucl. Phys. B 704 (2005) 3.

[53] H. P. Nilles, *Adv. High Energy Phys.* **2015** (2015) 412487.

[54] S. Krippendorf, H. P. Nilles, M. Ratz, and M. W. Winkler, *Phys. Lett. B* **712** (2012) 87 [arXiv:1201.4857 [hep-ph]].

[55] M. Badziak, S. Krippendorf, H. P. Nilles, and M. W. Winkler, J. High Energy Phys. 1303 094 (2013).

[56] L. Randall and R. Sundrum, *Nucl. Phys. B* **557**, (1999) 79.

[57] G. F. Giudice, M. Luty, H. Murayama, and R. Rattazzi, *J. High Energy Phys.* **9812**, 027 (1998).

[58] J. Bagger, T. Moroi, and E. Poppitz, *J. High Energy Phys.* **0004**, 009 (2000).

[59] P. Binetruy, M. K. Gaillard, and B. Nelson, *Nucl. Phys. B* **604**, 32 (2001).

[60] K. Choi, A. Falkowski, H. P. Nilles, M. Olechowski, and S. Pokorski, *J. High Energy Phys.* **0411**, (2004) 076.

[61] K. Choi, A. Falkowski, H. P. Nilles, and M. Olechowski, *Nucl. Phys. B* **718**, (2005) 113.

[62] J. P. Conlon, F. Quevedo, and K. Suruliz, *JHEP* **0508**, (2005) 007 [arXiv:hep-th/0505076].

[63] A. Pierce and J. Thaler, *JHEP* **0609** (2006) 017.

[64] B. L. Kaufman, B. D. Nelson, and M. K. Gaillard, *Phys. Rev. D* **88** (2013) no.2, 025003.

[65] K. Choi, K-S. Jeong, and K. Okumura, *J. High Energy Phys.* **0509**, (2005) 039.

[66] A. Falkowski, O. Lebedev, and Y. Mambrini, J. High Energy Phys. 0511, (2005) 034.

[67] H. Baer, V. Barger, M. Savoy, H. Serce, and X. Tata. (2017) [arXiv:1705.01578 [hep-ph]].

[68] The ATLAS collaboration [ATLAS Collaboration], ATLAS-CONF-2017-020.

[69] CMS Collaboration [CMS Collaboration], CMS-PAS-SUS-16-051.

[70] J. Alwall, M. Herquet, F. Maltoni, O. Mattelaer, and T. Stelzer, *JHEP* **1106** (2011) 128.

[71] T. Sjostrand, S. Mrenna, and P. Z. Skands, *Comput. Phys. Commun.* **178** (2008) 852.

[72] J. de Favereau et al. [DELPHES 3 Collaboration], *JHEP* **1402** (2014) 057.

[73] H. Baer, V. Barger, J. Gainer, P. Huang, M. Savoy, D. Sengupta, and X. Tata. (2016) [arXiv:1612.00795].

[74] S. Corréad, V. Kostioukine, J. Levêque, A. Rozanov, J. B. de Vivie, ATLAS Note, ATLAS- PHYS-2004-006, and V. Kostioukine, ATLAS Note, ATLAS-PHYS-2003-033.

[75] M. Cacciari, G. P. Salam, and G. Soyez, *JHEP* **0804**, 063 (2008) doi:10.1088/1126-6708/2008/04/063 [arXiv:0802.1189 [hep-ph]].

[76] M. Cacciari, G. P. Salam, and G. Soyez, *Eur. Phys. J. C* **72**, 1896 (2012) doi:10.1140/epjc/s10052-012-1896-2 [arXiv:1111.6097 [hep-ph]].

[77] M. Cacciari and G. P. Salam, *Phys. Lett. B* **659**, 119 (2008) doi:10.1016/j.physletb.2007.09.077[arXiv:0707.1378 [hep-ph]].

[78] H. Baer, V. Barger, J. Gainer, P. Huang, M. Savoy, H. Serce, and X. Tata. (2017) [arXiv:702.06588 [hep-ph]].

[79] W. Beenakker, R. Hopker and M. Spira, hep-ph/9611232.

[80] H. Baer, V. Barger, P. Huang, D. Mickelson, A. Mustafayev, W. Sreethawong and X. Tata, *JHEP* **1312** (2013) 013.

[81] H. Baer, V. Barger, P. Huang, D. Mickelson, A. Mustafayev, W. Sreethawong and X. Tata, *Phys. Rev. Lett.* **110** (2013) no.15, 151801.

[82] H. Baer, A. Mustafayev, and X. Tata, *Phys. Rev. D* **89** (2014) no.5, 055007. [arXiv:1701.03480].

[83] C. Han, A. Kobakhidze, N. Liu, A. Saavedra, L. Wu, and J. M. Yang, *JHEP* **1402** (2014) 049. [arXiv:].

[84] P. Schwaller and J. Zurita, *JHEP* **1403** (2014) 060.

[85] H. Baer, V. Barger, M. Savoy, and X. Tata. *Phys. Rev. D* **94** (2016) 035025 [arXiv:1604.07438 [hep-ph]].

[86] H. Baer, V. Barger, N. Nagata, and M. Savoy. *Phys. ReV. D* **95** (2016) 055012 [arXiv:1611.08511 [hep-ph]].

[87] M. L. Graesser and J. Shelton, *Phys. Rev. Lett.* **111** (2013) no.12, 121802.

[88] D. E. Kaplan, K. Rehermann, M. D. Schwartz and B. Tweedie, *Phys. Rev. Lett.* **101** (2008), 142001.

[89] J. Thaler and L. T. Wang, *JHEP* **0807** (2008), 092.

[90] L. G. Almeida, S. J. Lee, G. Perez, I. Sung and J. Virzi, *Phys. Rev. D* **79** (2009), 074012.

[91] T. Plehn, G. P. Salam and M. Spannowsky, *Phys. Rev. Lett.* **104** (2010), 111801.

[92] T. Plehn, M. Spannowsky, M. Takeuchi and D. Zerwas, *JHEP* **1010** (2010), 078.

[93] V. Barger and P. Huang, *Phys. Lett. B* **708** (2012) 296.